Doctoral Dissertation

博士論文

A Study of Baseline Compensation System for Stable Operation of Gravitational-wave Telescopes

(重力波望遠鏡の安定稼働のための基線長補償システムの研究)

A Dissertation Submitted for the Degree of Doctor of Philosophy

December 2019

令和元年12月博士 (理学) 申請

Depertment of Physics, Graduate School of Science,
The University of Tokyo
東京大学大学院理学系研究科
物理学専攻

Kouseki Miyo
三代浩世希

Contents

Chapter 1

Background

In 2015, an epoch when LIGO detectors have detected gravitational-waves (GW), new astronomy had been established. From the first detection, the development of GW detectors has been a history of improving sensitivity. It is necessary to improve the duty cycle, which is the observable time, as well as the sensitivity because the GW astronomy needs multiple detectors to determine the direction of the arrival.

This chapter describes GW and GW detectors. GWs cause strain changes in space which are extremely small. In order to detect the strain, the GW detector is a complex Michelson interferometer with several optical resonators. In addition, in order to increase the sensitivity of strain measurement, the baseline is enlarged. The complicated and large interferometer has a limited duty cycle due to seismic noise. This chapter focuses on the duty cycle of the terrestrial large-scale GW detector because the purpose of this thesis is the development of the new seismic isolation system to improve the duty cycle.

In section 1.1, we describe the essential properties and sources of the gravitational-wave. Section 1.2 describes the detection principle of the GW by using an interferometer. In section 1.3 and 1.4, we describe the technology to improve the sensitivity of the detectors and the duty cycle of the current terrestrial detectors, respectively. At the end of the chapter, we describe the outline of this thesis in section 1.5.

1.1 Gravitational-wave (GW)

Gravitational-wave (GW) is a ripple of the space-time which propagates at the speed of light. These waves are generated by the dynamic motion of the massive object in the universe. Therefore, the GW informs us not only the feature of the space-time but also

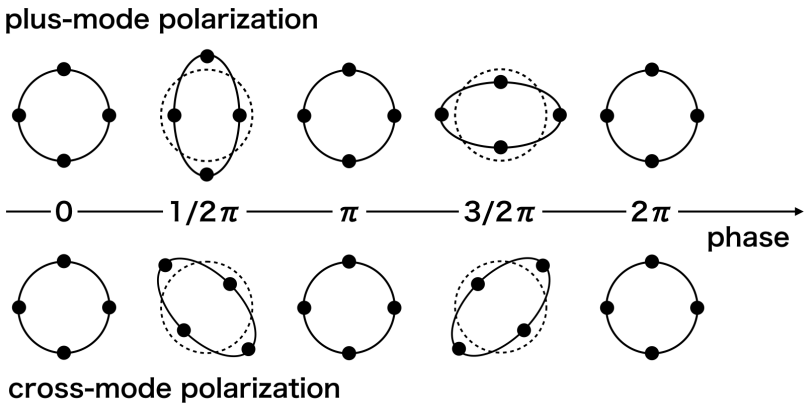

Figure 1.1: Polarizations of the GW propagating in the direction of the paper. These polarizations change the distance as the tidal motion.

the mechanism of the high-energy astrophysical phenomena.

1.1.1 Properties of GWs

GW was predicted by A. Einstein in 1918 and is a result of the general theory of relativity.

Two polarized transverse waves

The metric tensor $g_{\mu\nu}$ describes the interval between two events in space-time as,

$$ds^2 = g_{\mu\nu}dx^\mu dx^\nu (\mu, \nu = 0, 1, 2, 3), \tag{1.1}$$

where dx^μ represents the coordinate distance of the events, and x^μ has four components; (ct, x, y, z).

In the general relativity theory [1], the metric tensor $g_{\mu\nu}$ is described by Einstein's equation;

$$R_{\mu\nu}\left(g_{\mu\nu}\right) - \frac{1}{2}g_{\mu\nu}R\left(g_{\mu\nu}\right) = \frac{8\pi G}{c^4}T_{\mu\nu}, \tag{1.2}$$

where $R_{\mu\nu}$ is the Ricci tensor, $R = g^{\mu\nu}R_{\mu\nu}$ is the Ricci scalar curvature, $T_{\mu\nu}$ is the energy-momentum tensor, G is Newton's gravitational constant, and c is the speed of light.

GW is derived from Einstein's equation when the metric can be described as the perturbation to the metric $h_{\mu\nu}$ and the Minkowsky metric describing flat space-time

$\eta_{\mu\nu}$, thus

$$g_{\mu\nu} \sim \eta_{\mu\nu} + h_{\mu\nu}. \tag{1.3}$$

In this weak-field regime, Einstein's equation reduces a linearized wave-equation whose solution is represented as

$$h_{\mu\nu}(z,t) = \begin{pmatrix} 0 & 0 & 0 & 0 \\ 0 & -h_+ & h_\times & 0 \\ 0 & h_\times & h_+ & 0 \\ 0 & 0 & 0 & 0 \end{pmatrix} \cos\left[\omega\left(\mathrm{t} - \frac{\mathrm{Z}}{\mathrm{c}}\right)\right], \tag{1.4}$$

where ω is the angular frequency of GW, z is the propagation direction of the wave, h_+ and $h_\times$ are the independent polarization of that. Therefore, GW is the transverse wave propagating with the speed of light.

The two polarizations of GW are known as plus and cross polarizations, and these polarizations change the distance between two points, as shown in Figure 1.1.

1.1.2 Sources of Gravitational-wave

In this section, we briefly describe possible astrophysical GW sources. More detail studies of the sources can be found in reference [2].

Compact Binary Coalescence

Compact binary coalescence (CBCs), such as black holes and neutron stars, emit a characteristic chirp GW signal. The frequency of a chirp GW signal increase as a function of time. This behavior is caused by losing the angular momentum of the system due to the emission of GW.

Advanced LIGO has detected the first GWs from stellar-mass binary black holes (BBHs) in the first observation run (O1), which took place from September 12, 2015, until January 19, 2016. After this observation, Virgo detector joined the Advanced LIGO detectors, and this network has detected the first detection of GWs from a binary neutron star inspiral in the second observation run (O2), which ran from November 30, 2016, to August 25, 2017. Moreover, observation of GWs from a total of seven BBHs [3].

Continuous GWs

Without rotating two objects, asymmetric spinning stars, such as neutron stars and pulsars, could produce detectable GWs, which signal is also well-defined [4, 5].

Burst GWs

In addition to continuous GWs, there are short-duration GWs like a burst event. Supernovae explosions are good candidates to emit te burst GWs [6].

Stochastic GWs

The stochastic background GWs are predicted [7, 8]. This background signal is originated from quantum fluctuations during inflation [9].

1.2 Interferometric Gravitational-wave Detection

The basic design of terrestrial GW detectors is Michelson interferometer [10]. The Michelson interferometer is sensitive to differential changes in the length of both arms, which can measure the expansion and contraction of space due to GWs. Since the interferometer has a wide antenna pattern, it is difficult to determine the direction of arrival by a single interferometer. Therefore, the GW astronomy needs multiple detectors on earth.

1.2.1 Michelson Interferometer

Michelson interferometer converts from the differential optical phase of two lights, which propagate each arm, to the amplitude modulation of single output light. Consider about the interferometer shown in Figure 1.2. Incident light is given as,

$$E_{\text{in}} = E_0 e^{i\omega t}, \tag{1.5}$$

where E_0 is the amplitude, and ω_0 is the angular frequency of the laser field. Two lights split by the Beam Splitter (BS) interfere at the Anti-symmetric (AS) port and Reflection (REFL) port. One can represent the output field at the AS port as,

$$E_{\text{AS}} = -\frac{1}{2} r E_0 e^{i(\omega_0 t - \phi_x)} + \frac{1}{2} r E_0 e^{i(\omega_0 t - \phi_y)}, \tag{1.6}$$

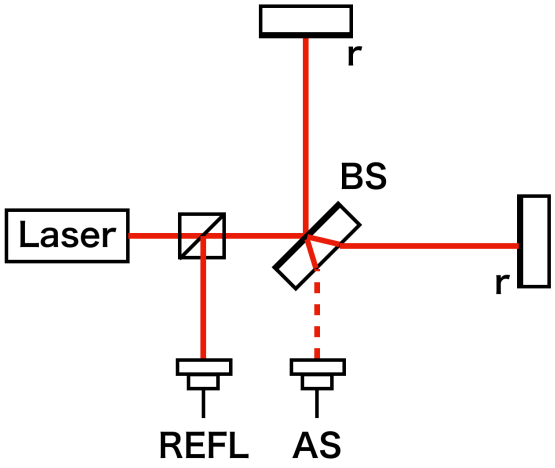

Figure 1.2: Michelson Interferometer.

where r denote the amplitude reflectivity of the end mirrors, and ϕ_x and ϕ_x are the phase delay due to the light traveling in the x and y arms. This output signal can be represented as a single fieled as,

$$E_{\rm AS} = irE_0 e^{i(\omega_0 t-(\phi_x+\phi_y)/2)} \sin\left(\frac{\phi_x-\phi_y}{2}\right). \tag{1.7}$$

We find that the amplitude of the output light is a function of the difference between two phases; $\phi_x - \phi_y$. Here, the power of output light at the AS port is obtained by squaring the Eq.(1.7),

$$P_{\rm AS} \quad = [r\sin(\phi_-)]^2 P_0 \tag{1.8}$$

Similarly, power of the output light as REFL port is written as,

$$P_{\rm REFL} \quad = [(r\cos(\phi_-))]^2 P_0. \tag{1.9}$$

1.2.2 Response to GWs

The Michelson interferometer is sensitive to the quadrupolar strain caused by the gravitational waves shown in Figure 1.1. For example, when the plus mode of the gravitational-wave incidents perpendicularly to change the length of both arms the most, the difference of the optical phase $\Delta\phi_-$ on the arms of length L is given by [11]

$$\Delta\phi_- \sim 2h_+ \frac{2\pi L}{\lambda}. \tag{1.10}$$

Thus, the Michelson interferometer can measure the length change of the space-time caused h_+L by the gravitational-wave.

Figure 1.3 shows an interferometer antenna response for gravitational-waves with puls and cross modes. The interferometer locates at the center with the two arms parallel to the x and y axes. The unpolarized waves is a quadrature sum of the two patterns. The averaged pattern shows that the interferometer has a wide directivity, and means the single detector is difficult to determine the direction of the source in the sky.

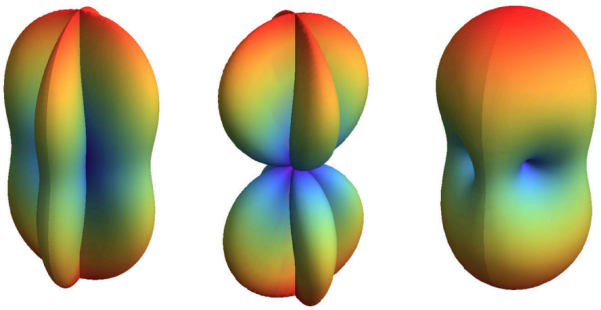

Figure 1.3: Antenna patterns of the Michelson interferometer for the plus-mode (left) , the cross-mode (middle), and unpolarized waves (right) [11].

1.2.3 Multiple Detection for GW Observation

Gravitational-wave observation generates various physics that cannot be obtained by conventional electromagnetic-wave observation, for which multiple detections are indispensable. The detector does not determine the direction of arrival because of its wide directivity. Therefore, a simultaneous observation by multiple instruments is essential for gravitational-wave astronomy. To verify the theory of gravity in a strong gravitational field, it is necessary to investigate the polarization pattern of gravitational waves, which requires four detectors.

Depending on the number of units, we can obtain various physics. Although one or two detectors do not determine the direction of the GW sources, if a neutrino detector exists, we can obtain the core state of the supernovae explosion comparing the time difference between the GW and neutrino signals [**?**]. In the case of three detectors, we can determine the direction. For example, in the neutron star merger event, a gravitational wave signal from the event can be detected before other electromagnetic signals, enabling multi-messenger observations. In four detections, we can determine the

polarization pattern of the GW [**?**]. There are only two polarization patterns in general relativity, but if other polarizations exists, the new polarizations imply the existence of gravity theory beyond general relativity. Furthermore, the four detections also increase the duty cycle in which at least three detectors are operating simultaneously, thereby multi-messenger observation will detect more GWs from compact binary coalescence.

1.3 Enhancement of the Sensitivity

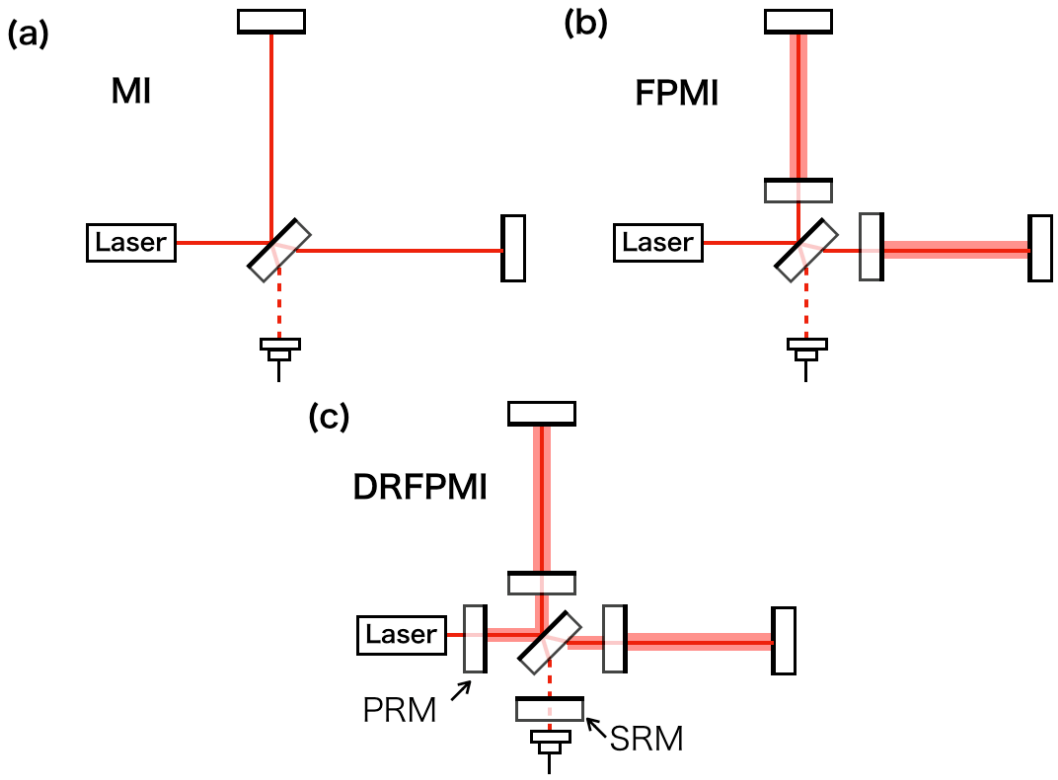

Figure 1.4: Configuration of interferometric GW detector. (a) Michelson interferometer (MI) (b) Michelson interferometer with two Fabry-Perot optical cavities (FPMI). (c) Dual-Recycled FPMI (DRFPMI)

In order increase the sensitivity, current interferometric GW detector use the Dual-Recycled Fabry-Perot Michelson Interferometer (DRFPMI).

1.3.1 Fabry-Perot Michelson Interferometer (FPMI)

According to Eq.(1.10), we need the large-scale interferometer. Fabry-Perot optical cavity enhances the effective arm length of the interferometer.

Fabry-Perot optical cavity increase the effective baseline linegth. Consider the Fabry-Perot optical cavity composed of two mirrors separated by L as shown in Figure 1.5a. In this figure, $E_{\rm in}$, $E_{\rm r}$, $E_{\rm t}$, E are the incident, reflected, and transmitted fields respectively, r_j and t_j are the amplitude reflectivity and transsivity of j-th mirrors ($j = 1, 2$). The averaged bounce number in a Fabry-Perot cavity $\mathcal{N}_{\rm FP}$ is written as [12]

$$\mathcal{N}_{\rm FP} = \frac{2\mathcal{F}}{\pi}, \tag{1.11}$$

where $\mathcal{F}$ is a finesse given as

$$\mathcal{F} = \frac{\pi\sqrt{r_1 r_2}}{1 - r_1 r_2}. \tag{1.12}$$

Here, we note that the arm length enhancement can work in case that the cavity length fluctuation is within the linewidth calculated as the full width at half maximum (FWHM);

$$L_{\rm FWHM} = \frac{\lambda}{2\mathcal{F}}. \tag{1.13}$$

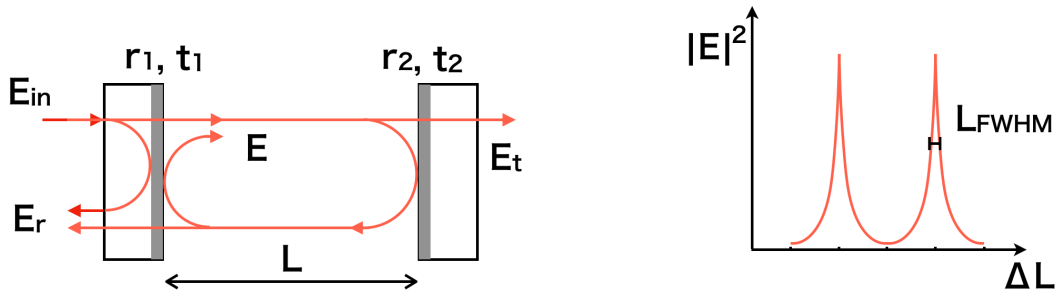

(a) Fabry-Perot optical cavity composed of two mirrors separated by L.

(b) Intra-cavity power as a function of displacement of cavity length.

Figure 1.5: Fabry-Perot optical cavity.

1.3.2 Dual-Recycled FPMI (DRFPMI)

As shown in Figure 1.4(c), the final configuration of the current GW detector is DRFPMI which has two recycling optical cavity [13].

Power Recycle

In order to decrease shot noise, GW detectors use the power recycling technique. In this technique, an additional mirror is installed between the laser and the interferometer to increase the effective laser power by recycling the reflected light from the interferometer. If we increase the laser power, the noise to signal ratio of shot noise decreases as mentioned later.

Signal Recycle

The signal recycling mirror installed on the AS port is for tunning the frequency band of the GW signal. This mirror enhances the GW signal by recycling the output signal from the interferometer.

1.3.3 Noise

In terms of the interferometric GW detector, noise can be classified into two noises; detection noise and displacement noise of the test mass. The former noises are the shot noise, the laser power noise, and laser frequency noise.

Detection noise (Shot Noise)

In an ideal case that the test mass is not disturbed, which means the mass behaves as the free mass, the shot noise limits the noise of the interferometer.

Shot noise is a noise associated with the fluctuation of the number of photons at the photodetector. In case that the number of photons N is large enough ($N \gg 1$), the number of photons obey the Gaussian distribution with the standard deviation of $\sqrt{N}$. Therefore, if laser power P incidents in the detector, shot noise has a relation with the power;

$$P_{\mathrm{shot}} \propto \sqrt{P}. \tag{1.14}$$

One can find that shot noise is a white noise, which propotional to the square-root of the light power P.

Here, the relative error of power at the PD is given by

$$\frac{\Delta P_{\mathrm{AS}}}{P_{\mathrm{AS}}} \propto \frac{1}{\sqrt{P_0}}, \tag{1.15}$$

where $P_{\rm AS}$, $\Delta P_{\rm AS}$ are the power at the PD, P_0 is the power of the incident light. This shows that the increased input laser power can decrease the shot noise. For this reason, we increase the input laser power using power recycling mirror.

laser frequency fluctuation

The actual interferometer has an asymmetricity in the arms, which causes the noise coupling from the laser frequency fluctuation. Thus, before inputting the beam to the interferometer, GW detectors use the frequency stabilization system.

laser power fluctuation

The laser power fluctuation also contaminates the sensitivity of the GW detectors; thus, the intensity stabilization system (ISS) is used for reducing the noise.

Seismic Noise

Seismic noise is the most trouble displacement noise for interferometric GW detectors. Seismic waves from various excitation sources disturb the test mass through the mechanical structures. Therefore, the test masses should be suspended by pendulums to attenuate the seismic noise.

The pendulum used in GW detectors is a multi-stage pendulum designed to have as low an eigenfrequency as possible. The pendulum acts as a mechanical filter. For example, in the case of a single-stage pendulum with a spring constant of k, the frequency transfer function from the ground to the test mass of M can be expressed as

$$H(f) \equiv \frac{1}{1-(f/f_0)^2}, \tag{1.16}$$

where $f_0 = (k/M)^{1/2}$ is the resonant frequency of the oscillator. According to this equation, the vibration isolation ratio is of the second order above the resonance frequency. When the number of stages becomes N, the vibration isolation ratio becomes 2N. Thus, the multi-stage pendulum can and efficiently reduced the ground vibration. In the case of KAGRA, they use a 9-stage pendulum to obtain a sufficient vibration isolation ratio above 10 Hz.

On the other hand, although a pendulum with a lower resonance frequency is required to expand the band in which the pendulum can attenuate, it is limited to the eigenfrequency of less than 1 Hz. In other words, the passive type seismic isolator cannot

attenuate the seismic noise below 1 Hz. Moreover, the low-frequency seismic noises in this band make the operation of the gravitational wave detector unstable.

Newtonian noise

Unlike the seismic noise mentioned above, the Newtonian noise is a noise that the density fluctuation of surrounding objects disturbs the test mass by gravitational interaction [14]. Because this noise propagates through space, the seismic isolation cannot isolate the noise. Although the noise does not affect the current 2nd generation GW detectors, it will contaminate the next 3rd generation detectors.

In order to reduce the Newtonian noise, the feedforward control using the seismometer array has been proposed [15].

Thermal Noise

In addition to external disturbances such as the seismic origin noise, the mirror substrate, and surface particles caused by the random thermal motion also generate displacement noise. This thermal noise has been classified into two; mirror thermal noise and mirror coating thermal noise [16].

The displacement noise of the mirror thermal noise of the mirror with temperature T is given by

$$G_{\mathrm{SB}}(f) = \frac{4k_B T}{\omega} \frac{1-\sigma^2}{\sqrt{\pi} E w_0} \phi_{\mathrm{sub}}(f), \tag{1.17}$$

where k_B is a Boltzmann constant, ω is the angular frequency, σ, E, ϕ_{sub} are a Poisson's ratio, Young's modulus, and mechanical loss angle of the bulk of the mirror respectively, and ω_0 is a beam radius [17, 18]. One can find that the mirror thermal noise is decreased by lower temperature or increase the beam radius.

The displacement noise of coating thermal noise is given by [18, 19]

$$G_{\mathrm{CB}}(f) = G_{\mathrm{SB}}(f) \left(1 + \frac{2}{\sqrt{\pi}} \frac{1-2\sigma}{1-\sigma} \frac{\phi_{\mathrm{coat}}}{\phi_{\mathrm{sub}}} \frac{d}{w_0} \right), \tag{1.18}$$

were d,ϕ_{coat} are depth and loss angle of the coating.

1.4 Duty Cycle of the Terrestrial GW Detectors

In the gravitational-wave observation, which requires simultaneous detection of multiple gravitational waves, a decrease of the duty cycle of each GW detector reduces that of

the entire detector network. As we described in section 3.1.2, the more simultaneous multiple detections, the more physics we can obtain. Thus we need to consider the duty cycle.

The observation of the terrestrial GW detectors is disturbed by seismic motions due to environmental changes. We can classify the none observation state into two states; the lock acquisition state and a state of being unable to do so. In the former state, various methods have been proposed and established in the operation of the detectors to decrease. These methods quickly move the interferometer from an uncontrolled state to a controlled state with low-noise configuration enough to observe. On the other hand, the latter state indicates that the present seismic isolation control is insufficient.

In order to improve the duty cycle, it is necessary to optimize the lock acquisition system and the seismic isolation system. Especially in our study focus on the development of the new seismic isolation system. Before we get into the details of the new system, we first give an overview of the current GW detectors. This section presents an overview of the terrestrial GW detector projects and the duty cycle deteriorated by the seismic motions.

1.4.1 Overview of the GW Detector Projects

There are three generations for GW detectors which are categorized by the difference of the baseline length. These detectors are listed in table 1.1. The first-generation has a baseline length of several hundred meters, the second-generation has several kilometers, and the third-generation has several tens of kilometers. The current working GW detector is the second generation. The third-generation detectors are under planning, but the concept is the underground interferometer using cryogenic mirrors. These two features, underground and cryogenic, are the same as that of KAGRA. KAGRA is the first large-scale cryogenic interferometer constructing in the underground in the GW detector projects, so this detector is also called 2.5 generation GW detector.

1st Generation

The first-generation GW detectors (LISM [23], CLIO [24], TAMA [25], GEO [26]) are small-scale interferometer. Although these detectors have performed scientific operations since 1999, no gravitational wave have detected. The operation was the demonstration of the working principle of the key technology to increase the sensitivity, and these detectors have constrained the upper limits to several gravitational wave sources [27, 28].

Table 1.1: Terrestrial laser interferometers [20, 21]

generation	project	baseline [m]	geological feature
1st	LISM	20	Granite/gneiss
	CLIO	100	Granite/gneiss
	TAMA	300	Sedimentary soil [22]
	GEO	600	Sedimentary rock
2nd	aLIGO L1	4000	Sedimentary soil
	aLIGO H1	4000	Sedimentary rock
	aVirgo	3000	Sedimentary rock
	KAGRA	3000	Granite/gneiss
3rd	ET	10000	(Planning)
	CE	40000	(Under the discussion)

2nd Generation

The second-generation GW detectors (KAGRA[29], Advanced Virgo[30], Advanced LIGO[31]) are the kilo-meter scale interferometers for the enough sensitivity to detect GW signal. The detectors have accomplished not only the first GW detection but also the determination of the direction of arrival, thereby the multi-messenger astronomy was established. As shown in Figure 1.6, the detectors are planning to enhance the sensitivity to reach the design sensitivity of each detector over several years [32].

3rd Generation

The third-generation GW detector has a ten-kilometer scale interferometers. Einstein Telescope (ET) and cosmic explorer (CE) [33] are proposed. It aims to reach a sensitivity about a factor of 10 or more better than the second-generation detectors.

The key features of the third-generation detector are the underground and cryogenic mirrors. These features are also the same as that of KAGRA.

KAGRA

KAGRA is a first large-scale cryogenic interferometer constructing in the underground. The key features of KAGRA were demonstrated in the first-generation detectors; LISM and LISO.

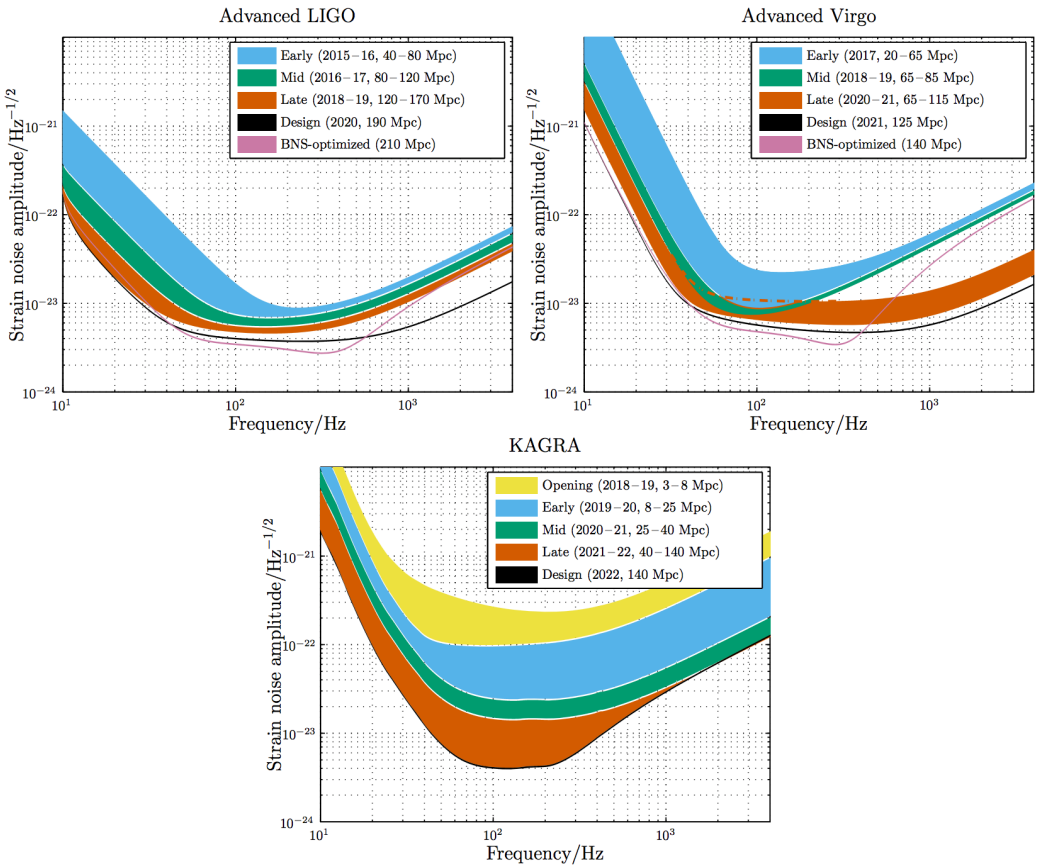

Figure 1.6: Target strain sesitivies of the second-generation detectors [32]

LISM, Laser Interferometer GW Small observatory in a Mine, is a first GW detector in the underground to demonstrate the stable performance of the detector. The detector of LISM is the Michelson interferometer whose arms contain 20 m Fabry-Perot optical cavities. This arm cavity has a high finesse of 25000. Despite such high finesse, the duty cycle was 99.8 %. Such a stable operation is owing to the reduction of the baseline length fluctuation of the bedrock. This reduction effect was confirmed on the sensitivity plot of LISM, as shown in Figure 1.7. In this figure, one can find that the sensitivity of the interferometer is less than the noise projection of the horizontal seismic noise below 6 Hz. In this band, the seismic motion moved the baseline as a single object, which means the less baseline length changes. So, LISM could perform a stable operation.

CLIO, cryogenic laser interferometer observatory, is an interferometer to demonstrate the thermal noise reduction using sapphire mirrors [24]. In order to confirm the

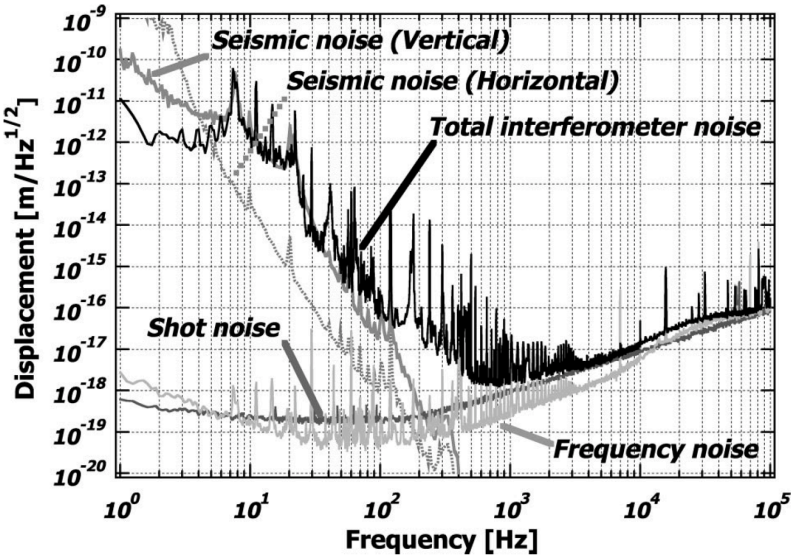

Figure 1.7: The noise equivalent detector sensitivity of LISM [23].

reduction, CLIO is also constructed in the underground to attenuate the seismic noise. Moreover, low-vibration pulse tube cryocooler has developed [34]. Owing to these quiet environment, they demonstrated to reduce the sensitivity limited by the thermal noise using a cryogenic test masses [35].

1.4.2 Duty Cycle

The duty cycle is the observable time of the telescope. For example, in the case of electromagnetic observation, the observation depends on the atmosphere in the bad weather. Even when the weather does not matter, in the case of the radio telescopes, the field of vision is limited, so we, of course, cannot see objects on the other side of the earth. On the other hand, GW observation is highly permeable and can detect in any direction, even underground. However, since the GW detector has a narrow sensor range while having high sensitivity, the sensitivity depends on the condition of the seismic activity. For example, the interferometer status of LIGO detectors during the first observation (O1) is shown in Figure 1.8. The duty cycle of both detectors is about 60%, and the remaining 40% caused by two major unobservable states except for other states including maintenance and commissioning. One is the Locking state, which is a transition state from an uncontrolled state to a low-noise configuration. The other is

a state of uncontrolled due to environmental changes such as earthquakes, microseismic noise, and so on.

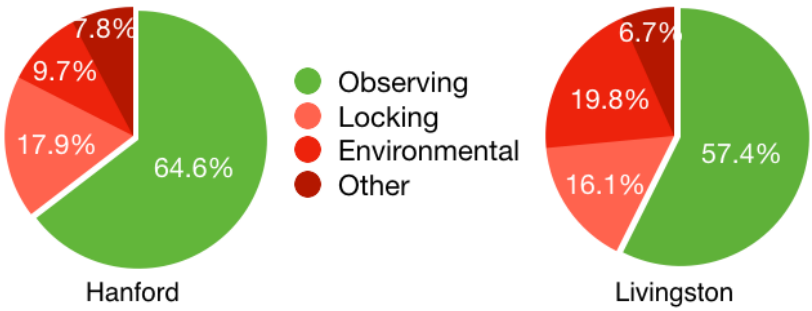

Figure 1.8: Interferometer status of LIGO in O1 [32]. Duty cycle is the observing state. Locking state is the transit state from an uncontrolled state to the lowest noise configuration. Environmental state is the uncontrolled state due to environmental changes. Other includes the planned maintainance and commissioning.

Problematic seismic noises for duty cycle

Seismic noise below approximately 1 Hz is the cause of the deterioration of the duty cycle because the pendulum used in the GW detector is difficult to attenuate insufficiently. In this frequency band, particularly problematic seismic noises include microseismic noise (0.1 - 1 Hz), long-period earthquakes (0.01 - 0.1 Hz), and earth tides (10^{-5} Hz). For example, during the test operation of KAGRA, there was a correlation between the root mean square amplitude of the ground motion and the duty cycle [36]. In the case of LIGO, owing to an active seismic isolation system using seismometers, the duty cycle is not limited mainly by microseismic noise but limited the long-period earthquakes [37]. This degradation occurs because the sensitivity of the seismometers used for the isolation system is insufficient in the earthquake band.

Furthermore, earth tides cause the saturation of control signals of all GW detectors. Insufficient actuator range causes the degradation of the duty cycle due to the low-frequency seismic noise. In principle, it is desirable to use an actuator that is sufficiently strong and has a broad actuator range for controlling the test mass, but this is not the case in practice. The GW detectors should use a weak actuator so that control noise does not contaminate the sensitivity.

The influence of low-frequency seismic noise becomes significant in long-scale interferometers. In the case of the short-scale baseline, the low-frequency seismic noise did not disturb the baseline length because the motion moves the arm cavity as a single object. However, in case the long-scale baseline, the seismic motion below 1 Hz moves the two mirrors of the arm cavity with no correlation. Especially around 0.2 Hz, the amplitude of microseisms caused by ocean activities exceeds the linewidth of the arm cavity. Thus, the low-frequencies seismic noises directly limit the duty cycle of interferometric GW detectors.

Therefore, the low-frequency seismic noise below 1 Hz is a significant problem that decreases the duty cycle. This is an unavoidable problem for the GW detectors aiming for the more lengthened baseline.

Improvement of duty cycle

The way to increase the duty cycle is to reduce the locking time and to improve the vibration isolation performance in the low-frequency band.

Arm length stabilization (ALS) is the technique to reduce the locking time. This technique reduces the RMS of arm cavity length using frequency-doubled auxiliary lasers before locking the cavity using the main infrared laser [38, 39]. The wavelength of this auxiliary laser is half of the main infrared laser. Since the linewidth is also half according to Eq.(1.13), the auxiliary laser is more comfortable to lock the arm cavity than the main laser. Once locking the arm cavity using the auxiliary laser, the ALS system can reduce the RMS of arm cavity length fluctuation using the feedback signal of the auxiliary system so that the main laser can lock the arm cavity. Owing to this system, lock acquisition end within about 10 minutes.

Although the ALS system can bring the interferometer to the observation state in a sufficiently short time, we cannot use the system in the observation phase due to the high control noise. In the observation state, we can only use the main laser with narrow linewidth as a sensor for measuring the baseline length. Moreover, we have to use a narrow dynamic range and weak actuator not to contaminate the GW sensitivity with the actuator noise. In this situation, if the seismic disturbances exceed the range of the sensors and the actuators, the cavity can not keep the locking state.

An active seismic isolation system has been developed to reduce the RMS amplitude of the arm cavity length during the observing state. This active system is used to isolate low-frequency seismic noise that is not attenuated in passive pendulum systems,

which is described in chapter 4. However, the current active vibration isolation systems are capable of vibration isolation only up to microseismic noise due to the insufficient sensitivity band of the inertial sensor used for control.

In LIGO, the duty cycle is diminished due to an earthquake shaking the ground in the lower band. When the interferometer lost the locking by an earthquake, it takes several hours to return to the observing state. In order to prevent the lock loss, the LIGO detector switches the control filter just before the earthquake hits the site [37]. Although this control filter introduces control noise above the microseismic band, this reduces the enhancement of the RMS amplitude in the earthquake band. The control filter is optimized to improve the duty cycle when earthquakes come.

1.5 Outline of thesis

The goal of this study is to improve the duty cycle of GW detectors by isolating the low-frequency seismic noises. We have developed a vibration isolation system for seismic noises. In this thesis, two main topics are described. One is a study of the influence of the low-frequency seismic noise to the large-scale GW detectors. This study shows that the baseline fluctuation is somehow reduced due to a correlated motion at two separate points, and this correlation decrease in the large-scale baseline. For this reason, large-scale GW detectors are suffering from seismic noise. This problem is happening even in the underground. Another topic is the development of the baseline compensation system to reduce residual motion. The feature of this new system is the feedforward control using a strainmeter installed in parallel to the KAGRA baseline, which is named geophysics interferometer (GIF). GIF has been developed for monitoring the deformation of the baseline directly with high sensitivity. The new system compensates for the baseline fluctuation of the arm cavity by using the GIF strainmeter signal.

In chapter 2, we describe the properties of the seismic noise. The GIF strainmeter's working principle and design are described in chapter 3. After that, we describe the baseline compensation system comparing with the current system in chapter 4. In chapter 5, the demonstration of this new system implemented on the KAGRA X-arm cavity, and the result is described. At the end of the thesis, chapter 6, we describe a conclusion and future directions.

Chapter 2

Seismic Noise

Seismic noise produces two types of problems for laser interferometric gravitational-wave detectors: it limits the low-frequency sensitivity and deteriorates the duty cycle. The former problem happens above 1 Hz and is associated with an anthropogenic activity. In order to reduce this human-induced seismic noise, constructing the detectors in the underground is an effective way because of far from human activity. On the other hand, the latter problem happens below 1 Hz and is generated by natural noise sources, such as the motion of the ocean, earthquakes, and earth tides. The underground environment, in contrast, cannot attenuate the lower-frequency seismic motions due to not local noises but global disturbances.

Regarding the low-frequency seismic noises, the property of the elastic waves on the ground, such as the common-mode rejection, effectively reduces the noises. The low-frequency elastic waves tend to shake the whole detector as a single object because the wavelength of the wave is several kilometers or more. Thus, the common-mode rejection effect appears in the small-scale GW detector such as LISM whose baseline is 20 m. For this reason, the LISM was able to operate stably due to the effect. However, this effect decreases in the large-scale baseline detectors, not only for current km-scale detectors but also for the planned Cosmic Explorer (CE) [33] and Einstein Telescope (ET) [40] whose baseline length is several ten km-scale.

Section 2.1 offers a theoretical understanding of seismic noise as elastic waves. Section 2.2 describes some general properties of seismic noise. Finally, we discuss the problem in section 2.3.

2.1 Properties of seismic waves

The ideal ground for GW detectors that must keep the optical cavity length constant is a *rigid ground* that does not stretch or contract the baseline length. The ground moves its center of mass without deformation when an external force is applied to the ground. In practice, however, the ground medium has elasticity and produces elastic waves when an external force is applied. The phase velocity of the elastic wave is finite. Thus a difference occurs in the displacement between two distant points. This becomes a baseline length fluctuation.

This section describes the baseline length fluctuation caused by elastic waves. We begin with the basic elastic waves in Section 2.1.1. Section 2.1.2 discusses how elastic waves cause baseline length expansion and contraction for different length baselines, and shows that the longer baseline is more susceptible to the low-frequency seismic waves.

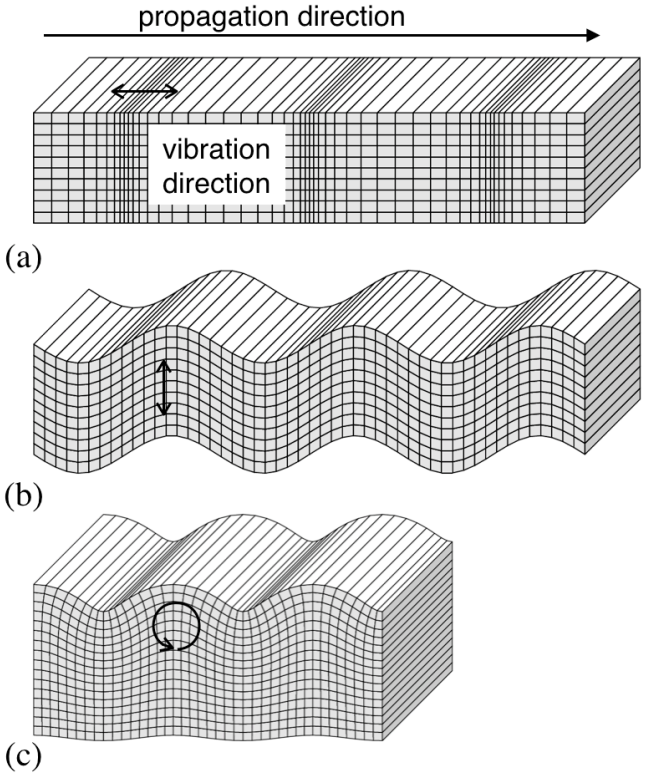

Figure 2.1: (a) longitudinal wave known as P-wave (b) transverse wave known as S-wave (c) Rayleigh wave [41].

2.1.1 Seismic Waves

Seismic waves can be roughly categorized into body waves and surface waves. Body waves are the elastic waves propagating in a medium, and surface waves are the elastic waves propagating at a boundary between two different media. These elastic waves have different propagation methods and different phase velocities.

For simplicity, consider the seismic waves propagating in the homogeneous medium without external forces. The elastodynamic wave equation is given by

$$\rho\ddot{\boldsymbol{u}} = (\lambda + 2\mu)\nabla(\nabla \cdot \boldsymbol{u}) - \mu\nabla \times (\nabla \times \boldsymbol{u}), \tag{2.1}$$

where $\boldsymbol{u}$ is the displacement field vetor of the medium, ρ denotes density of the medium, and λ, μ are Lame's first and second parameter [42].

Body Waves

From Eq.(2.1), we can obtain two characteristic waves; longitudinal wave and transverse wave. Using Helmholtz's decomposition, we represent the displacement field vector $\boldsymbol{u}$ as

$$\boldsymbol{u} = \nabla\phi + \nabla \times \boldsymbol{\psi}, \tag{2.2}$$

where ϕ is the scalar potential, and $\boldsymbol{\psi}$ is the vector potential. The first term shows the seismic wave with changing the volume of the media, and the second term shows the seismic wave without changing that. Substitute Eq.(2.2) into Eq.(2.1) and after some vector algebra, one can obtain two wave equations;

$$\ddot{\phi} = v_L^2\nabla^2\phi, \tag{2.3}$$
$$\ddot{\psi} = v_T^2\nabla^2\psi, \tag{2.4}$$

where v_L, v_T are defined as

$$v_L = \sqrt{\frac{\lambda + 2\mu}{\rho}}, \; v_T = \sqrt{\frac{\mu}{\rho}}. \tag{2.5}$$

Because the scalar potential and the vector potential are obey the wave equation Eq.(2.3) and Eq.(2.4) respectivly, the general solutions of these potentials are given as

$$\phi = \phi_0(\omega t - \boldsymbol{k} \cdot \boldsymbol{x}) \tag{2.6}$$
$$\boldsymbol{\psi} = \boldsymbol{\psi_0}(\omega t - \boldsymbol{k} \cdot \boldsymbol{x}), \tag{2.7}$$

where ω, $\boldsymbol{k}$ are the angular frequency and the wave vector, respectively. One can obtain the divergence component of the displacement filed vector $\boldsymbol{u}$ as

$$\boldsymbol{u}_{\mathrm{div}} = \nabla\phi_0(\omega t - \boldsymbol{k}\cdot\boldsymbol{x}) = -\boldsymbol{k}\phi. \tag{2.8}$$

The displacement vector $\boldsymbol{u}_{\mathrm{div}}$ whose phase velocity is v_L propagates along with direction of the wave vector. This means that v_L is the phase velocity of a longitudinal wave. On the other hands, one can obtain the curl component of $\boldsymbol{u}$ as

$$\boldsymbol{u}_{\mathrm{rot}} = \nabla\times\boldsymbol{\psi_0}(\omega t - \boldsymbol{k}\cdot\boldsymbol{x}) = -\boldsymbol{k}\times\boldsymbol{\psi}. \tag{2.9}$$

This displacement vector $\boldsymbol{u}_{\mathrm{rot}}$ whose phase velocity is v_T is perpendicular to the wave vector. Thus, v_T is the phase velocity of a transverse wave.

The phase velocity of the longitudinal wave v_L is higher than that of the transverse wave v_T;

$$v_L > v_T. \tag{2.10}$$

because λ and μ are positive numbers. Therefore, the former wave is called primary wave (P-wave), and the latter wave is called secondary wave (S-wave) due to the time delay of arrival. Figure 2.1 shows the ground motion caused by P and S waves.

Surface Wave (Rayleigh waves)

If there is a free surface such as the ground surface, the surface wave propagates on the surface. Here, we particularly describe surface waves called Rayleigh waves. Figure 2.1 shows the ground motion caused by the Rayleigh wave. As shown in Figure 2.6, consider a seismic wave propagating in the x-axis direction in a semi-infinite homogeneous medium. In this figure, P-wave and S-wave which are oscillating in the x-z plane exist. Assuming that these waves propagate at the same phase velocity c_R, the velocity can be expressed as a Rayleigh wave equation given as

$$\left(\frac{c_R^2}{c_S^2}\right)^3 - 8\left(\frac{c_R^2}{c_S^2}\right)^2 + 8\left(3-\frac{2}{\gamma^2}\right)\left(\frac{c_R^2}{c_S^2}\right) - 16\left(1-\frac{1}{\gamma^2}\right) = 0, \tag{2.11}$$

where c_{S} is the phase velocities of the S-wave, and $\gamma \equiv c_{\mathrm{P}}/c_{\mathrm{S}}$, where c_{P} is the phase velocity of the P-wave [42]. In the case that $0 < (\frac{c_R^2}{c_S^2}) < 1$, the velocity has a physically meaningful value. We can calculate the phase velocity of the Rayleigh waves if the velocity of the both P-wave and S-wave. According to Eq.2.11, the ratio $\frac{c_R}{c_S}$ is a function

of the ratio γ. For example, because the phase velocity of P-wave and S-wave are $5.54 \pm 0.05\,\mathrm{km/s}$ and $3.05 \pm 0.06\,\mathrm{km/s}$, respectively, according to measurements in Kamioka mine [43]. Thus, the phase velocity of the Rayleigh wave almost $3\,\mathrm{km/s}$ in the Kamioka mine.

Depth dependence of the amplitude of the Rayleigh wave

The displacement amplitude of the Rayleigh wave depends on the depth. Figure 2.3 shows the amplitude of the Rayleigh wave in the x and z directions (u_x, u_z) as a function of the depth z' normalized by the wavelength of the Rayleigh wave [42]. From this figure, it can be seen that the x component of the Rayleigh wave decreases at a depth of 1/4 wavelength. Therefore, the underground environment can reduce seismic noise caused by Rayleigh waves. In the underground environment, the horizontal motion of Rayleigh waves, which are surface waves, can be reduced, but P waves and S waves, which are body waves, cannot be reduced in such way.

The vibration component which is a problem for the gravitational wave detectors is the baseline length expansion and contraction represented by the differential component of the horizontal motion between two points. Fortunately, this component can be reduced.

2.1.2 Common Mode Rejection of the Baseline

The low-frequency seismic motion having a long wavelength is easy to move two distant points in the same phase, so that the variation of the baseline length, which is the opposite phase, is reduced. In this subsection, such a common mode rejection effect is discussed by assuming that the seismic wave is a plane wave.

Consider the motion of the ground whose displacement is given by the displacement field $\boldsymbol{u}(t, \boldsymbol{x})$, where t is time and $\boldsymbol{x}$ is the position vector.

Differential Motion and Common Motion

We define the motion of two points shown in Figure (2.4) as $\boldsymbol{u}_1 = \boldsymbol{u}(t, \boldsymbol{x}_1)$ and $\boldsymbol{u}_2 = \boldsymbol{u}(t, \boldsymbol{x}_2)$, respectively, where x_1 and x_2 are the position vector of each points. The motion of the two points can alternatively be represented as the differential motion and

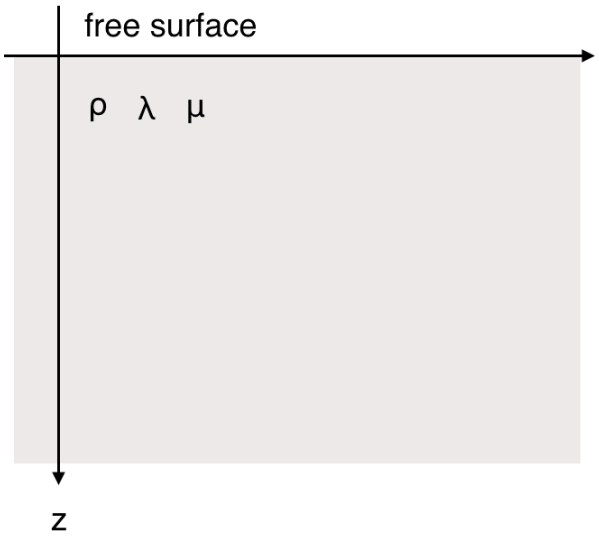

Figure 2.2: Semi-infinite medium. Where $z < 0$, homogeneous medium fill the space with density ρ and Lame's first and second parameter; λ and μ. Where $z = 0$, there are free surface.

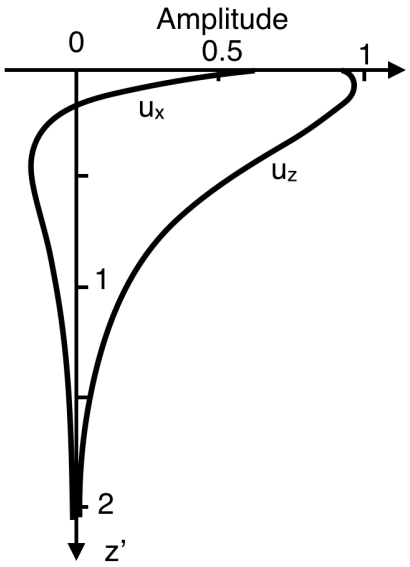

Figure 2.3: Depth dependance of the amplitude of the Rayleigh wave cited from [42]. u_x, u_z are the amplitude of the Rayleigh wave which given by Eq. in the case $\lambda = \mu$. z' is the normalized depth given by $z' = z/(k/2\pi)$, where z is the depth and k is the wavevector of the Rayleigh waves.

the common motion defined as

$$\boldsymbol{u}_{\text{diff}} \equiv \frac{\boldsymbol{u}_1 - \boldsymbol{u}_2}{\sqrt{2}}, \tag{2.12}$$

$$\boldsymbol{u}_{\text{comm}} \equiv \frac{\boldsymbol{u}_1 + \boldsymbol{u}_2}{\sqrt{2}}. \tag{2.13}$$

These two components are normalized by $\sqrt{2}$ to conserve the total power.

Common and Differential Motion Ratio (CDMR)

To discuss the common-mode rejection effect, we define the power ratio of the common motion over the differential motion as common and differential motion ratio (CDMR).

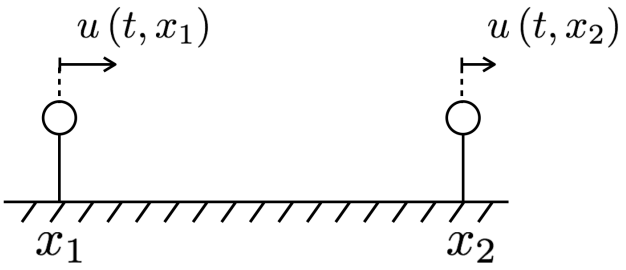

Figure 2.4: The two points are sparated by a distance L along the X axis. $\boldsymbol{u}(t, \boldsymbol{x})$ is the displacement field vector, where t denotes the time and $\boldsymbol{x}$ denotes the location vector.

The power spectrum density (PSD) of CDMR is given by

$$\mathrm{CDMR} \equiv \sqrt{\frac{\mathrm{Common\,Motion}}{\mathrm{Differential\,Motion}}} = \sqrt{\frac{P_{\mathrm{comm}}(\omega)}{P_{\mathrm{diff}}(\omega)}} \tag{2.14}$$

where $P_{\mathrm{comm}}, P_{\mathrm{diff}}$ are the PSDs of the differential and common motions, respectively. This ratio is useful to describe how the differential motion is reduced in the baseline compared to the common motion.

To obtain these PSDs, we convert from the autocorrelation function of these. Therefore, autocorrelation function C_{diff} of the differential motion is given by its definition in Eq.(2.13)

$$C_{\mathrm{diff}}(\tau) = \frac{1}{2}\left\langle \Big[u_1(t) - u_2(t)\Big]\Big[u_1(t+\tau) - u_2(t+\tau)\Big] \right\rangle \tag{2.15}$$

$$= \frac{1}{2}\Big[C_{11}(\tau) - C_{12}(\tau) - C_{21}(\tau) + C_{22}(\tau)\Big], \tag{2.16}$$

where C_{ij} are the autocorrelation functions of each point and defined as $C_{ij} \equiv \langle u_i(t) u_j(t+\tau)\rangle$, $(i = 1, 2,\ j = 1, 2)$. Here, one can obtain the power spectrum density of differential motion $P_{\mathrm{diff}}(\omega)$ as

$$P_{\mathrm{diff}}(\omega) = \frac{1}{2}\Big[P_1(\omega) + P_2(\omega) - P_{12}(\omega) - P_{12}^*(\omega)\Big] \tag{2.17}$$

$$= \frac{1}{2}\Big[P_1 + P_2 - \mathrm{Re}\,[\mathrm{coh}] \times 2\sqrt{P_1 P_2}\Big], \tag{2.18}$$

where $P_1(\omega), P_2(\omega)$ are the PSDs of each points, and $P_{12}(\omega)$ are the cross spectrum between the two points. The parameter coh is the complex coherence between them defined by

$$\text{coh} \equiv \frac{P_{12}}{\sqrt{P_1 P_2}}. \tag{2.19}$$

Furthermore, assuming that seismic wave propagating each points does not decay, which means $P_1 = P_2 \equiv P$, one can compute the $P_{\text{diff}}(\omega)$ as

$$P_{\text{diff}}(\omega) = P(1 - \text{Re}\,[\text{coh}]). \tag{2.20}$$

Similarly, the PSD of the common motion can be calculated as

$$P_{\text{comm}}(\omega) = P(1 + \text{Re}\,[\text{coh}]). \tag{2.21}$$

Finaly, the PSDs of the CDMR defined Eq.(2.14) in the case that the seismic wave is plane wave is represented as

$$\text{CDMR} = \sqrt{\frac{1 + \text{Re}\,[\text{coh}]}{1 - \text{Re}\,[\text{coh}]}}\,. \tag{2.22}$$

Eq.(2.22) indicates that CDMR can be expressed by only the coherence coh between of two points. For example, CDMR tends to be larger when coh close to 1. This means that the differential motion is less than the common motion because the two points move together in the same direction. This means that the common mode rejection effect.

Uniform Plane Wave Model

Consider the PSD of the CDMR when the plane waves are distributed uniformly around the azimuth. This case is true when the seismic noise sources are distributed uniformly. The coherence in the case that the single plane wave propagating with the azimuth angle θ along the direction of the x-axis in Figure (2.5) is given by

$$\text{coh} = \exp\left[i\frac{L\cos\theta\omega}{c}\right], \tag{2.23}$$

where L is the distance between the two points.

The coherence in case that the plane waves propagates uniformly is given by the integral of Eq.(2.23) overall direction;

$$\text{coh} \;=\; \frac{1}{2\pi}\int_{-\pi}^{\pi} e^{i\frac{\omega}{c}L\cos\theta} d\theta = J_0\left(\frac{L\omega}{c}\right). \tag{2.24}$$

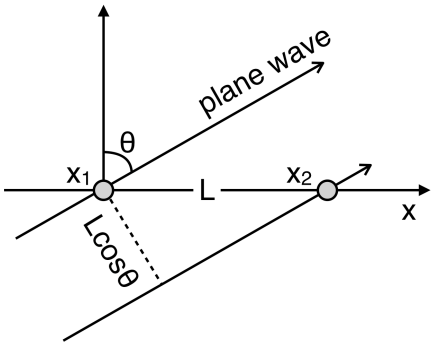

Figure 2.5: Single plane wave passing through two points with azimuth angle θ. Top view of Figure 2.4.

where the coherence is normized azimuth angle. Therefore, the PSD of the CDMR is given as

$$\mathrm{CDMR} = \sqrt{\frac{1 + J_0(\frac{L\omega}{c})}{1 - J_0(\frac{L\omega}{c})}}. \tag{2.25}$$

Comparison with different baseline length

We show how the effect of common-mode rejection differs from the baseline length. The CDMR comparison with LISM, CLIO, KAGRA is shown in Figure 2.6. We assume that the uniform plane wave model with the phase velocity of 3 km/s, which means the uniform Rayleigh waves in the Kamioka mine. One can find that KAGRA which is the km-scale detector has few CDMR below 0.1 Hz than the other short-scale detectors. This means that the effect of the common-mode rejection is reduced on the long baseline. Thus, the ground vibration below 1 Hz is more significant than on the short baseline.

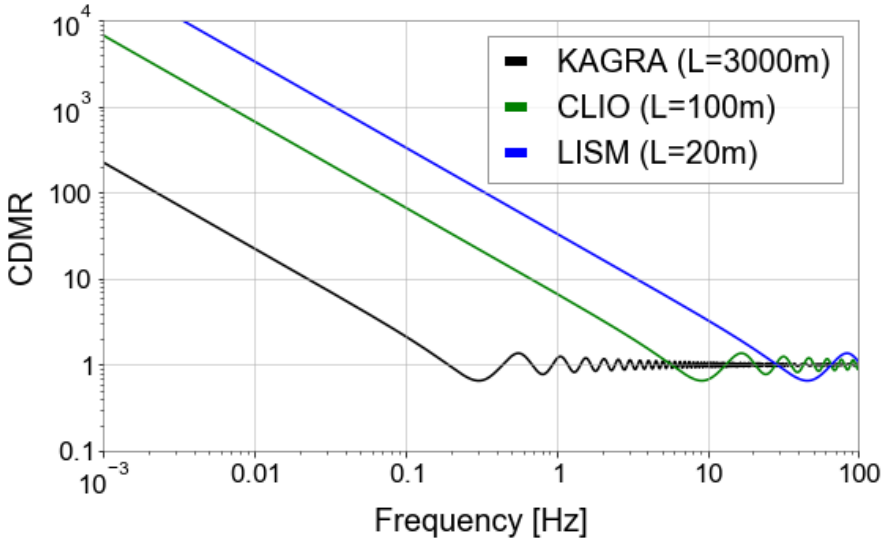

Figure 2.6: CDMR given in Eq.(2.25), of the underground GW detectors assuming the uniform plane waves model with phase velocity of 3 km/s. Black is the CDMR of KAGRA with the 3000 m baseline, green is the CDMR of CLIO with the 100 m baseline, and blue is the CDMR of LISM with the 20 m baseline.

2.2 Seismic Noise

In this section, we introduce the noise source of the seismic motion. Characteristics of the seismic noise are related to its origin spatially and temporally. The noise sources are spread anywhere; footsteps, traffic, ocean waves, and these amplitude depends on day-night or weather condition.

As summarized in Table 2.1, the seismic noises above 1 Hz are clearly correlated with cultural activities, and that below this frequency are excited by the natural phenomena [44].

Table 2.1: Two types of seismic noise

Type of noise	Frequency Band	Sources
Cultural Noise	> 1 Hz	traffic, machinaries, foot steps
Natural Noise	< 1 Hz	ocean, air pressure, earth tides

This boundary frequency between cultural or natural depends on the soil structure.

At the sediment site such as the LIGO [45] and Virgo site [46], the cultural noise can be shifted to a lower frequency and appear below 1 Hz. On the other hand, at the hard rock site such as the KAGRA site, the cultural noise can be distinguished from the natural noise for its diurnal variability and apparent only above 1 Hz.

2.2.1 Cultural Noises

The cultural seismic noise contaminates the sensitivity of gravitational-wave detectors in the frequency range of interest for gravitational-waves sources, above 1 Hz. In this frequency band, cultural noise is dominated by human activities. For example, seismic noise from traffic near the detectors is reported at the LIGO site [47].

2.2.2 Natural Noises

The natural seismic noise affects the stability of the GW detectors below 1 Hz. These natural noises depend on the location. Figure 2.7 shows the noise spectra of the seismic noise measured by Peterson in 75 stations in the world [48]. The new high noise model (NHNM) is a spectrum of the average of high background noise power in the stations. The primary contributions to the NHNM are coastal stations and inland stations on the soft soil. On the other hand, the new low noise model (NLNM) represents the seismic noise when microseismic is quiet. Especially, below 0.1 Hz, it represents the global seismic noise floor [49].

Microseisms

Microseisms whose power peaked in the frequency range of 50 – 200 mHz are excited by oceanic waves. These seismic waves can be categorized by generating mechanism [50]. The primary ocean microseisms are produced only in shallow waters in coastal regions. In these regions, the water wave energy can be converted directly into seismic energy either through vertical water pressure variations or by the impacts of the surf on the shores. Thus, there is a correlation between this microseismic peak and the swell at the beaches was known from the data sets studied by [51]. The secondary ocean microseisms could be explained by the superposition of ocean waves of equal period traveling in opposite directions. Therefore, generating standing gravity waves of half the period [52].

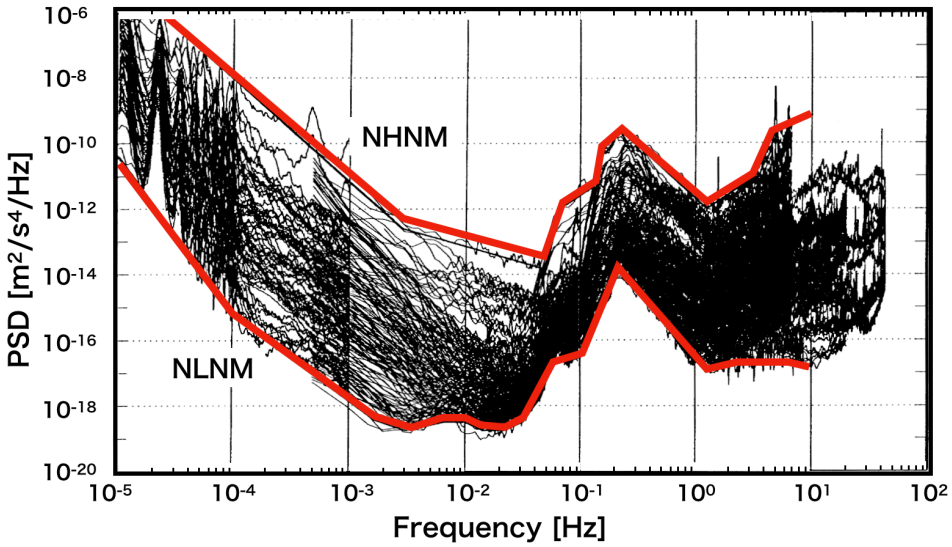

Figure 2.7: PSDs of the seismic noise obtained by Peterson in 75 stations in the world [48]. Each of the black solid lines are PSDs divided into 5 different frequency band at the each stations. Each red lines are the new high noise model (NHNM) and the new low noise model (NLNM), respectively.

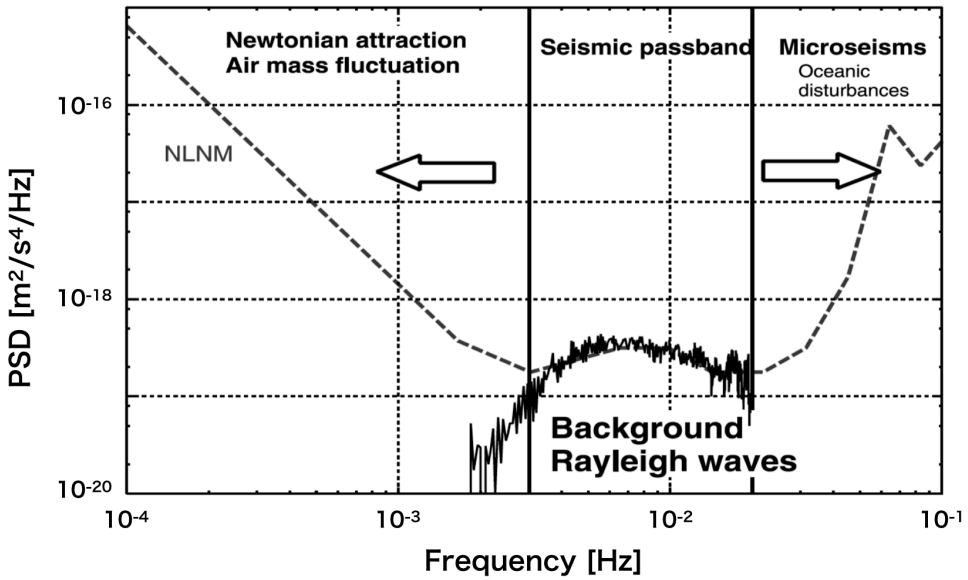

Figure 2.8: Noise contribution below 100 mHz [49].

Seismic Noise Below 20 mHz

Below the microseismic band, the main seismic noise source is an atmospheric pressure change; Rayleigh waves excited by air fluctuation on the surface, and the deformation of the Earth's crust caused by the Newtonian attraction of air mass fluctuation [53, 54]. Figure 2.8 shows PSDs of the NLNM and the seismic motion excited by the Rayleigh waves [49]. The noises caused by Rayleigh waves are consistent with the NLNM between 2 Hz and 30 mHz. The noises caused by the Newtonian attraction are increased PSD increases rapidly with decreasing frequency below two mHz.

Although Seismic motion in this band is usually quiet, large earthquakes often excite the ground in this band [55, 56].

Earth tides

At even lower frequencies, the earth deformed by tidal forces due to the attraction of Sun and Moon in diurnal and semi-diurnal periods [57].

2.3 Seismic Noise in the KAGRA Mine

In this section, we characterized the seismic noise in the KAGRA site by using a seismometer installed at the site. Section 2.3.1 described the seismometer and signal acquisition system. Section 2.3.2 compared the seismic noise in KAGRA with the typical noise in the world. Section 2.3.3, we discuss the common-mode rejection effect observed in the X and Y arms in KAGRA comparing with a simple model.

2.3.1 Experimental Arrangement

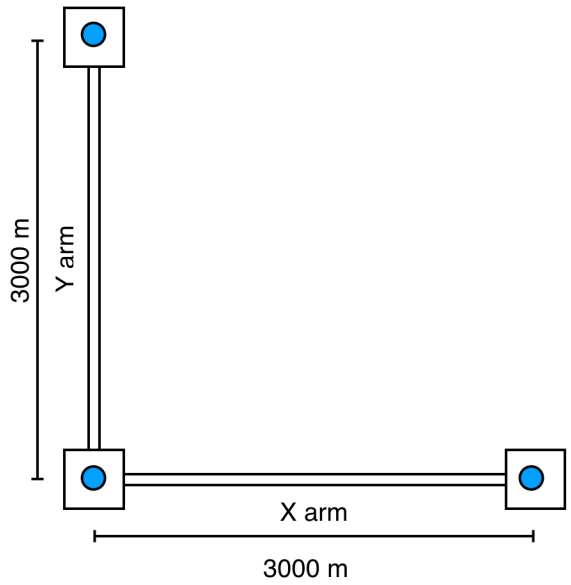

Figure 2.9: Location of the seismometers (blue). KAGRA has three stations which are separated with 3 km; X-end, Y-end, and corner stations.

Seismometers Array

The Trillium 120-QA which is a three-axis, very broadband, and low-noise seismometer, is used. These three outputs are proportional to the ground velocity of two horizontal and one vertical, respectively.

The seismometer is housed in the black thermal insulation cover, as shown in Figure 2.10. Thermal insulation protects two broad categories of thermal couplings that can

Figure 2.10: Trillium 120-QA installed on the second floor at X-end area, which is coverd by black thermal insulation cover

cause unwanted noise [58]. First is the direct coupling to the sensitivity. This coupling typically increases the noise of the vertical channel as a periodic diurnal variation caused by the day-to-night temperature cycle, because the springs that suspended the inertial masses are temperature sensitive. The second is the coupling to tilt from the thermal fluctuation. Tilt converts the vertical acceleration of gravity into horizontal acceleration. This thermally induced tilt noise on the horizontal will be larger than the direct thermal coupling on the vertical channel. To be low sensitivity to both tilt and temperature, this model has a function to center the inertial mass after the initial installation.

The signals of the seismometer are recorded through the data acquisition system developed by LIGO [59]. The analog signal is converted to a digital signal by the 16-bit analog-to-digital converters (ADC) with 16384 Hz sampling. This analog signal is amplified with 30 dB so that the ADC noise does not mask this signal.

Data Processing

The estimation of the amplitude spectrum densities is calculated by the average of 32 segments with 50% overlapping. The single segment has $256\,(2^8)$ sec. The FFT calculation of each segment is done after detrending the linear trend and multiplying the Hanning window.

The error bars of this spectral is calculated by chi-square distribution. For example, the spectrum averaged by 32 obeys the chi-square distribution with 32 degrees of

freedom. The confidence interval of $100(1-\alpha)\,\%$ with degrees of freedom ν is given by

$$\frac{\nu\hat{G}(f)}{\chi^2(\nu, 1-\frac{\alpha}{2})} \leq G(f) \leq \frac{\nu\hat{G}(f)}{\chi^2(\nu, \frac{\alpha}{2})}, \tag{2.26}$$

where f is the frequency and $\hat{G}(f)$ is estimator of spectrum. Therefore, the confidence level of 95% is

$$\nu/\chi^2(\nu, 1-\frac{\alpha}{2}) \leq G(f)/\hat{G}(f) \leq \nu/\chi^2(\nu, \frac{\alpha}{2}). \tag{2.27}$$

In case that degrees of freedom is 32, the spectral point lies within 0.65 to 1.75 of the estimates.

2.3.2 Study of Long-term Seismic Noise

It is known from the measurement by Peterson that the seismic noise varies from place to place. In this subsection, we compared the stationary seismic noise of KAGRA obtained in one year with Peterson's measurements.

Long-term seismic noise is measured by a seismometer installed on the second floor of the X-end station. This area is placed 200 m underground from the surface of the mountain. In comparison to the corner area, human activity in the end area is less because the corner area has parking lots. In comparison to the Y-end area, there is no entrance connected to other mines. Therefore, the X-end area is relatively quiet in the KAGRA mine, regarding the seismic noise induced by human activity.

We estimated the noise spectral using the one-year data, which does not include the glitch noises such as the earthquake or circuit noise. Figure 2.11 shows the amplitude spectral densities (ASDs) of the horizontal and vertical components of the acceleration. Below 40 mHz, the horizontal noise is much larger than the vertical noise due to noise arise by temperature fluctuation, and the ten percentile of vertical noise is close to Peterson's NLNM estimation. This means that the KAGRA mine is also quiet with respect to anthropogenic noise enough to measure the background seismic noise floor in this band. From 40 mHz to 1 Hz, in the microseismic noise band, the ten percentile of both components are middle of the NHNM and NLNM. This indicates that the microseismic in KARGA is not quieter than that in the inland station because the KAGRA site is located on 40 km far from Toyama bay. Above 1 Hz, both components are close to the NLNM due to the underground environment.

In the environment of KAGRA, human-induced seismic noise above 1 Hz is quiet and approaches NLNM, but the seismic noise in the microseismic noise band is located

in the middle of NHNM and NLNM. Thus, the effect of microseismic noise is not small, even in the underground.

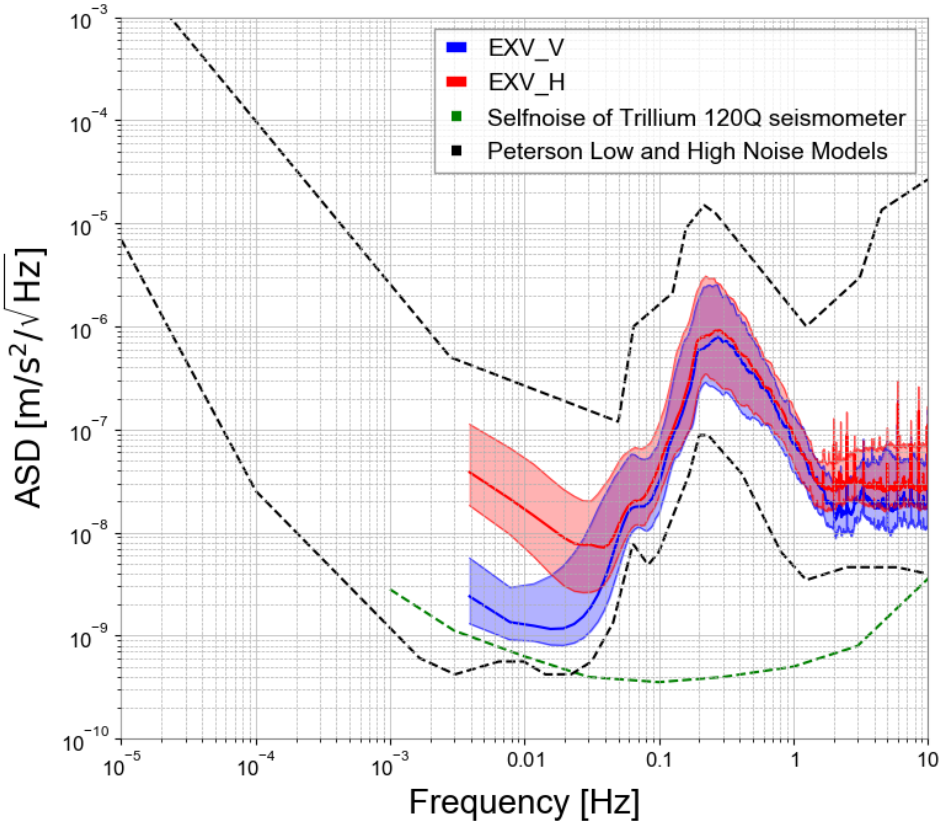

Figure 2.11: The seismic noise in KAGRA mine. Red and blue are the amplitude spectral densities (ASDs) of horizontal and vertical components of the ground motion, respectively. Each component are shown by the 90, 50, 10 percentile of their ASDs, in order from top to bottom.

2.3.3 Study of the Common Mode Rejection

We have evaluated the common-mode rejection effect for the 3 km arms of KAGRA. For that purpose, we calculated the CDMR given by Eq.(2.14), using two seismometers pairs; the X-end and corner stations, and the Y-end and corner stations in Figure 2.9. For example, the differential (solid line) and common motion (dashed line) of the X-arm are calculated by the X-axis of each seismometer signal, which is proportional to the ground velocity.

The top of Figure 2.12 shows the common and differential motion of the ground velocity. In this figure, ASDs of the velocity of the differential (solid line) and the common motion (dashed line) are shown. The red and blue indicate the motions of X-arm and Y-arm, respectively. As a reference, the black dashed line shows the self-noise of the Trillium 120Q broadband seismometer multiplied $\sqrt{2}$. Below 0.05 Hz, the ASDs are limited by the thermally induced tilt noise which is mentioned in section 2.3.1.

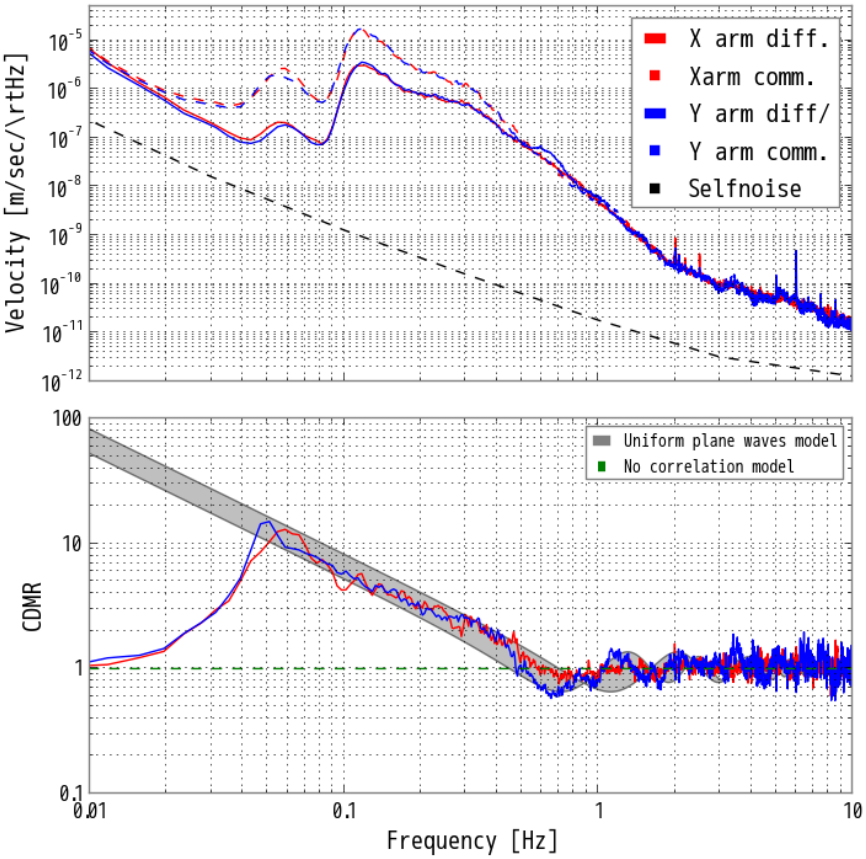

Figure 2.12: Comparison with the measured CDMR and the CDMR assumed the uniform plane waves model.

The bottom of Figure 2.12 shows the comparison of the measured CDMR and the CDMR assumed a uniform plane wave model. The measured CDMR is given as red and blue solid lines whose colors indicate the X-arm and Y-arm, respectively. As a

reference, the gray line indicates the CDMR assuming the uniform plane waves model in case the phase velocity is in the region from $5 - 3\,\mathrm{km/sec}$, and green dashed line is the CDMR assuming the no correlation between each endpoint of the baseline. The measured CDMR is consistent with the uniform model in $0.05 - 0.5\,\mathrm{Hz}$. Below this band, the CDMR is close to the no correlation model due to the noise of the seismometers. Below and above this band, the measured CDMR is consistent with the no correlation model.

Chapter 3

Geophysics Interferometer (GIF)

As shown in Figure 3.1, GIF is a 1500 m laser strainmeter installed along the KAGRA X-arm. The laser strainmeter is an asymmetric Michel-son interferometer with 0.5 m and 1500 m arms, which measure the baseline length change of 1500 m relative to the short arm length. The arms are housed in a vacuum chamber, and reflectors are fixed directly to the ground. Therefore, this laser strainmeter can directly measure the baseline length expansion and contraction. Furthermore, we use corner cubes for the reflector to simplify alignment adjustment at the kilometer scale and use no active controls on the optics. This feature makes the stable operation. The GIF has been operating for about three years since it was installed in 2016.

GIF has better low-frequency sensitivity than a seismometer. Since the seismometer measures the apparent force on its proof mass, it is impossible in principle to distinguish between a tilt component of the ground and the horizontal component of the ground. Moreover, the seismometer also sensitive to the temperature changes in the low-frequency. On the other hand, laser strainmeter does not have such mechanical limitations of seismometers, and the strainmeter can directly measure the expansion and contraction of the baseline length. This chapter compares the sensitivity of GIF and seismometer. The results showed that the GIF had a lower noise level than the seismograph below 0.1 Hz.

In this chapter, instruments of GIF are described. The working principles of the interferometer are described in section 3.1. Optics of GIF is described in section 3.2. The realtime signal acquisition system to send the strain signal to KAGRA is described in 3.3.

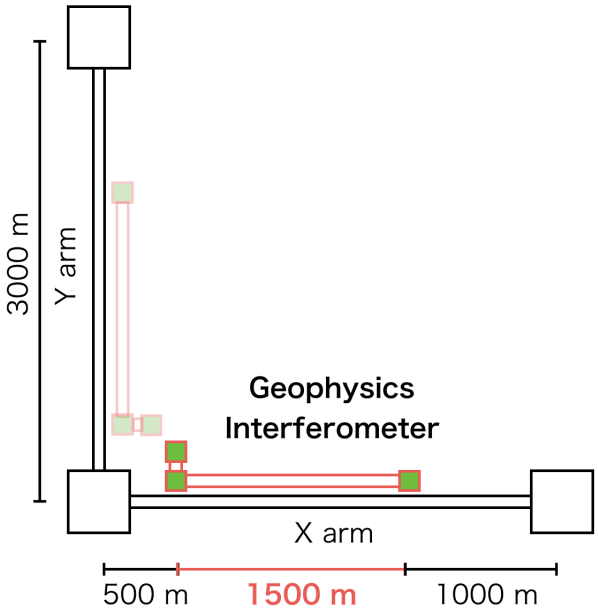

Figure 3.1: Location of geophysics interferometer (GIF). Whereas KAGRA is a symmetric L-shape 3000 m Michelson interferometer, GIF is an asymmetric 1500 m Michelson interferometer. GIF is only installed along the X-arm tunnel.

3.1 Working Principle

This section describes the measurement principle of GIF and the main noise limiting the strain measurement. GIF is an asymmetric Michelson interferometer with 0.5 m and 1500 m arms. GIF is the equipment that measures the baseline length elongation and contraction of 1500 m based on the short arm length. Therefore, we use the super invar plate whose thermal expansion coefficient is extremely low as the reference arm, and both arms are housed in vacuum tanks so as not to be changed by air fluctuation. The asymmetric arms cause noise coupling from the laser frequency noise. Thus, we have to decrease the noise for precise strain measurement.

This section also describes the difference in the seismic strain response between 1500 m and 3000 m baselines. While the GIF directly measured at 1500 m, it does not directly measure the 3000 m baseline of KAGRA. However, for example, when the base length is expanded or contracted in dc, the fluctuation of 3000 m is two times that of 1500 m. This relation is true below 1 Hz with some assumptions. Therefore, we can measure the baseline length fluctuation of KAGRA by GIF signal in this frequency band.

As described in section 1.2, the working principle of the strain measurement of GIF

is the same as the GW detectors. However, the sensitivity of GIF is limited by the laser frequency noise due to the asymmetric optical configuration.

3.1.1 Asymmetric Michelson Interferometer

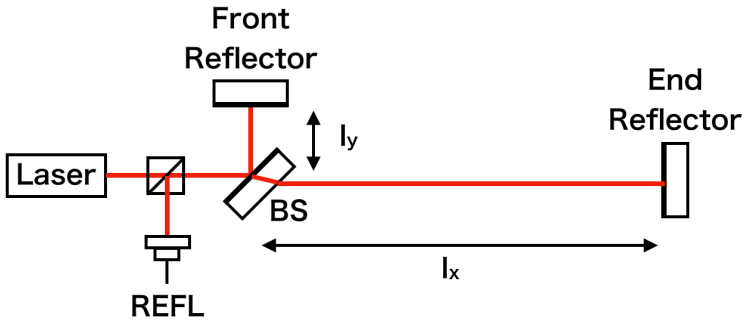

Figure 3.2: Schematic drawing of the GIF as an asymmetric Michelson interferometer, which has two different arm lengths, $l_x \gg l_y$. In this figure, the mode-matching optics and the optics for signal detection are not drawn.

An asymmetric Michelson interferometer is an interferometer that is sensitive to both strain changes in baseline length and fluctuations of the laser frequency. Here, consider the Michelson interferometer, as shown in Figure 3.2. For simplicity of discussion, it is assumed that the power fluctuation of the laser and the detection noise in the photodetector can be sufficiently ignored.

The asymmetric interferometer measures changes of baseline length l_x with reference to the short arm l_y and its fringe signal is obtained at the REFL port. The optical phase ϕ_- is given as

$$\phi_- = 4\pi \frac{l_-}{\lambda}, \tag{3.1}$$

where $l_- = l_x - l_y$ is the differential of the two arm length and λ is the wavelength of the laser. Taking the infinitesimal changes of both side in Eq. (3.1), one can obtain the

following equation;

$$\Delta\phi_- = \frac{4\pi}{\lambda}\Delta l_- - \frac{4\pi}{\lambda^2}\Delta\lambda l_- \tag{3.2}$$

$$= \frac{4\pi l_x}{\lambda}\left(\frac{\Delta l_-}{l_x} - \frac{\Delta\lambda}{\lambda}\frac{l_-}{l_x}\right) \tag{3.3}$$

$$= \frac{4\pi l_x}{\lambda}\left(\frac{\Delta l_-}{l_x} + \frac{\Delta f}{f}\frac{l_-}{l_x}\right), \tag{3.4}$$

where Δ denote the infinitesimal change of the variables and f is the laser frequency.

Consider the asymmetricity of the arms. Assuming that the X-arm length is sufficiently longer than the Y-arm to be regarded as $\Delta l_- = l_x$, Eq.(3.4) can be represented as

$$\Delta\phi_- = \frac{4\pi l_x}{\lambda}\left(h + \frac{\Delta f}{f}\right), \tag{3.5}$$

where $h \equiv \Delta l_x/l_x$ is the strain of the baseline.

Equation (3.4) shows that the optical phase of an asymmetric Michelson interferometer is represented by both the relative fluctuation $\Delta f/f$ and the strain of the baseline. Thus, for the interferometer to be sensitive to only the strain, the laser frequency fluctuation must be smaller than the amount of the strain.

3.1.2 Noise

The optical phase must be changed by the baseline length fluctuation. As mentioned above, GIF is an asymmetric Michelson interferometer, so it is sensitive to the laser frequency fluctuations as well as the strain of the baseline. Therefore, a frequency stabilized laser is required. In addition, the optical phase is changed by the fluctuation of the optical path due to a gas in the arms. Thus, the optical path of the interferometer is housed in a vacuum chamber.

Frequency Noise

As mentioned above, the noise of asymmetric interferometer is limited by the frequency noise because of a lesser amount of common-mode rejection. The GIF, therefore, uses the frequency stabilized laser by using the iodine-absorption line [60]. The fluctuation $\Delta f/f$, which corresponds to the strain, is

$$h = \frac{\Delta f}{f} \sim 7 \times 10^{-13}. \tag{3.6}$$

Residual Gas Noise

GIF interferometer is housed in the vacuum chamber to reduce the residual gas noise. Because residual gas fluctuates the optical path, length measured by interferometer is also fluctuates. The optical path length $L_{\rm opt}$ is given by $L_{\rm opt} = nL$, where L is the length of the baseline and n is the refraction index of the medium. Under the pressure of p in vacuum, the index n is approximated as $n = 1 + c_0(p/p_0)$, where c_0 denotes the relative refractive index, p_0 is pressure in standard air at 1 atm. The apparent strain due to the residual pressure is given as [61];

$$h = (L_{\rm opt} - L)/L = c_0(p/p_0) \sim 3 \times 10^{-9} p. \tag{3.7}$$

In order to maintain the strain sensitivity; 3×10^{-13}, the vacuum pressure should be below 1×10^{-4} [Pa]. However, actual vacuum pressure is 1×10^{-2} [Pa], then apparent strain is $\sim \times 10^{-12}$.

3.1.3 Seismic Strain Response

In order to use GIF as a baseline length monitor for KAGRA, we should consider the difference in its length. For example, a static baseline length expansion is excited to the baseline lengths of GIF and KAGRA. The strain obtained by dividing each baseline length changes by the baseline length is equal. This relationship is correct when the wavelength of the elastic wave is longer than the baseline length.

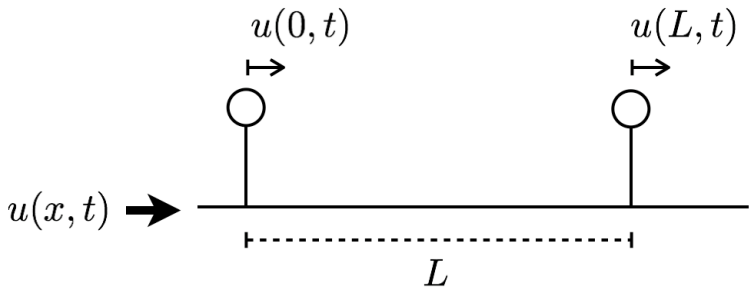

Figure 3.3: Seismic wave propagating two points

As shown in Figure 3.3, consider the response from strain to the optical phase H_{strain} in the case that the plane seismic waves whose displacement $u(t, x)$ is represented as $u(t, x) = u_0 e^{i(\omega t - kx)}$ with angular frequency of ω and the wavenumber of k. The seismic wave propagates along with the direction of the baseline (the right direction in this figure).

Relationship between the strain ϵ and the displacement of the seismic wave u is $\epsilon \equiv \frac{du}{dx}$. Relationship between the baseline length change ΔL and the optical phase of the interferometer ϕ_- is given by $\phi_- = \frac{4\pi}{\lambda}$, according to Eq.(3.1). We consider the transfer function from the displacement to the length fluctuation H_{disp}.

Response from u to ΔL, (H_{disp})

Before calculating the response to strain, we calculate the response from the displacement of the seismic wave to the baseline length change. First, because the length fluctuation between two mirrors separated with L can be expressed as

$$\Delta L(t) \equiv u(t, 0) - u(t, L) \tag{3.8}$$

$$= u(t, 0) - u(t - \tau, 0), \tag{3.9}$$

where $\tau = L/v$ is the time delay, the transfer function from the displacement to the length fluctuation is given by Laplace transform as

$$H_{\rm disp}(s) \equiv \frac{\Delta L(s)}{u(s)} = \frac{u(s)\left[1-\exp(-\tau s)\right]}{u(s)} = 1-\exp(-\tau s) \tag{3.10}$$

Response from ϵ to ϕ_-, ($H_{\rm strain}$)

Because the strain amplitude $\epsilon(x,t)$ is defined as $\epsilon(x,t) \equiv \frac{du}{dx}$, the seismic strain is represented as

$$\epsilon(x,t) \equiv \frac{du}{dx} = \frac{du}{dt}\frac{1}{v} = \frac{s}{v}u(s) \tag{3.11}$$

Therefore, the transfer function from the seismic strain to the displacement is given as

$$\frac{\Delta L(s)}{\epsilon(s)} = H_{\rm disp}\frac{v}{s} \tag{3.12}$$

Finally, because the transfer function from the length change of the baseline to the optical phase is given as $4\pi/\lambda$, the transfer function from the seismic strain to the optical phase is represented as

$$H_{\rm strain}(s) = 4\pi\frac{1}{\lambda}\left[1-\exp(-\tau s)\right]\frac{v}{s}. \tag{3.13}$$

Block diagram of the transfer function from the starin to the optical phase $H_{\rm strain}$ is shown in Figure (3.4).

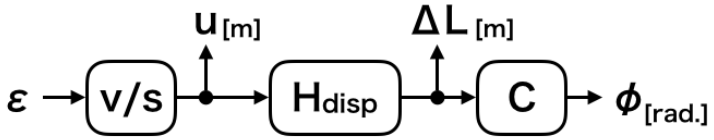

Figure 3.4: The response from seismic strain to optical phase.

Comparison with the baseline length

Here, we describe the length dependence of the response given by Eq.(3.13). The bode plot of the strain response with two different baseline lengths is shown in Figure 3.5. The response has a flat response below the corner frequency defined by

$$f_0 = \frac{v}{L}, \tag{3.14}$$

where v is the phase velocity and L is the length of the baseline. Thus, if the baseline length is twice, the frequency becomes a half value, which means a decrease of the observation frequency band. For example, in the case of $L = 1500\,\mathrm{m}$, and assuming the phase velocity of 5.5km/sec, the corner frequency is $f_0 \sim 3.7\,\mathrm{Hz}$. In the KAGRA case, the frequency is $f_0 \sim 1.8\,\mathrm{Hz}$. Therefore, below 1 Hz, the response of both baseline is flat response. In this region, the baseline length fluctuation of KAGRA $\Delta L_{\mathrm{KAGRA}}$ is given by

$$\Delta L_{\mathrm{KAGRA}} = 3000 \times \epsilon_{\mathrm{GIF}}, \tag{3.15}$$

where ϵ_{GIF} is the strain measured by GIF in 1500 m baseline.

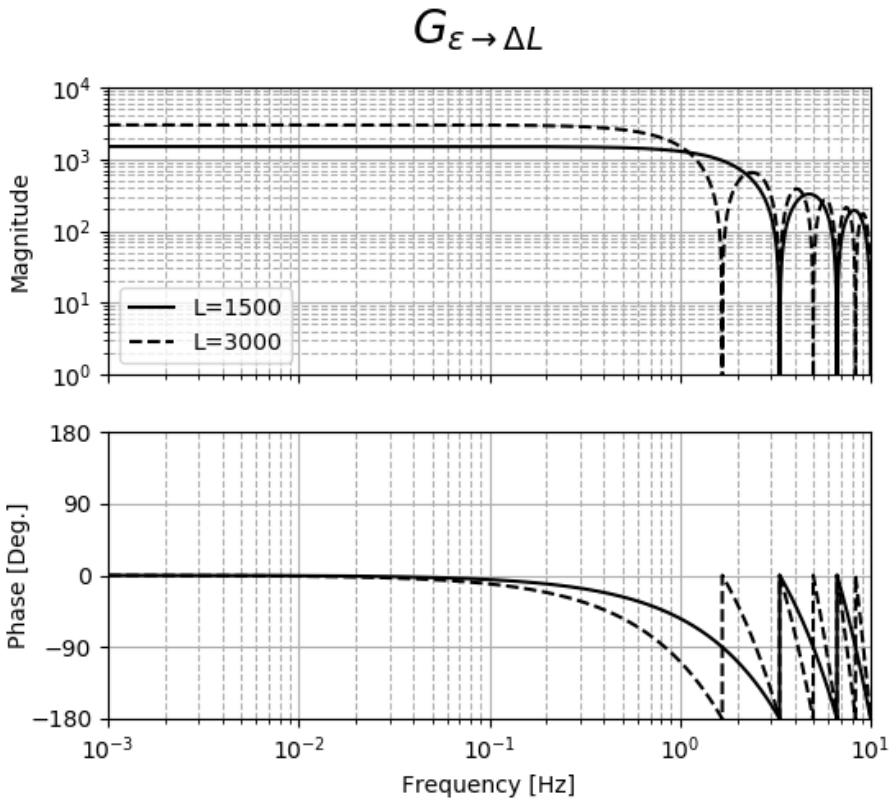

Figure 3.5: Compasison of the transfer function from strain of the baseline ϵ to the length change of that ΔL in the different baseline length given in Eq. (3.13) assumed the phase velocity of 5.5 km/s.

3.2 Optics

In the previous discussion, the laser light was implicitly assumed the plane wave, which does not change the optical phase and radius of the beam when it propagates, but the actual beam is not. The actual beam requires a design of these beam profiles to interfere with the beam within a finite scale. In this section, we assume a Gaussian beam and describe the design for the GIF interferometer.

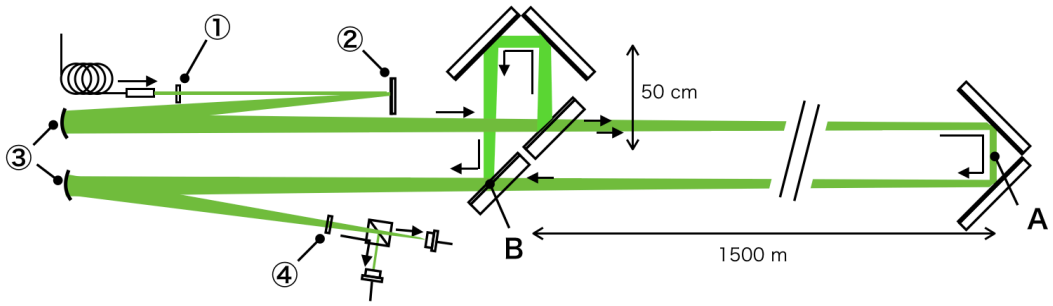

Figure 3.6: Schematic optics layout. (1) A collimator lens for input beam. (2) A flat mirror for steering mirror. (3) Two concave mirrors with a radius of curvature of 9.8 m for mode matching. (4) A collimator lens for output beam. The waist of the beam is at the end reflector at point A. Two reflected on the reflectors are combined at point B.

3.2.1 Input Output Optics

Input-output optics is used for matching the beam profile of the input laser with that of the interferometer in order to interfere, as shown in Figure 3.6. The output beam from the laser incidents into a beam splitter (BS) using (1) a collimator, (2) steering mirror, and (3) concave mirrors in order to be the beam waist at the end reflector. The reflected beams from each reflector are re-combine at Point B, and this interfered light is incidents to the photodetector through another concave mirror and collimator. The mode matching is described in reference [62].

3.2.2 Core Optics

The core optics of the Michelson interferometer are composed of two reflectors and a beam splitter (BS). The core optics are housed in a vacuum tank not to be affected

by environmental changes. These optics are fixed on the super-invar plate so that the length does not change in temperature. Furthermore, the reflector uses corner cubes. Thus we do not require alignment on the km scale. The vacuum tank containing these optical elements is placed on granite directly fixed to the ground.

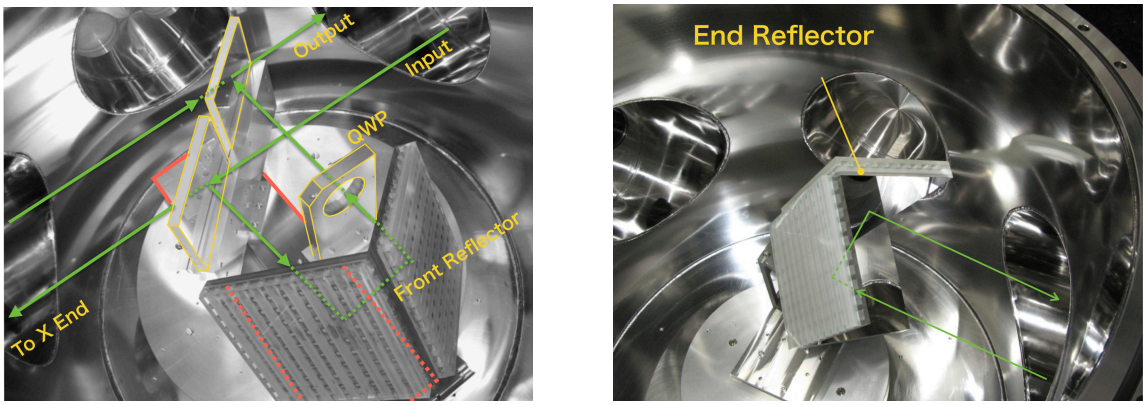

(a) Core optics in the front vacuum chamber. **(b)** Core optics in the end vacuum chamber.

Figure 3.7: The picture of the core optics.

In order to minimize the size of the reflectors, the beam of the GIF interferometer is designed so that the beam waist is in the end reflector, as shown in Figure 3.6. In this case, if the beam waist w_0 is focused at the end reflector, the beam radius at the front reflector $w(L)$, which locates 1500 meters from the end reflector, spreads. Therefore, we need to design the beam so that

$$\arg\min_{w_0} \left[w_0 \times \frac{w(L)}{w_0} \right]. \tag{3.16}$$

Substituting Eq.(B.4) into Eq.(3.16), one can obtain the beam waist radius

$$w_0 = \sqrt{\frac{L\lambda}{\pi}} \tag{3.17}$$

We note that the Rayleigh range is $z_0 = L$ in the case of that.

According to Eq.(3.17), the beam waist radius of the GIF is

$$w_0 = \sqrt{1500\,[\mathrm{m}] \times 532\,[\mathrm{nm}]/\pi} = 16\,\mathrm{mm}. \tag{3.18}$$

Furthermore, the beam radius at the front reflector is $w(1500) = \sqrt{2}w_0$. Finally, we determine the size od the reflectors as the three times of the $w(1500)$, then the minimum size of the reflector is $2 \times 3 \times \sqrt{2}w_0 \sim 270\,\mathrm{mm}$.

3.2.3 Frequency Stabilized Laser

As mentioned in 3.1.2, because the frequency noise of the laser limits the sensitivity of the strain measurement, the GIF interferometer uses the frequency stabilized laser utilizing the iodine absorption line [63]. The control diagram of the frequency stabilization system is shown in Figure 3.8. This control is a feedback system in order to reduce the error signal of the laser frequency and the frequency of the iodine absorption line. The error signal is obtained by the saturated absorption spectroscopy method from the absorption signal that is a doppler free signal by using the pump and probe light [64].

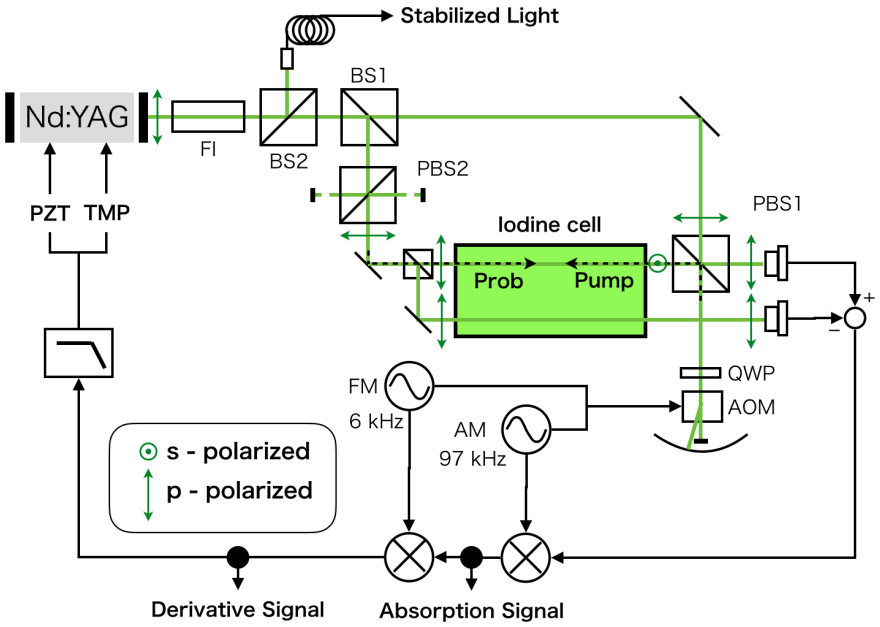

Figure 3.8: Schematic diagram of the frequency-stabilization system of the GIF main laser.

3.2.4 Quadrature Phase Fringe Detection

We use the quadrature-phase fringe detection to measure the length change of the baseline with a wide dynamic range [65]. The optical layout for the detection is shown in Figure 3.9. A half-wave plate (HWP) produces a p-polarization and s-polarization. A quarter-wave plate (QWP) delay the optical phase of the s-polarized light with 90 degrees against the other. As a result, one can obtain the quadrature-phase fringes.

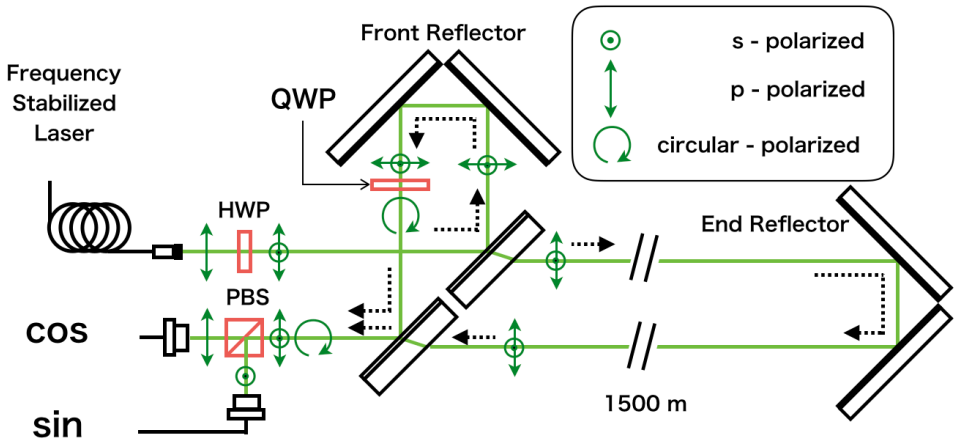

Figure 3.9: Quadrature interferometer used in the GIF strainmeter.

The quadrature-phase fringes are detected by two photodetectors, these can be represented as

$$x(t) = x_0 + b\cos(\phi(t)), \tag{3.19}$$

$$y(t) = y_0 + a\sin(\phi(t) + \delta), \tag{3.20}$$

where x and y are the two voltage outputs from the detectors, a and b are the amplitudes of these fringe signals, x_0 and y_0 are the offsets, ϕ is optical phase, and δ is the phase offsets from imperfections [66]. Here, the optical phase ϕ is given by

$$\phi = \arctan\frac{\bar{Y}}{\bar{x}} \tag{3.21}$$

where

$$\bar{Y} = \left(\frac{\bar{y} - \bar{x}\sin\delta}{\cos\delta}\right), \tag{3.22}$$

$$\bar{x} = \frac{x - x_0}{b} \text{ and } \bar{y} = \frac{y - y_0}{a}. \tag{3.23}$$

According to Eq.(3.19) and Eq.(3.20), if these parameters are given in at time t, the optical phase $\phi(t)$ is obtained.

3.3 Realtime Data Aquisition System

Essentially, the GIF is an independent instrument from the KAGRA not to interfere with each other. Therefore, the data acquisition system of each was developed independently. However, in order to use the GIF strainmeter for the baseline compensation system, we need to implement the GIF system into the KAGRA system.

In this section, the realtime data acquisition system is described. In the quadrature-phase detection method, we need the ellipse fitting to obtain the optical phase. In section 3.3.1, the realtime data acquisition system is described. This system process the fitting below 1 msec.

3.3.1 Realtime Data Processing

All the PD signals of the GIF are taken by the analog-digital-converter (ADC) and processed in the KAGRA digital system, which is the same as LIGO [59]. The ADC converts the analog signal to the digital signal with 16 bit and 2^{16} Hz sampling frequency. All the digital signals are simultaneously sampled in the digital system.

The realtime calculation model in the KAGRA system is shown in Figure 3.10. To reduce the calculation cost, the digital signal in this model is downsampled to 2^{14} Hz. This realtime model has three main functions; the ellipse fitting function, the strain calculator function, and the unwrap function. These functions are described below.

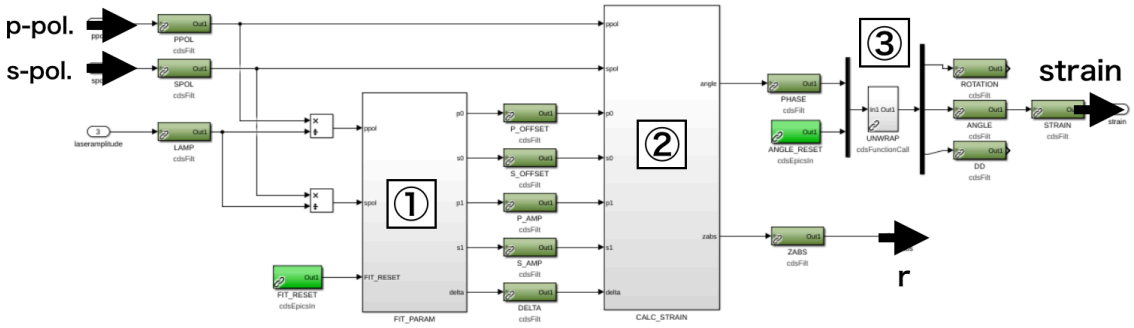

Figure 3.10: Realtime calculation model of the phase calculator of GIF. (1) the elipse fitting function (2) the strain calclator function (3) the unwrap function.

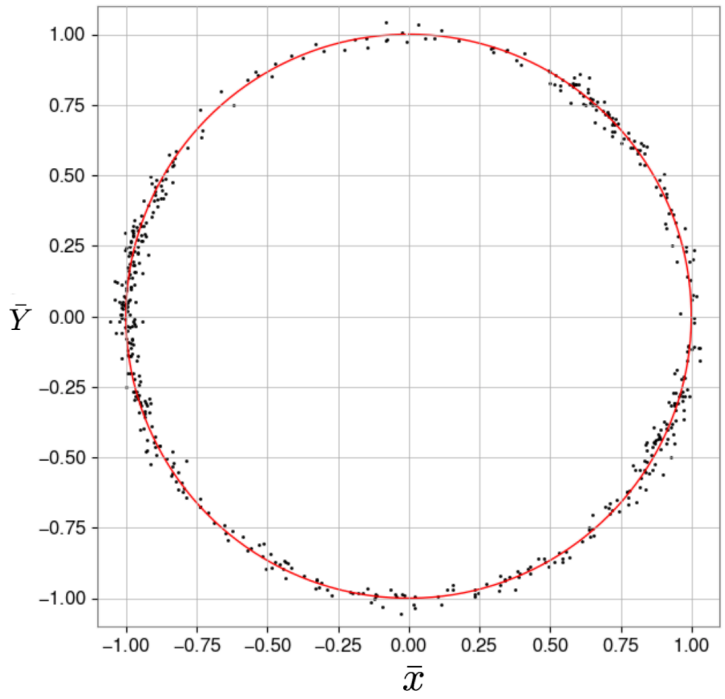

Figure 3.11: Fitting the elipse curve to the Lissajous figure. $\bar{Y}$ and $\bar{x}$ are defined in Eq.(3.22,3.23), respectively.

Elipse fitting function

This function is for obtaining the five ellipse parameters in Eq.(3.20) and Eq.(3.19) by fitting the ellipse curve to the Lissajous figure drawn by two PD signals. The function calculates these parameters using the least-square method with 512 data points of each two PD signals, as shown in Figure 3.11.

Strain calculator function

This function calculates the optical phase using the ellipse parameters based on Eq.(3.21). For example, Figure 3.11 shows the fitted curve (red line) and the data points (black dots). As described above, the optical phase ϕ is an angle of the data point. This optical phase depends on the power ratio $\bar{y}/\bar{x}$ and the phase offset δ because the phase is given by

$$\phi = \frac{\bar{y}}{x}\frac{1}{\cos\delta} - \tan\delta. \tag{3.24}$$

This means that the changes in the power ratio and the phase offset are the noise of the optical phase measurement. In particular, the power ratio is sensitive at the PBS, which divides the interfered two polarized lights. For this reason, we covered this location with a small house to protect winds disturbed by passengers. On the other hand, the phase offset has small fluctuation because the QWP is installed in the vacuum chamber.

Although the calculation of the optical phase by measuring the angle is not affected by the input power changes, the signal to noise ratio will worse in less input power. We also monitor the quality of the calculation using a parameter;

$$r = \sqrt{\bar{x}^2 + \bar{Y}^2}. \tag{3.25}$$

Unwrap function

This function unwraps the optical phase calculated by the phase calculator function and returns the continuous phase proportional to strain because the atan2 function is used in the phase calculator return between $-\pi$ to π.

3.3.2 Comparison with seismometers

We measure the 3 km baseline length change by using the seismometers and GIF, and compare their sensitivity. The two seismometers are installed on the corner area and X-end area, which is separated 3 km. The displacement is calculated by the differential signal of the X direction of these seismometers. On the other hand, because the GIF strainmeter directly measures the displacement of the 1.5 km baseline. Thus, the displacement of the 3 km is calculated by this strainmeter signal multiplied factor 2.

Figure 3.12 shows the ASDs of the displacement of the baseline measured by two seismometers and GIF strainmeter. Above 0.1 Hz, seismometer could measure the displacement, but below this frequency, this is limited by self-noise, which increases in low-frequency. On the other hand, a strainmeter could measure the displacement below 1 Hz. For this reason, we use GIF strainmeter to measure the deformation of the baseline in the low-frequency region, which are the main disturbances degrading the duty cycle of GW detectors.

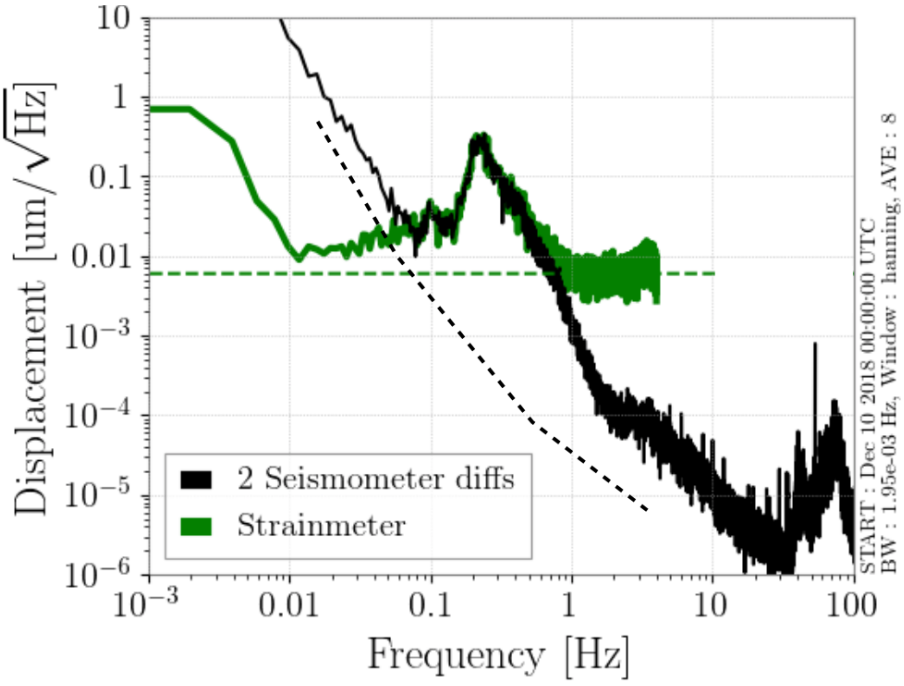

Figure 3.12: Baseline length fluctuation measured by two seismometers (black) and GIF strainmeter (green).

Chapter 4

Baseline Compensation System

Baseline Compensation System is an active seismic isolation system to attenuate the low-frequency seismic motions below 1 Hz. In this region, the wavelength of the seismic motions is more than a few kilometers. Such global disturbances cannot be avoided even in the underground. Therefore, the gravitational wave detectors require a vibration isolation system to reduce the influence of these disturbances.

The active seismic isolation system is for attenuating the low-frequency seismic motions in which the passive seismic isolation cannot attenuate. The passive seismic isolation using a pendulum, as described in chapter 1, cannot attenuate the motion below its eigenfrequency. This means that the suspension point of the pendulum moves with the ground below the eigenfrequency which is typically 1 Hz. On the other hand, active seismic isolation reduces the low-frequency motions by using a feedback control with sensors which can measure the disturbance of the suspension point.

Active seismic isolation can be categorized into two types based on the difference in sensors used for control. One is active inertial seismic isolation which uses inertial sensors, e.g., seismometers. The sensors measure the motion of the suspension points against the inertial frame. Thus, the suspension points are isolated from the ground by using a feedback control with the sensor. Although this method is used in the present gravitational wave detectors the inertial sensor has problems in lower frequency (typically below 0.1 Hz); insufficient sensitivity at lower frequencies and signal coupling from the tilt motion to the horizontal motion of the ground. These problems cause the low-frequency seismic isolation performance to deteriorate.

The second is active baseline seismic isolation, which has been developed to solve the problem of the low-frequency sensitivity of the inertial sensor. This method is based on

the point that the vibration which is a problem for the gravitational wave detectors is the fluctuation of the optical cavity length. Thus, the length motion should be isolated from the seismic motion.

This method use a sensor called a suspension point interferometer (SPI) which can directly measure the length motion between suspension points of pendulums suspending two mirrors constituting optical cavity mirrors. The direct length measurement makes it possible to isolate the cavity length from the seismic motion down to dc. However, it is not used in actual gravitational wave detectors because of the cost of constructing a km-scale SPI and the various controls required to operate it.

In order to resolve the problems of these two active seismic isolation, we have developed the baseline compensation system which is a new active baseline seismic isolation system using the GIF as the SPI. While the conventional system uses a feedback control, the new system uses a feedforward control. Owing to the feedforward control, it does not necessarily have to install the SPI on the suspension points directly if the SPI could measure the length of between the points. Moreover, because the purpose of the active isolation system is the attenuation of the low-frequency motions below 1 Hz, all we need to do is to use a SPI which can measure the baseline length changes in this region. GIF is exactly a SPI for the purpose. As described in chapter 3, the GIF has a better sensitivity than the inertial sensors in lower frequency region, and have been operating stably even a kilometer-scale interferometer. Taking the advantages of these special characteristics of GIF, we have developed the new system in KAGRA.

In this chapter, reviews of the two active seismic isolation system and baseline compensation system implemented in KAGRA are described.

4.1 Active Inertial Seismic Isolation

An active inertial seismic isolation system is widely used in the current GW detectors. The system uses the platform stage which isolates the suspension point of the pendulum from seismic motion. In the LIGO case, this stage is supported by the hydraulic external pre-isolator (HEPI) [67], and in KAGRA and Virgo case, the stage is suspended by an inverted pendulum (IP) [68, 69]. These stages are controlled by feedback control with the inertial sensor on the stage.

In this section, we describe control schemes for the active inertial seismic isolation system, especially in the LIGO case [70]. In the control schemes, the system uses three

control techniques: one feedback control and two auxiliary feedforward control for compensation for insufficient performances of the inertial sensor on the stage. In KAGRA and Virgo, the two feedforward controls are not currently used. As a general case of the active inertial seismic isolation system, these three controls are described below.

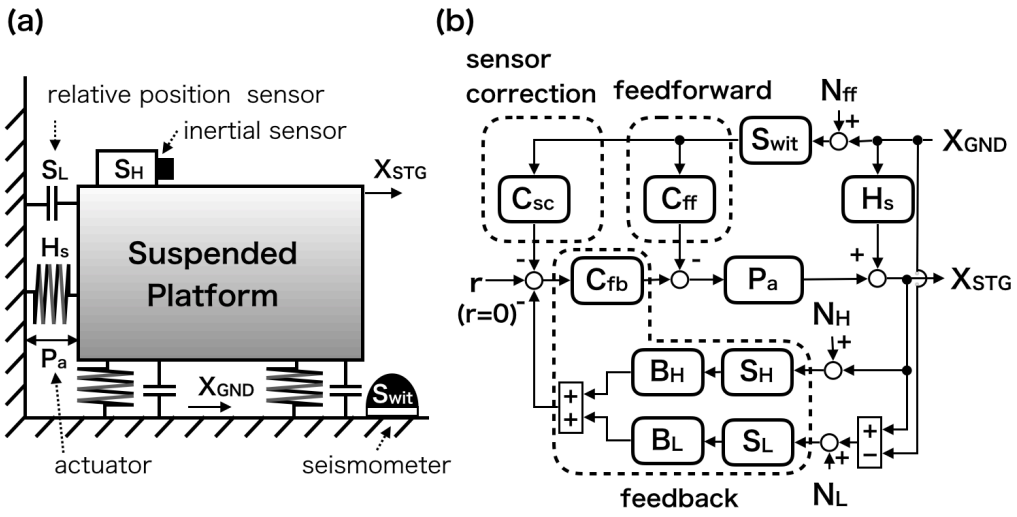

Figure 4.1: **(a)** Schematic drawing of an active seismic isolation system for the platform. **(b)** Block diagram of the active control scheme.

The active isolation system is shown in Figure 4.1(a). A platform is suspended from the ground with transmissivity H_s. This platform is fed back both signal of an inertial sensor with calibration factor S_H and signal of a relative position sensor with calibration factor S_L, to the platform using actuator with actuator efficiency P_a. This feedback control actively decouples the platform from the seismic disturbance from 0.1 Hz to a few Hz. Furthermore, the platform is controlled with feedforward using a seismometer with a calibration factor of S_{wit} installed on the local ground. The block diagram of the system is shown in Figure 4.1(b), the active vibration system is integrated with feedback control, sensor correction control, and feedforward control. These control schemes are described below.

4.1.1 Sensor Blending Technique

The purpose of the active inertial seismic isolation is to reduce the stage motion against the inertial frame. Thus, we use feedback control using an inertial sensor. However, the

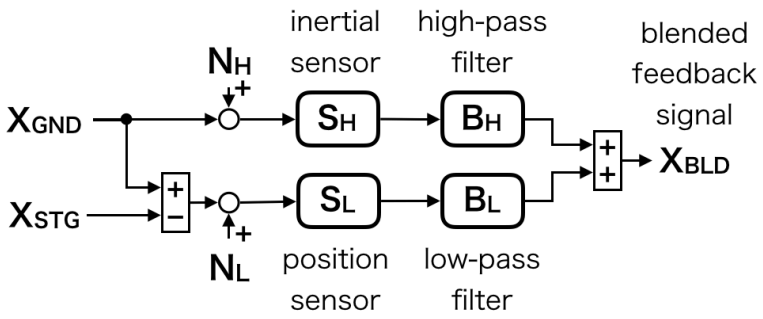

Figure 4.2: Sensor Blending.

feedback system cannot use the inertial sensor in this region because the noise level of the inertial sensor is worse in the low-frequency region. Nevertheless, the stage needs control of the DC position. In this situation, the sensor blending technique is commonly used in the active vibration system.

As shown in Figure 4.2, the feedback signal is blended with signals of the inertial and position sensors. The inertial sensor output is filtered with high-pass filter B_{H} because the noise of the sensor is worse in the low-frequency region. On the other hand, the position sensor is filtered with a filter B_{L} so that

$$B_{\mathrm{H}}S_{\mathrm{H}} + B_{\mathrm{L}}S_{\mathrm{L}} = 1. \tag{4.1}$$

In the case of using the blended feedback signal, the displacement of the platform stage is given by

$$X_{\mathrm{STG}} = \frac{G}{1+G}LX_{\mathrm{GND}} + \frac{1}{1+G}H_{\mathrm{s}}X_{\mathrm{GND}} + \frac{G}{1+G}\left(HN_H + LN_L\right), \tag{4.2}$$

where X_{STG}, X_{GND}, N_{H}, and N_{H} are the displacement of the stage and the ground motions, and the noise of the inertial sensor and the position sensor, respectively. $G = C_{\mathrm{fb}}P_{\mathrm{a}}$ is the loop gain, and the multiples of the complementary filters (B_{H}, B_{L}) and each sensor responses are defined as $L = B_{\mathrm{H}}S_{\mathrm{H}}$ and $H = B_{\mathrm{L}}S_{\mathrm{L}}$, respectively. Here, if the feedback is work enough; the loop gain is large enough, the displacement of the stage is given as

$$\lim_{G\to\infty} X_{\mathrm{STG}} = LX_{\mathrm{GND}} + \left(HN_H + LN_L\right) \tag{4.3}$$

According to Eq.(4.3), to attenuate the stage to the inertial frame, the active isolation system should design L as small as possible, whereas the H as the complementary filter

of that must be large, which means that the inertial sensor noise introduces to the stage. Actually, the cutoff frequency of these filters is chosen at 100 mHz due to the inertial sensor noise, and the system cannot isolate the seismic noise below this frequency. In other words, although the active vibration system using the inertial sensor can design the response from the ground to the stage by filter L, the system performance is limited by the inertial sensor noise in the low-frequency region.

4.1.2 Sensor Correction Technique

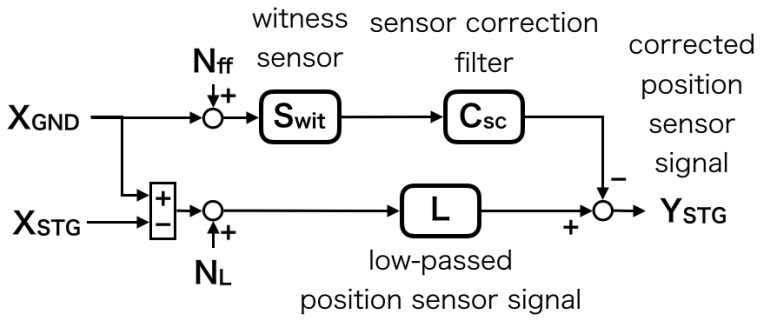

Figure 4.3: Sensor correction scheme.

The sensor correction technique is a method to correct the position sensor by using the additional inertial sensor on the ground [71]. Because of the insufficient noise of the inertial sensor on the stage, the blended feedback signal had to use the position sensor in the low-frequency. This means that the stage motion is attenuated against the local ground frame, not the inertial frame in this frequency region.

The sensor correction removes the ground motion from the position sensor by using another seismometer on the ground that has better sensitivity than the inertial sensor on the stage, as shown in Figure 4.3. We can correct the position sensor signal to be a signal of the new seismometer by subtracting the ground motion X_{GND} from the relative ground motion $X_{\mathrm{GND}} - X_{\mathrm{STG}}$. The corrected feedback signal can compensate for the performance of the inertial sensor on the stage.

Consider the displacement of the isolated stage utilizing the sensor correction technique. As shown in Figure4.1, the correction signal from the seismometer signal is injected at the set-point through the control filter C_{sc} to remove the ground motion from the feedback signal by using the position sensor. The displacement of the stage is

given by

$$\begin{aligned} X_{\mathrm{STG}} &= \frac{G}{1+G} L \left(1 - C_{\mathrm{sc}} \frac{S_{\mathrm{wit}}}{L}\right) X_{\mathrm{GND}} + \frac{1}{1+G} H_{\mathrm{s}} X_{\mathrm{GND}} \\ &+ \frac{G}{1+G} \left(H N_H + L N_L\right) + \frac{G}{1+G} C_{\mathrm{sc}} S_{\mathrm{wit}} N_{\mathrm{ff}} \end{aligned} \tag{4.4}$$

Here, in the case that the loop gain is large enough, the stage motion is given by

$$\lim_{G \to \infty} X_{\mathrm{STG}} = L \Delta_{\mathrm{sc}} X_{\mathrm{GND}} + \left(H N_H + L N_L\right) + L N_{\mathrm{ff}}, \tag{4.5}$$

where

$$\Delta_{\mathrm{sc}} \equiv \left(1 - C_{\mathrm{sc}} \frac{S_{\mathrm{wit}}}{L}\right) \tag{4.6}$$

is the gain matching coeffient. By comparison with Eq.(4.5) and Eq.(4.3), the displacement of the stage can be reduced by the gain matching due to the sensor correction. Although this gain match factor can be zero when $C_{\mathrm{sc}} = B_{\mathrm{L}}(S_{\mathrm{wit}}/S_{\mathrm{L}})$, actually, the factor is limited by the calibration errors of the witness sensor and the inertial sensor on the stage.

4.1.3 Feedforward Technique

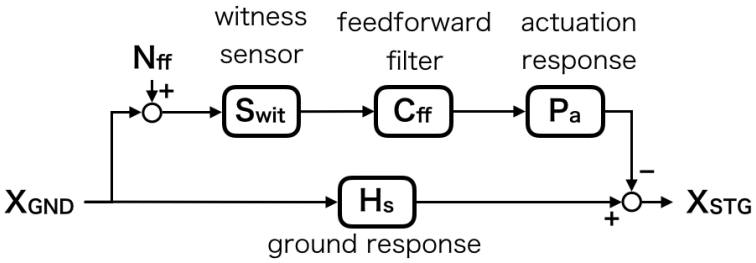

Figure 4.4: Feedforward scheme.

The feedforward technique is similar to sensor correction, but this technique removes the motion caused by the ground motion directly. Figure4.4 shows the block diagram of the feedforward control. While the stage motion X_{STG} is disturbed by the ground motion X_{GND} through the mechanical response of the platform H_{s}, the feedforward compensates for the stage motion by subtracting the disturbance with the witness sensor (in this case, seismometer) signal. This feedforward control does not depend on the feedback

control, unlike the sensor correction. In other words, the feedforward control works in the frequency region where the feedback loop gain is small, whereas the sensor correction works in the high loop gain region. Therefore, both feedforward and sensor correction technique is used to improve the active seismic isolation system in all frequency region.

Finally, consider the control integrated with three techniques; sensor blending, sensor correction, and feedforward. In the case that the additional feedforward signal is injected at the error-point, as shown in Figure 4.1, the displacement of the stage motion is given by

$$\begin{aligned} X_{\mathrm{STG}} &= \frac{G}{1+G} L \Delta_{\mathrm{sc}} X_{\mathrm{GND}} + \frac{1}{1+G} \Delta_{\mathrm{ff}} X_{\mathrm{GND}} \\ &+ \frac{G}{1+G} \left(H N_H + L N_L \right) + \frac{G}{1+G} C_{\mathrm{sc}} S_{\mathrm{wit}} N_{\mathrm{ff}} \\ &+ \frac{1}{1+G} P_{\mathrm{a}} C_{\mathrm{ff}} S_{\mathrm{wit}} N_{\mathrm{ff}}. \end{aligned} \tag{4.7}$$

Here,

$$\Delta_{\mathrm{ff}} \equiv \left(H_{\mathrm{s}} - P_{\mathrm{a}} C_{\mathrm{ff}} S_{\mathrm{wit}} \right) \tag{4.8}$$

is defined as the gain matching coefficient of the feedforward. One can find that, in Eq.(4.7), the first and second terms indicating the contribution from the ground motion can be reduced by the gain matching factors: Δ_{sc} and Δ_{ff}.

4.1.4 Problem in Lower Frequency Region

The inertial sensors have a problem in horizontal measurement in low-frequency due to coupling from the tilting. This is called the tilt-horizontal coupling. Because of this coupling, the feedback control using the inertial sensor is difficult to suppress the horizontal seismic motion aggressively.

Tilt-horizontal coupling

The inertial sensors cannot distinguish the horizontal or tilt motions of the ground because the inertial sensor measure the apparent force from the sensor frame. This coupling is known as the tilt-holizontal coupling and the response from each ground motion is given by [72]

$$Y(s) = \frac{-ms^2}{ms^2 + cs + k} \left[W(s) + \frac{g \sin(\theta_0)}{s^2} \Theta(s) \right], \tag{4.9}$$

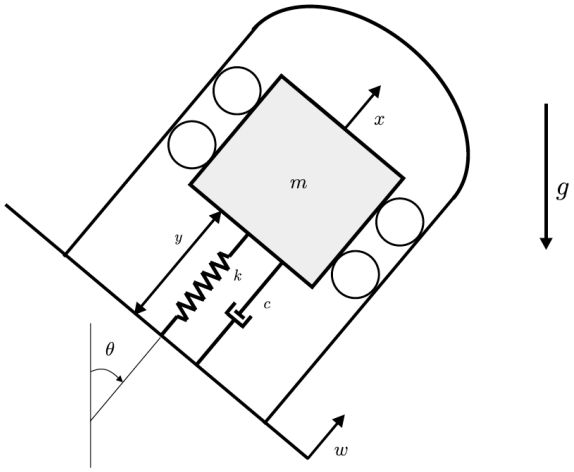

Figure 4.5: Tilted inertial sensor. Cited from Figure12 in [72]

where $W(s)$, $Y(s)$, and $\Theta(s)$ are, Laplace transformed, the displacement of the mechanical oscillator in the sensor, the relative displacement of the oscillator and the box housing it, and the tilting angle of the box, respectively. Moreover, m, c, k, g,, and θ_0 are the mass of the osclillator's proof mass, viscous damping coefficient, spring constant, and gravitational acceleration. According to Eq.(4.9), when

$$f < \sqrt{\frac{g\sin(\theta_0)}{(2\pi)^2}} \text{ [Hz]} \tag{4.10}$$

the tilt motion tends to couple to the horizontal motion. For example, in the case of the maximum tilt coupling: $\theta_0 = \pi/2$, the tilt motion contaminates the horizontal motion when $f < 0.5$ [Hz].

Control strategy to avoid the problem

Because of the tilt-horizontal coupling, the active inertial seismic isolation system, especially in LIGO, uses the tilt sensor to remove the tilt components in the inertial sensor for avoiding the signal coupling [73].

4.2 Active Baseline Seismic Isolation

For laser interferometric gravitational-wave detector, the baseline length should be isolated from the seismic noise, while it is not necessary to isolate the individual stages to the inertial frame. For this reason, the active baseline seismic isolation system using an additional interferometer named suspension point interferometer (SPI) has been developed.

4.2.1 Suspension Point Interferometer (SPI)

The basic idea of the active baseline seismic isolation is proposed by Drever in 30 years ago. In this idea, the baseline length is kept by feedback or feedforward with the baseline length signal measured by the suspension point interferometer (SPI), which is installed near the suspension point of the pendulum to measure the length [74]. The advantage of this active seismic isolation system is the sensitivity of the SPI, which is better than that of the inertial sensor in low-frequency. Thus, this system could attenuate the seismic noise to the dc region. Therefore, various types of vibration isolation systems have been developed so far.

Fabry-Perot Optical Cavity Type

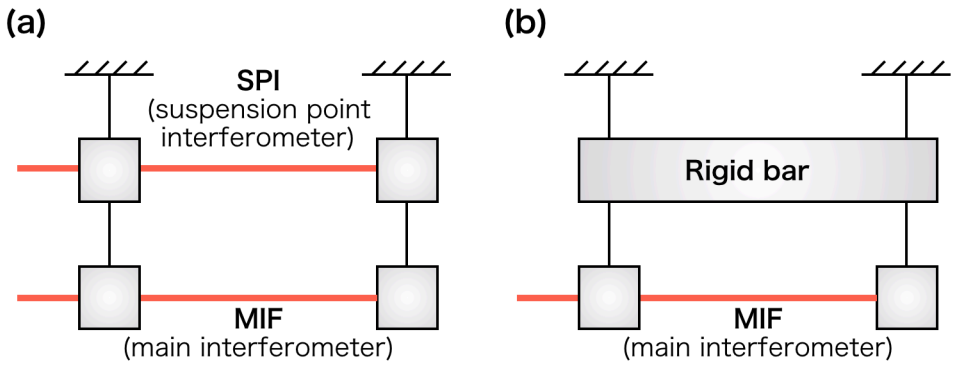

Figure 4.6: Schematic arrangement for one arm of SPI.

The initial type of the SPI is, as shown in Figure 4.6, the Fabry-Perot optical cavity on the main interferometer's arm cavity [75]. The advantage of this idea is that this system can suppress the baseline length fluctuation using the feedback control because

the SPI is installed near the main interferometer. Thus, if we increase the feedback gain, the length of the SPI behaves as the rigid bar, as shown in Figure 4.6(b). This means that the main cavity is suspended by the single pendulum from the ground, which does not change the baseline length entirely. After the proposal of the concept, a 2 m prototype of SPI was developed and demonstrated about 40 dB of vibration attenuation below 1 Hz [76].

The Fabry-Perot type SPI has problems in the km-scale GW detectors. While the displacement measurement of the Fabry-Perot cavity is precise, the linear range of the optical cavity is narrow (a few nm). Due to a small dynamic range, the operation of the SPI becomes unstable. The alignment control is also difficult in the km-scale detectors.

Michelson Interferometer Type

In order to resolve the narrow linear range of the Fabry-Perot type SPI, a prototype of the Michelson type SPI was developed [77]. The interferometer configuration of this prototype was the same as the GIF interferometer, and the signal detection also the same. Thus, the type had a wide dynamic range without alignment control to keep the operation of the SPI. This prototype demonstrates the vibration suppression in 2 m baseline over several hours.

4.2.2 Limitation due to CMRR

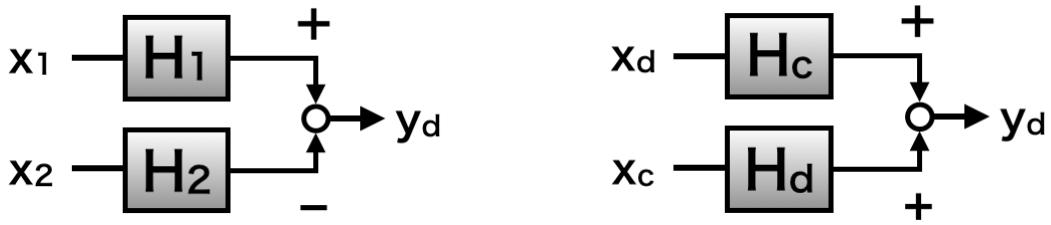

(a) two ground motion inputs (x_1 and x_2) one differential baseline change output (y_d)

(b) two differential and common ground motion inputs (x_d and x_c) one differential baseline change output (y_d)

Figure 4.7: comparison of two representations.

In general, the disadvantage of SPI is the noise coupling from the common motion due to the worse common-mode rejection (CMR) above the eigenfrequency of the pendulums,

because the active baseline vibration isolation system cannot attenuate the common motion of the baseline. If the mechanical response of the pendulums suspended from the SPI stage has asymmetricity, the CMR is worse, and the common motion couples to the baseline length change, which is the differential motion of the baseline.

Consider the differential motion of the platform stages. As shown in Figure 4.7a, the motion can be represented as

$$y_{\mathrm{d}} = H_1 x_1 - H_2 x_2, \tag{4.11}$$

where x_i, y_d and H_i denote the ground motion, the stage motion, and the mechhanical transferfunction from the ground motion to the stage motion, respectively. The indicies of i run in 1 or 2, which denote the name of the stages. Here, we define the differential and common motion of the ground and transferfunction as

$$x_{\mathrm{d}} = x_1 - x_2, \;\; x_{\mathrm{c}} = x_1 + x_2 \tag{4.12}$$

$$H_{\mathrm{d}} = \frac{H_1 - H_2}{2}, \;\; H_{\mathrm{c}} = \frac{H_1 + H_2}{2}. \tag{4.13}$$

The Eq(4.11) can be represented as

$$y_{\mathrm{d}} = H_1 x_1 - H_2 x_2 \tag{4.14}$$

$$= H_{\mathrm{c}} x_{\mathrm{d}} + H_{\mathrm{d}} x_{\mathrm{c}}. \tag{4.15}$$

The last equation can be represented as shown in Figure 4.7b. If we define the CMRR of this system as

$$H_{\mathrm{CMRR}} \equiv \frac{H_1 + H_2}{H_1 - H_2} = \frac{H_{\mathrm{c}}}{H_{\mathrm{d}}}, \tag{4.16}$$

the differential system can be written as

$$y_{\mathrm{d}} = H_{\mathrm{c}} \left(x_{\mathrm{d}} + \frac{1}{H_{\mathrm{CMRR}}} x_{\mathrm{c}} \right) \tag{4.17}$$

Eq.(4.17) indicates that increaseing the CMRR, the coupling from the common ground motion to the differential stage motion. In other words, the inverse of the CMRR is the coupling coefficient.

According to the definition of the CMRR in Eq.(4.16), this ratio is sensitive to the differential of two mechanical responses. Thus, if the eigenfrequency of each pendulum is not the same, the CMRR is decreased above the frequency due to an asymmetricity.

For example, assuming that the mechanical response of the stage is the single pendulum of H. In the high frequency, above the eigenfrequency, the response can be approximate as $H \sim (f_0/f)^2$. In this frequency region, if the eigenfrequency shifts by Δf_0, the gain of the response differs by $2f_0\Delta f_0$. This amount decreases the CMRR, and increase the common motion coupling to the differential motion.

4.2.3 RMS Reduction

The reduction of Root-mean-square (RMS) of the differential stage motion is expected by utilizing the SPI on the active baseline seismic isolation system. Because the SPI has good sensitivity in low-frequency, including the microseisms and earth tides, the RMS of the differential stage motion can be reduced.

The reduction has some advantages for GW detectors.

Improvement of Actuator Noise

The RMS reduction of the differential stage motion can relax the requirement of the actuator on the test mass. The actuator on the test mass can only actuate weak force because the strong actuator would introduce the actuation noise to the sensitivity [78]. Therefore, the RMS reduction on the top stage can relax the load on the test mass actuators. This means the improvement of the test mass actuator's noise directly, and means that the actuator's dynamic range can become wider.

Improvement of Glitch Noise

The reduction of the test mass actuator's load reduces the glitch noise, such as the Barkhausen noise. This noise is caused by the large DC voltage on the test mass actuators and actuators above the test mass stage [79].

4.3 Baseline Compensation System

The baseline compensation system is the active baseline seismic isolation system using the GIF. (まとめる)

4.3.1 Concept

The purpose of the new system is the attenuation of the low-frequency seismic noise below 1 Hz which degrades the stability of operation of the GW detectors. In this region, the RMS motion in cavity length is mainly disturbed by the seismic noise such as the microseisms ($\sim$ 200 mHz), large earthquake in distant place ($<$ 100 mHz), air pressure response ($<$ 20 mHz), and earth tides ($\sim$ 10^{-5} Hz). Moreover, the RMS of these seismic motion is comparable with several 1 $\sim$ 100 um, which is much greater than the test mass actuator's range. Therefore, the compensation of the cavity length disturbed by these seismic noises not only reduces the glitch noises in the GW signal but also improves the stability of the detector operation.

The concept of the baseline compensation system is the feedforward control, which moves the platform stage at X-end using the strain signal measured by the GIF in order to compensate for the seismic disturbance on the X-arm cavity, as shown in Figure 4.8. The cavity's mirrors are suspended by the pendulums, whose suspension point is fixed on the platform stage. This platform stage is also suspended by the inverted pendulums on the second floor. The strain signal is fed forward to the actuator on the X-end stage.

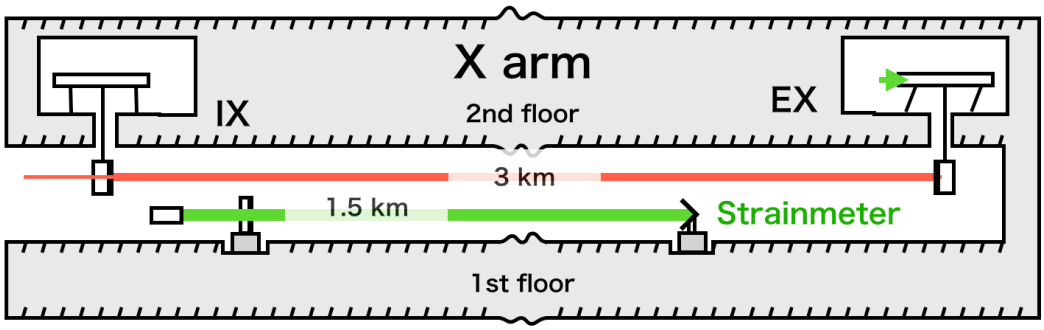

Figure 4.8: Schematic view of the baseline compensation system.

The idea of this baseline compensation system originates from the Michelson Interferometer type SPI as described in section 4.2.1. While this system used feedback control, our system uses feedforward control. The feedback control style has some difficulty in terms of the development of the km-scale SPI because we need to install the SPI on the platform stage. This means that, in the KAGRA case, an additional tunnel is needed on the second floor to connect the platform stages. On the other hand, the feedforward style system does not need such a facility; it just requires the SPI which can measure the baseline length in the target frequency below 1 Hz. GIF is exactly a SPI for the

purpose. The GIF has a better sensitivity than the inertial sensors in lower frequency region, and have been operating stably even a kilometer-scale interferometer.

4.3.2 Control Design

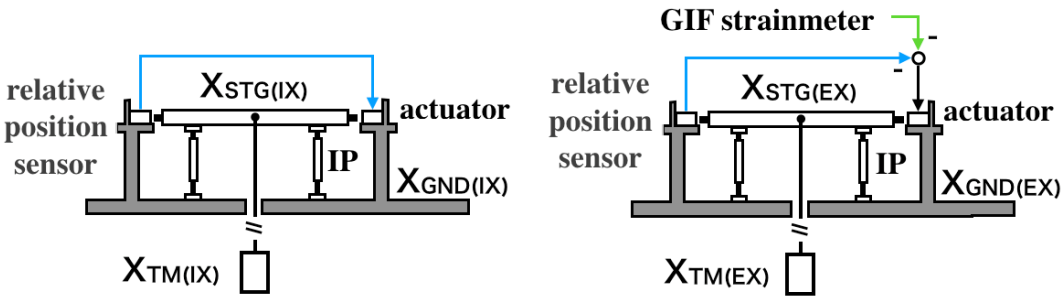

(a) Schematic contol of each platform stage. Left figure is that of the IX stage, right figure is that of the EX.

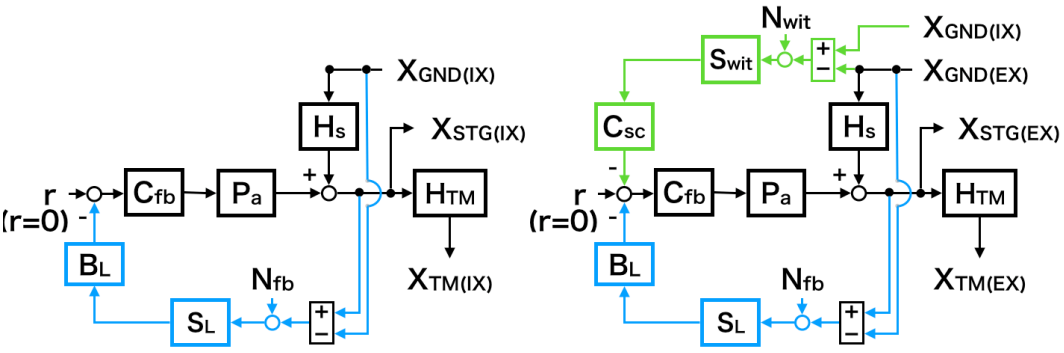

(b) Control block diagram of each platform stage. Left figure is that of the IX stage, right figure is that of the EX.

Figure 4.9: The baseline compensation control of each platform stage for demonstration.

To demonstrate the baseline compensation system using GIF as a SPI, we design a simple control configuration. Although the simplest configuration is the feedforward using the GIF, the feedforward control cannot suppress the disturbances: not only the horizontal seismic noise but also the ground tilt motion or the temperature fluctuation [80]. Because these disturbances could move the platform stage in a horizontal direction, we need a feedback control using the position sensor to suppress these disturbances. Therefore we use the sensor correction control rather than the feedforward control.

Figure 4.9a shows the schematic control of the platform stage for the input x-arm test mass (IX) and end x-arm test mass (EX). While the IX stage is fed back the relative position sensor signal to the actuator on the stage, the EX stage is added to the GIF strainmeter signal. In other words, while the IX stage is locked to the local IX ground, the EX stage is also locked to the local EX ground, but this feedback signal is corrected by using the GIF signal. The GIF measure the baseline length changes, which means the differential motion of the IX and EX ground. Therefore, the corrected feedback signal is the same as the feedback signal of the IX stage. In other words, the EX stage can follow the IX stage by using the corrected feedback signal.

Figure 4.9b shows the control diagram of each stage. In both stages, the displacement of the IX platform stage X_{STG} is disturbed by the local seismic motion X_{GND} though the mechanical response of the inverted pendulum (IP) H_{s}. In order to reduce the stage motion in the low-frequency region, below 1 Hz, the platform stage is controlled by the feedback control using the relative position sensor. S_{L}, N_{fb} and B_{L} are the displacement response and the noise of the relative position sensor and the low-pass filter of the complemental filter. The feedback signal is sent to the actuator, whose transfer function from the actuator force to the platform stage is given by P_{a}, through the control filter C_{fb}.

In this situation, each displacement of the stage are given by

$$X_{\mathrm{STG(IX)}} = \frac{G}{1+G}LX_{\mathrm{GND(IX)}} + \frac{G}{1+G}N_L + \frac{1}{1+G}H_{\mathrm{s}}X_{\mathrm{GND(IX)}}, \tag{4.18}$$

$$\begin{aligned} X_{\mathrm{STG(EX)}} &= \frac{G}{1+G}L\left(1-\frac{C_{\mathrm{sc}}S_{\mathrm{wit}}}{L}\right)X_{\mathrm{GND(EX)}} + \frac{G}{1+G}N_L \\ &+ \frac{G}{1+G}\frac{C_{\mathrm{sc}}S_{\mathrm{wit}}}{L}X_{\mathrm{GND(IX)}} + \frac{G}{1+G}\frac{C_{\mathrm{sc}}S_{\mathrm{wit}}}{L}N_{\mathrm{wit}} \\ &+ \frac{1}{1+G}H_{\mathrm{s}}X_{\mathrm{GND(EX)}}, \end{aligned} \tag{4.19}$$

respectively, where $G = C_{\mathrm{fb}}P_{\mathrm{a}}$ is the loop gain and $L = B_{\mathrm{L}}S_{\mathrm{L}}$. Here, if $G \gg 1$ and we design the sensor correction filter C_{sc} so that

$$\frac{C_{\mathrm{sc}}S_{\mathrm{wit}}}{B_{\mathrm{L}}S_{\mathrm{L}}} = 1, \tag{4.20}$$

the displacement of each stage are given as

$$X_{\mathrm{STG(IX)}} = X_{\mathrm{GND(IX)}} + N_{\mathrm{L}}, \tag{4.21}$$

$$X_{\mathrm{STG(EX)}} = X_{\mathrm{GND(IX)}} + N_{\mathrm{L}} + N_{\mathrm{wit}}. \tag{4.22}$$

If the noise of the GIF as a wittness sensor is smaller than that of the relative position sensor, both stage motions are the same each other; $X_{\mathrm{STG(EX)}} = X_{\mathrm{STG(IX)}}$. This same motion means the reduction of the differential stage motion. Thus, the cavity length is isolated from the differential ground motion, which is the baseline length fluctuation.

Chapter 5

Demonstration of Baseline Compensation System

5.1 Experimental Arrangement

Because the purpose of the baseline compensation system is to reduce the arm cavity length fluctuation, we prepared the experimental arrangement to measure the length.

The length fluctuation of the X-arm cavity is measured by the PDH method [81]. This method obtains the error signal, which is proportional to the displacement from the nominal length where the cavity is on resonance. In order to keep the resonance, the error signal is fed back to the acousto-optics modulator (AOM), which changes the input laser frequency.

The brief measurement procedure is shown in Figure 5.1. (1) The deformation of the baseline causes the length change of the arm cavity length through the suspensions. Suppose that the baseline length is displaced by ΔL from the nominal length of L. Utilizing the PDH method, we can obtain the error signal proportional to this displacement. (2) This signal is also interpreted as the frequency changes of the input laser because the frequency change Δf has a relation with the baseline length change ΔL [39];

$$-\frac{\Delta f}{f} = \frac{\Delta L}{L}. \tag{5.1}$$

(3) To keep the optical cavity on resonance, the signal is fed back to the AOM, which is the frequency actuator. In this procedure, the length fluctuation is obtained from the feedback signal to the AOM.

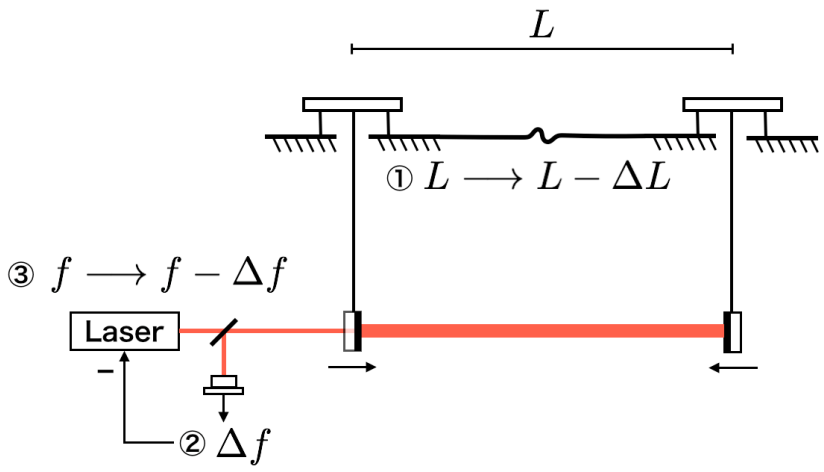

Figure 5.1: Experimental arrangement for X-arm length measurement. X-arm cavity controled by feeding the PDH signal back to the AOM of the input laser to keep on resonance. The length change of the cavity is obtained from the feedback signal.

5.2 Results

The performance of the baseline compensation system is evaluated when the system is engaged. Figure 5.2 shows the length fluctuation of the arm cavity and of the baseline as a reference. At 12 minutes, the baseline compensation system was turned on. Whereas the X-arm cavity length is drifted during the compensation system was off, the drift is removed during the system was on. As a result, this system compensated for the deformation of the baseline.

This result also indicates that the RMS amplitude of the X-arm cavity length is reduced. The amplitude spectrum density of the length when both the compensation system was on and off is shown in Figure 5.3. Accumulated RMS amplitude is reduced by -6 dB.

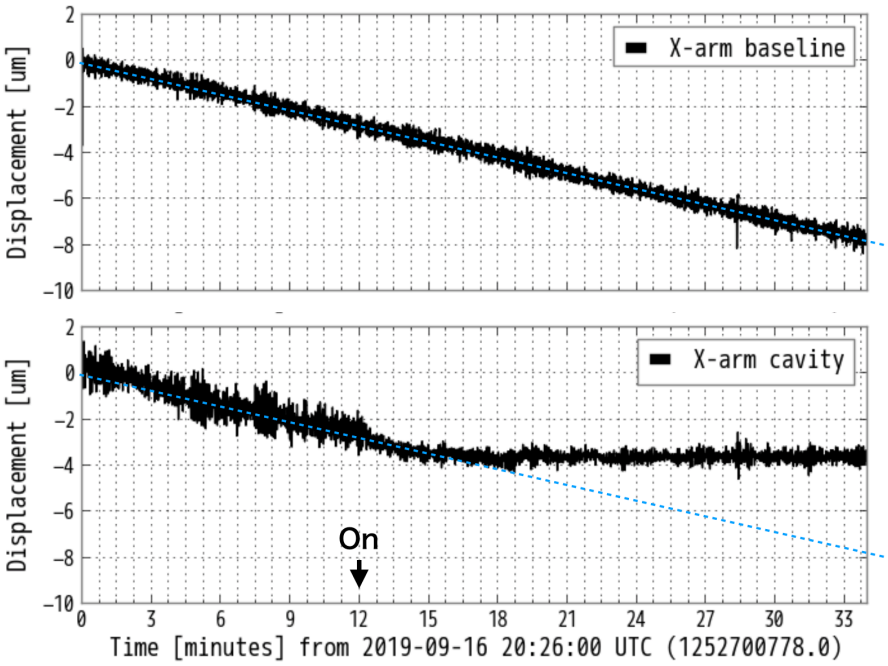

Figure 5.2: Length change of both X-arm baseline and X-arm cavity when baseline compensation system is turned on or off. At 12 minutes, the control is on.

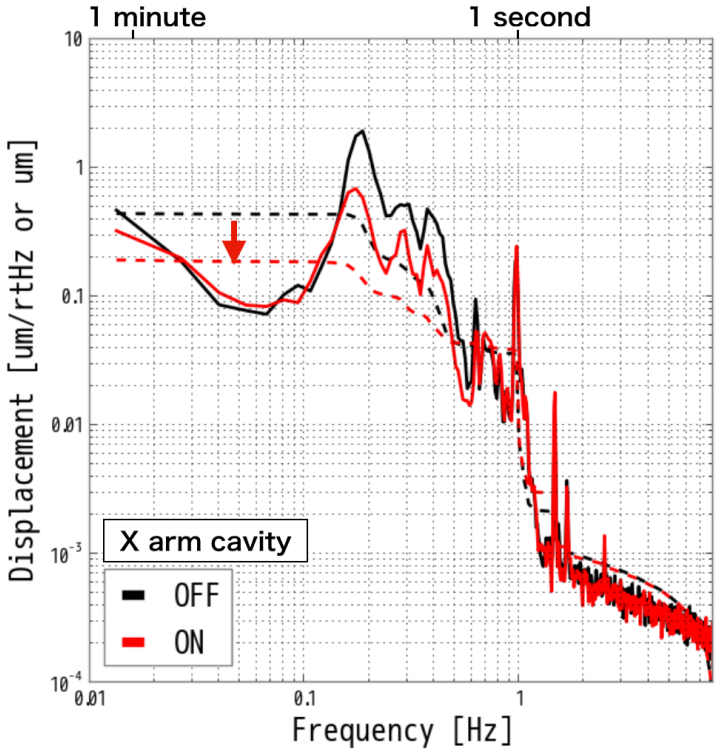

Figure 5.3: ASDs of X-arm caivty length when baseline compensation system is turned on and off.

5.3 Discussion

5.3.1 Earth Tides Band

While earth tides typically have RMS amplitudes of several 100 um, the RMS amplitude of the compensated arm cavity length shown in Figure 5.2 is less than 1 um. The demonstration this time was about 30 minutes, but if we tentatively determine that the arm cavity length fluctuated at this level during the period of the earth tide, we can say that the reduction rate was at least -40 dB.

5.3.2 Earthquake Band

No reduction was observed in the frequency band of 10 - 100 Hz where long-period earthquakes are a problem, as shown in Figure 5.3. The reason for the lack of reduction is that the GIF was covered by its own noise. Figure 5.5 shows the amplitude spectrum densities and coherence of the X-arm cavity length change and GIF signal before baseline length compensation. Below 0.1 Hz, there is no coherence between the X-arm cavity length and the GIF signal. GIF signal is bigger at 0.1 Hz than the seismometers signal as a reference. This noise excess suggests that the GIF is covered by its noise.

5.3.3 Microseismic Band

RMS amplitude above 0.1 Hz was reduced by -6 dB. This reduction is small compared with the apparent reduction rate for earth tides mentioned above.

We compared the rigid body model of the KAGRA seismic isolation system with the measured cavity length change before compensation. As a result, the model calculation agreed with the measurement. However, when we compare the measurement after compensation with the model calculation assuming a 5% calibration error, the measurement is larger than the calculation. This excess suggests that coupling from other degrees of freedom not included in the model calculations limits the reduction. In fact, in order to keep the X-arm cavity on resonance, the alignment was controlled using a sensor that measured the relative angle to the local ground. When the coherence between these control signals and the baseline length expansion and contraction of the X-arm was examined, coherence was observed in the frequency range of 0.1 Hz. For this reason, it is suggested that the coupling from the control signals to other degrees of freedoms limits the reduction rate in the band of microseismic noise.

Comparison with the model

Compare with the measured data and rigid body model of the KAGRA suspensions [80]. Because this model outputs the state-space model, we can calculate the transfer function. For example, the transfer function from the ground motion to each stage; the platform stage, test mass, and so on.

To simplify the discussion, suppose the CMRR is large enough to ignore the coupling from the common motion to the differential motion, as described in 4.2.2. It is a valid assumption below the eigenfrequency of the suspensions. According to Eq.(4.17), the transfer function from the differential input to differential output is given by a single transfer function. Therefore, the differential transfer functions from the differential ground motion to the differential output of the stage and the test mass motion are given by the single transfer function of that, respectively.

Figure 5.4a shows the amplitude spectrum densities (ASDs) of the X-arm cavity length when the compensation system is OFF. The black line is the ASD calculated by the feedback signal of the X-arm cavity. The red line is the ASD, which is the summation of the noise contributions, the noise of the relative position sensor, named LVDT (blue line), and the noise of the differential baseline length change measured by the GIF strainmeter (orange line). Above 1 Hz, the X-arm cavity length and the seismic noise contribution are not the signals due to the noises of the instruments. Below 1 Hz, the measurement is consistent with the estimation.

Figure 5.4b shows the ASDs of the X-arm cavity length when the compensation system is ON. The red line, which indicates the summation of the noise contribution estimated by the rigid body model, is calculated assuming the reduction factor of the sensor correction of 1/20, as mentioned in 4.1.2. This reduction factor is calculated from the relative calibration error of 5 % between the LVDT and GIF. Although this reduction rate should be realized, the measurement is not consistent with the estimation assumed the reduction rate. The RMS of the cavity length fluctuation is limited by peaks around 200 mHz.

Signal coupling

The peaks around 200 mHz, which are the main contributions to the RMS, are correlated with the other degrees of freedoms (DOFs).

Figure 5.5 shows the ASDs in the top figure and the coherence in the bottom figure when the compensation system was off. In the top figure, the ASDs of the X-arm cavity

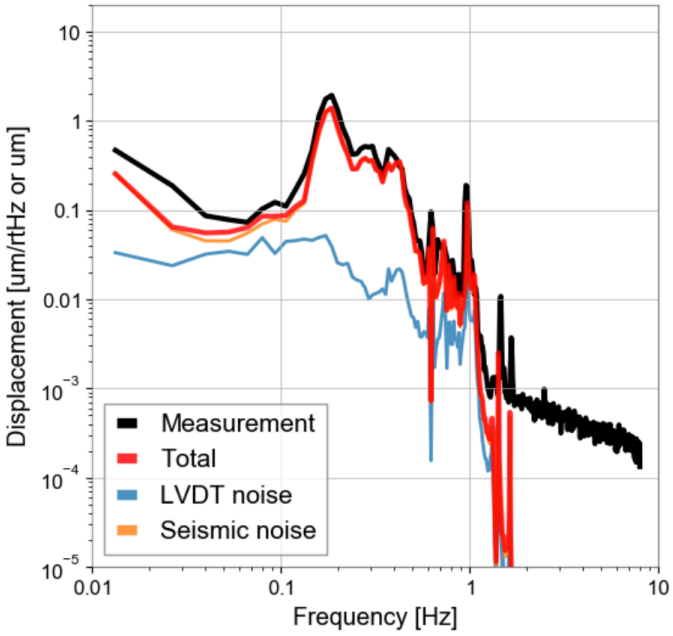

(a) Noise budget when the compensation system is OFF. Measurement is same as the black line in Fig.5.3. Total is the summation of all the noise contributions.

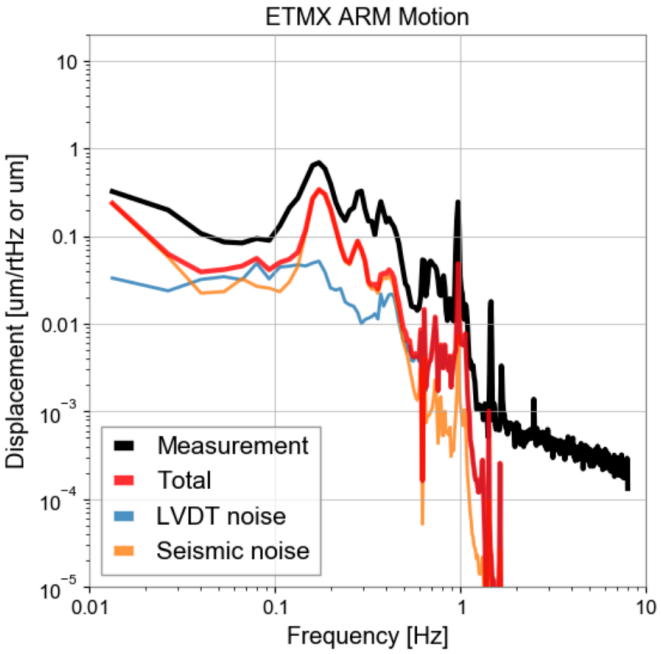

(b) Noise budget when the compensation system is ON. Measurement is the same as the red line in Fig.5.3. Total is the summation of all noise contributions assuming the reduction factor of sensor correction of 1/20.

Figure 5.4: Comparison between the measurement of X-arm and the expected value of that. The expected total value is the summation of some noise contribution, which is named the noise budget.

length and the baseline length changes are displayed. The baseline length changes are shown by two ASDs; the length change measured by the GIF strainmeter and that given by the differential signal of two seismometers, which is installed near the IX and EX stages. While, above 1 Hz, the baseline length change should be referred by the seismometer differential signal, below 50 mHz, the length change should be referred by the GIF strainmeter signal because of this self-noise. One can find that the X-arm cavity length is enhanced by some mechanical peaks compared with the baseline length change. On the other hand, the bottom figure shows some coherence between the X-arm cavity length and the GIF, and between the cavity length and the other DOFs' signals; the feedback signals of the yaw and transverse directions on the each IX and EX platform stages, which controls are needed to keep the X-arm cavity on resonance. Whereas the cavity length has a coherence with the deformation of the baseline measured by GIF strainmeter (blue) around 0.2 - 0.7 Hz broadly, coherence with the other DOFs does not exist clearly in this frequency region. This coherence implies that the cavity length is mainly disturbed by the deformation of the baseline.

Figure 5.6 show the ASDs and coherence when the compensation system was on. Around 0.2 Hz, the coherence between the cavity length and the many other DOFs appear, although these coherences did not when no length compensation. These coherences imply the cavity length is disturbed by the internal DOFs coupling.

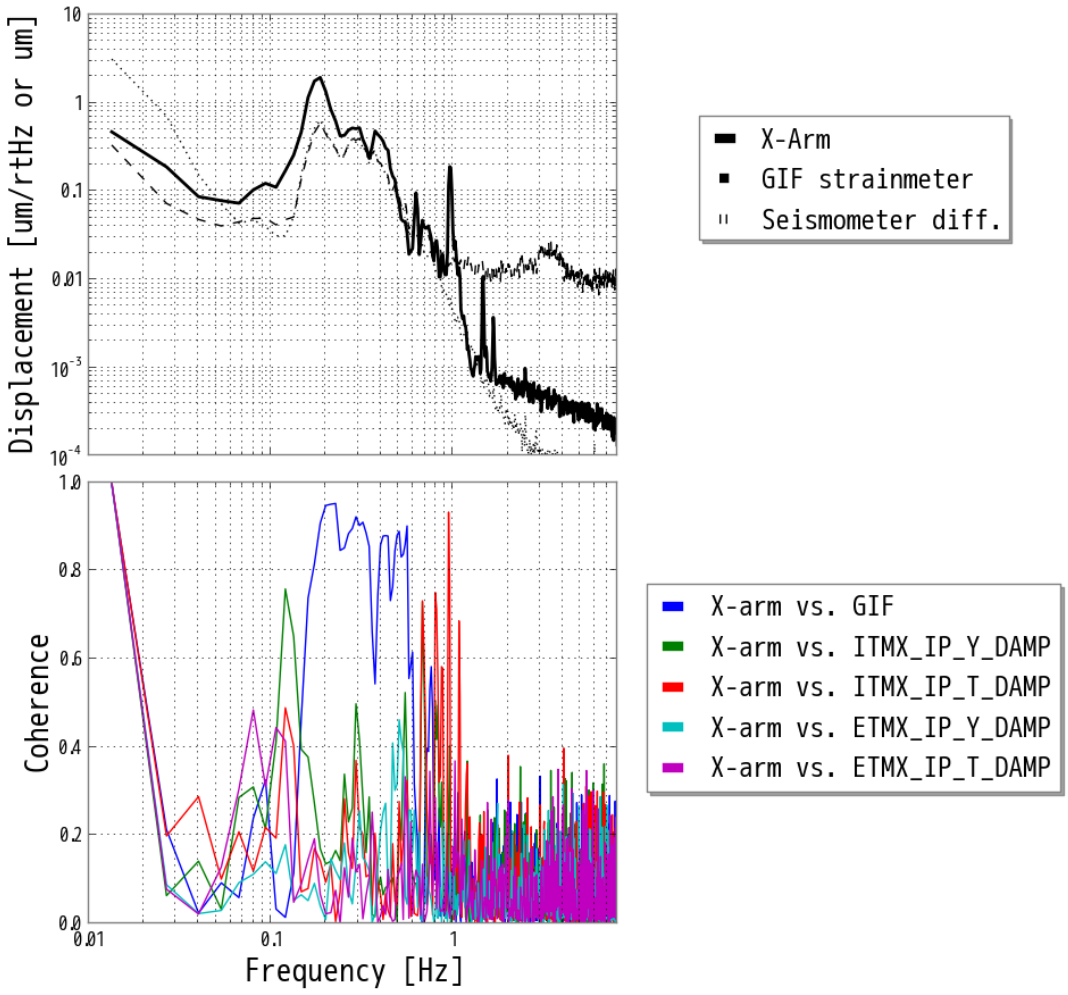

Figure 5.5: Coherence between the cavity length and GIF strainmeter, other degrees of freedoms on the stage control when the compensation system is on. (Top) ASD of the cavity length and baseline length. (Bottom) The coherence between the cavity's length and some signals.

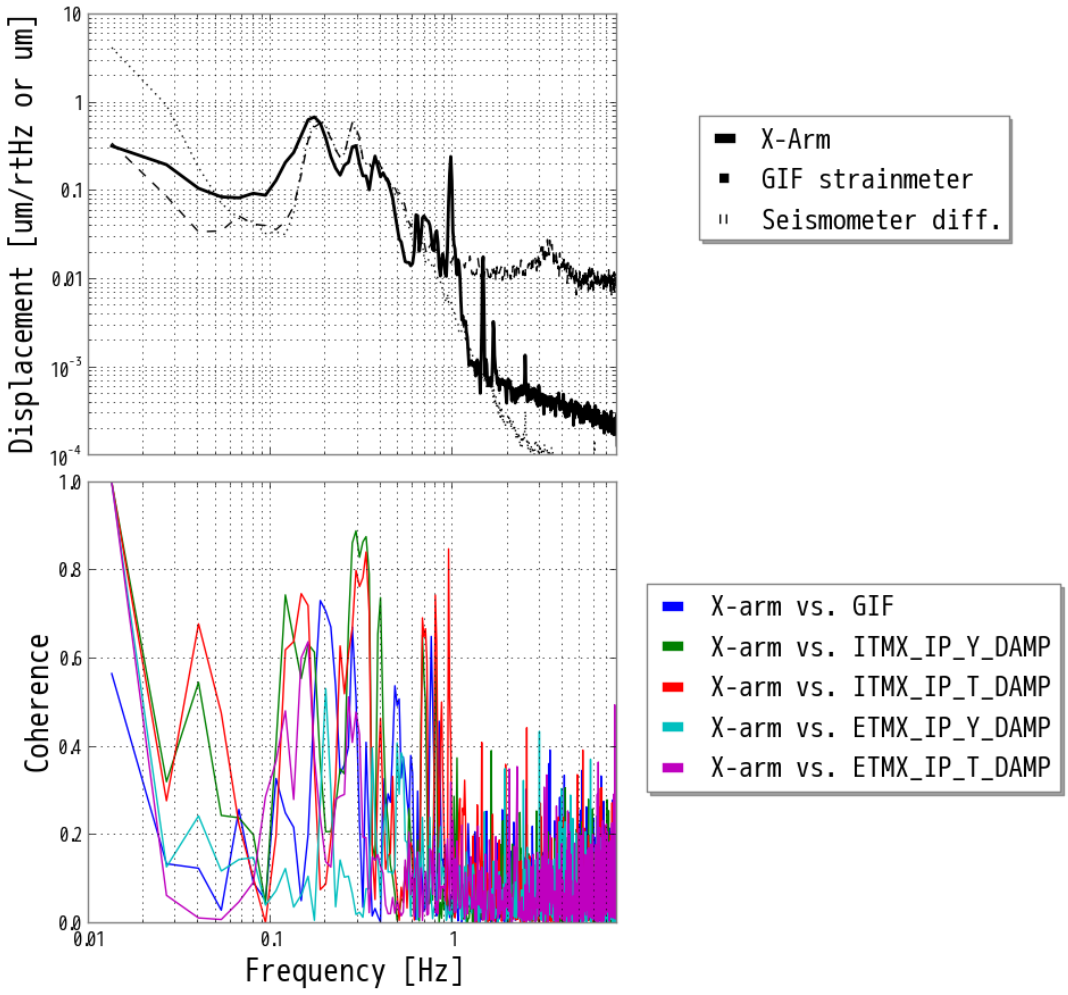

Figure 5.6: Coherence between the cavity length and GIF strainmeter, other degrees of freedom on the stage control when the compensation system is off. (Top) ASD of the cavity length and baseline length. (Bottom) The coherence between the cavity's length and some signals.

Chapter 6

Conculusion and Future Prospects

In this chapter, we conclude the thesis and describe future prospects.

6.1 Conclusion

In this study, we developed the baseline compensation system for reducing the influence of the low-frequency seismic noise. The baseline compensation system is the active baseline seismic isolation system for the optical arm cavities. This system only uses the GIF which can measure the baseline length changes directly. The conventional system uses a seismometer to measure the length change, which means that the insufficient isolation performance below 0.1 Hz due to the sensitivity of the seismometer.

We evaluated the performance of the new system by using the X-arm cavity. As a result, we have shown the reduction of the length at least by -6 dB below 1 Hz. The reduction was also in the earth tides band at least by -40 dB. This reduction is the first result of the kilo-meter scale active baseline seismic isolation in the world.

6.2 Future Prospects

In order to obtain higher seismic isolation performance, a seismic isolation system that combines the conventional seismic isolation system and the baseline length compensation system developed in this study is useful.

In this section, we describe the improvement of the baseline compensation system in the future and the prospection of improvement of the duty cycle.

6.2.1 Control Design

The demonstration in this study was for 30 minutes, during which the microseismic noise was quiet. In order to improve the duty cycle, it is necessary to isolate the seismic noises even in bad weather. Although we did not implement in this study, it is useful to incorporate a conventional active inertial seismic isolation system so that seismic isolation can isolate the microseismic. In other words, passive seismic isolation using a pendulum is used for frequencies above approximately 1 Hz, a baseline length compensation system is used for frequencies below 1 Hz, and an active inertial vibration isolation system is used for frequencies between 0.1 Hz and 10 Hz. Inertial sensors have higher noise levels than GIFs below 0.1 Hz, but lower levels above that. Therefore, in the microseismic band (0.1 Hz to 1 Hz), the vibration isolation performance of the conventional active inertial vibration isolation system is higher. This conventional system has a narrow frequency band for vibration isolation, but unlike the baseline length compensation system, the common component of the mirrors of the arm cavity can also be isolated. Moreover, in the microseismic band, the resonance frequency of inverted pendulum exists in the case of KAGRA. Thus the active inertial vibration isolation system using the feedback control is also useful in the point of appropriate damping control of these.

In order to improve the performance of the baseline compensation system, especially the microseismic noise band, we should use the active inertial seismic isolation system to enhance the performance in this band.

To simplify the discussion, we supposed the CMRR is large enough to ignore the common motion coupling. Thus, we can just consider the only differential component of the motion in this system.

The control diagram of the future baseline compensation system can be represented as shown in Figure 6.1. Essentially, all the terms in this figure are the same as the active inertial isolation system shown in Figure 4.1 except the input and output signals. These signals are replaced as X_{d} and Y_{d}, which are the differential displacement of the ground and platform stage motions, respectively. In this figure, S_{wit} and N_{ff} are the frequency response and the self-noise of the GIF, respectively. Furthermore, the noises N_{H} and N_{L} are multiplied by $\sqrt{2}$ in the case of the amplitude unit.

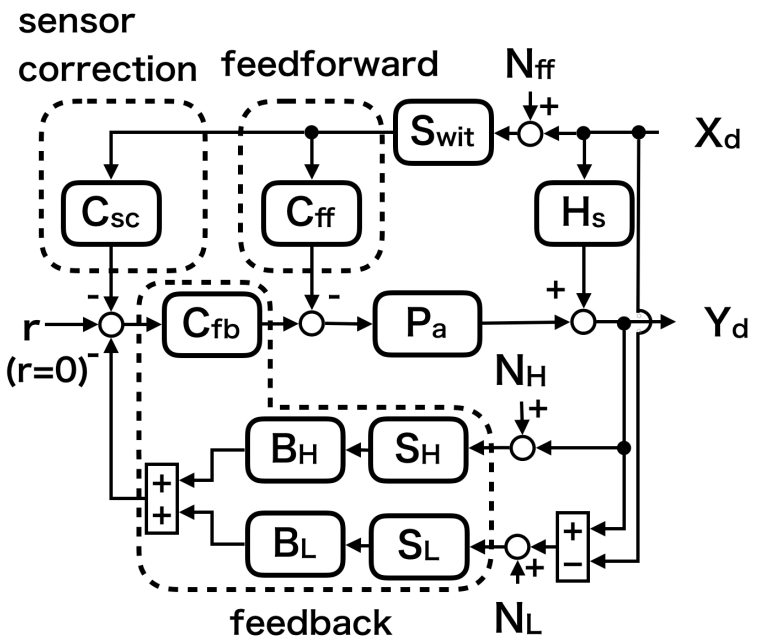

Figure 6.1: The block diagram of the future baseline compensation system.

The displacement of the differential motion of the stages is given by

$$\begin{aligned} Y_{\rm d} &= \frac{G}{1+G} L \Delta_{\rm sc} X_{\rm d} + \frac{1}{1+G} \Delta_{\rm ff} X_{\rm d} \\ &+ \frac{G}{1+G} \left(H N_H + L N_L \right) + \frac{G}{1+G} C_{\rm sc} S_{\rm wit} N_{\rm ff} \\ &+ \frac{1}{1+G} P_{\rm a} C_{\rm ff} S_{\rm wit} N_{\rm ff}. \end{aligned} \tag{6.1}$$

According to the first and second terms in the equation, the contribution of the ground motion $X_{\rm d}$ can be independently isolated by three factors: $\Delta_{\rm sc}$, $\Delta_{\rm ff}$, and L. While the current design needed high loop gain G to reduce the second term, this design does not need due to the $\Delta_{\rm ff}$. Thus, the feedforward path can make flexible design. Furthermore, the low-pass filter L can isolate the lower frequency motions if the inertial sensor on the stage has enough sensitivity to measure the microseismic noise band.

6.2.2 Improvement of Duty Cycle

If the baseline length compensation system developed in this study is applied to the currently operating gravitational wave detector, it will be possible to improve the lock loss caused by low-frequency ground vibration.

As shown in Figure 1.8 in chapter 1.4.2, the low-frequency ground vibration caused by environmental changes causes an average of 10% lock loss. This method can improve this. Furthermore, because we also reduce the amount of lock loss, we would reduce the number of lock acquisitions. Thus, locking time, which takes up 20% of the unobserved state, can also be reduced. Therefore, our compensation system will improve the lock loss except the maintenance or commissioning. The gravitational-wave detectors whose duty cycle is improved will enhance the gravitational-wave astronomy.

Appendix A

KAGRA

A.1 Overview of KAGRA

A.1.1 Status of KAGRA

KAGRA is a 3km laser interferometer constructed in Kamioka, Gifu, Japan, and is now in its final commissioning phase. KAGRA is now commissioning to observe with LIGO and Virgo in the third observation (O3), through the two test operation phase. The phases of the KAGRA project are listed in Table **??**. The first test operation named initial KAGRA (iKAGRA), which is taken place from March to April 2016, was a demonstration of the 3-km Michelson interferometer. In this operation, While the test masses are not in cryogenic temperature but room temperature, KAGRA demonstrates the operation of the km-scale interferometer in the underground. Next, the second test operation named baseline KAGRA (bKAGRA) demonstrated the cryogenic Michelson interferometer from April to May 2018. Although this interferometer was not for sensitivity enhanced configuration, the cryogenic operation, which is the key feature of KAGRA, could be demonstrated. Now, in December 2019, KAGRA is faced with the O3 observation with the Michelson interferometer, whose each arm has Fabry-Perot optical cavities (FPMI). To join the O3, KAGRA is now tunning the interferometer operation and hunting the several technical noises.

A.1.2 Main Interferometer

The main interferometer of KAGRA is shown in Figure A.1a. The interferometer configuration of KAGRA is also the same as other GW detectors such as advanced LIGO

Table A.1: Summary of the phases of KAGRA. MI: Michelson Interferometer, FPMI: Fabry-Perot Michelson Interferometer, DRFPMI: Dual-Recycled Fabry-Perot Michelson Interferometer, RSE: resonant sideband extraction

	iKAGRA	bKAGRA Phase1	bKAGRA for O3	bKAGRA (final)
Year	2016 Mar - Apr	2018 Apr - May	2019 Dec -	2020 - (planned)
Configuration	MI	MI	FPMI	DRFPMI (RSE)
Test mass temperature	room temp.	18K room temp.	18K room temp.	22K

and advanced Virgo, the Michelson interferometer with Fabry-Perot optical cavity on each arm and two recycling optical cavities. The different feature of these detectors is the cryogenic test masses. To cool down to cryogenic, typically 22 K, the test mass mirror is made of sapphire because of the high thermal conductivity and mechanical Q value even in a cryogenic environment. These properties can reduce some problems of the interferometric GW detectors; thermal lens effect and thermal noise. The main interferometer is divided into four parts; (1) arm cavities, (2) input and output mode cleaners (IMC and OMC), (3) power recycling cavities (PRC), (4) and signal recycling cavities (SRC). The first, the arm cavities are composed of input test masses (ITMs) and end test masses (ETMs) with high reflectivity corresponding to a finesse of 1530 not to increase the internal cavity power. The second, while IMC is used for clean out the higher-order spatial mode and stabilizing the frequency of the main input laser, OMC is used for clean out the unwanted higher-order spatial modes and frequency sideband of the output beam. The IMC is the triangle optical cavity which is made to stabilize the input laser frequency above 1 Hz. The OMC is the bow-tie cavity composed of four mirrors. The third, PRC is used for increasing the input laser power by ten times. This cavity is composed of three mirrors named PRM, PR2, and PR3, respectively. The forth, SRC is used to expand the bandwidth of GW signals. This technique is more important than Advanced LIGO and Advanced Virgo because the bandwidth is narrower than other detectors due to a high finesse arm cavity of KAGRA.

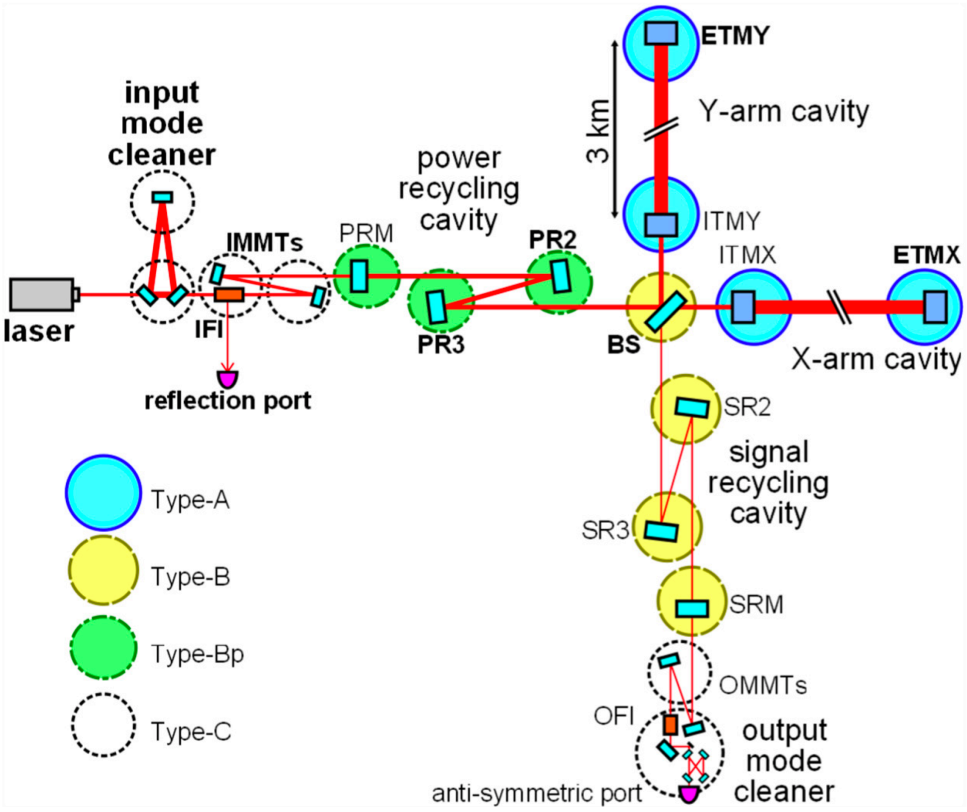

(a) Schematic interferometer configuration of KAGRA [36]

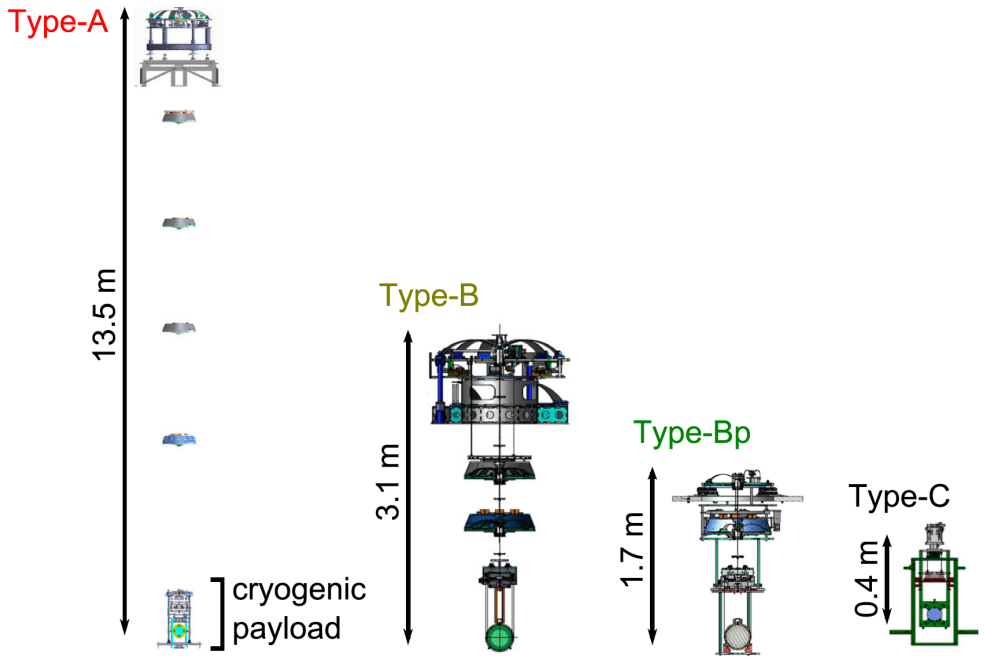

(b) KAGRA mirror suspension system [36]

Figure A.1: Interferometer configuration and mirror suspension system

A.1.3 Mirror Suspension System

All mirrors of the interferometer are suspended by four types of suspensions: Type-A, Type-B, Type-Bp, Type-C. These suspensions are shown in Figure A.1b. The Type-A is a 13.5 m scale 9-stage pendulum suspending the test mass mirror. The Type-B is a small size of Type-A suspension for suspending the signal recycling mirrors and beam splitter mirror. The Type-Bp is also a small size of Type-B but without the pre-isolator stage, which is for the power recycling mirrors. The type-C is the simple 2-stage suspension used in TAMA300 but with minor modification.

A.2 KAGRA Type-A Suspension

A.2.1 Overview

In order to suspend the cryogenic test mass, as shown in Fig.A.2, KAGRA Type-A suspension has two parts; cryogenic payload and 13.5 m room temperature tower pendulum [69]. The cryogenic payload consists of Platform, Marionette, Intermediate mass, Test mass. The tower consists of 5 mechanical filters; Top filter, F1, F2, F3, and Bottom filter. Moreover, the suspension point of the tower is suspended by the pre-isolator stage which has an inverted pendulum.

In terms of the low-frequency seismic attenuation, the pre-isolator is the important mechanical part.

A.2.2 Pre-Isolator stage (PI)

The pre-isolator (PI) is active seismic isolation for the suspension point of the long Type-A or Type-B suspensions. As shown in Figure A.3a, the suspension point is on the platform stage supported by the inverted pendulum (IP) which isolates the seismic noise in a horizontal direction. For vertical direction, geometric anti-spring (GAS) suspends this point. Especially, the horizontal motion of the platform stage is isolated by using the feedback control with the inertial sensor and the relative position sensor, which is described in section **??**.

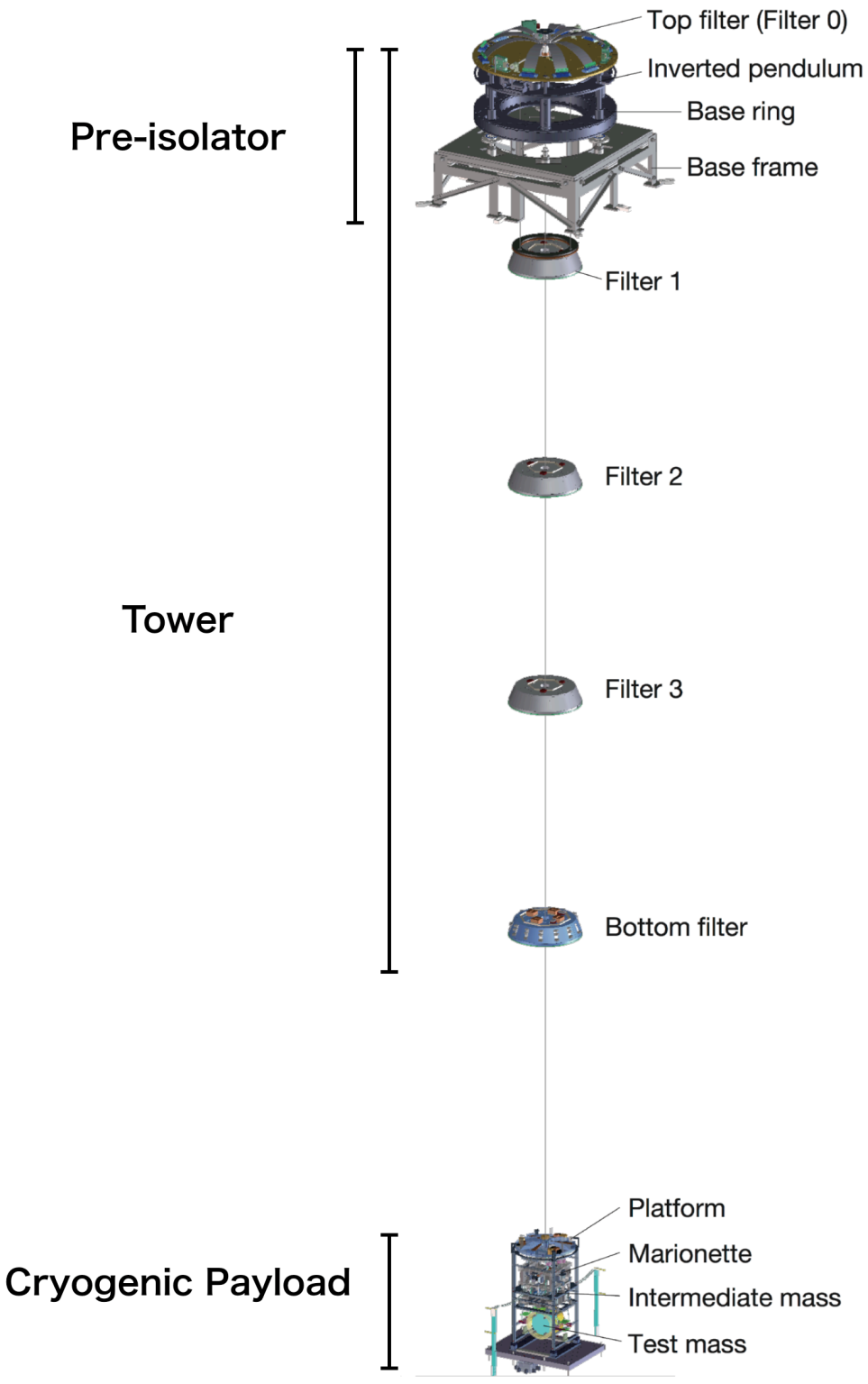

Figure A.2: An overview of the Type-A suspension [69]. Test mass is suspended by a 13.5 m pendulum consisted of several mechanical filters. The suspension point of the long pendulum is supported by the pre-isolator, which consists of an inverted pendulum, on the ground through the base frame and base ring.

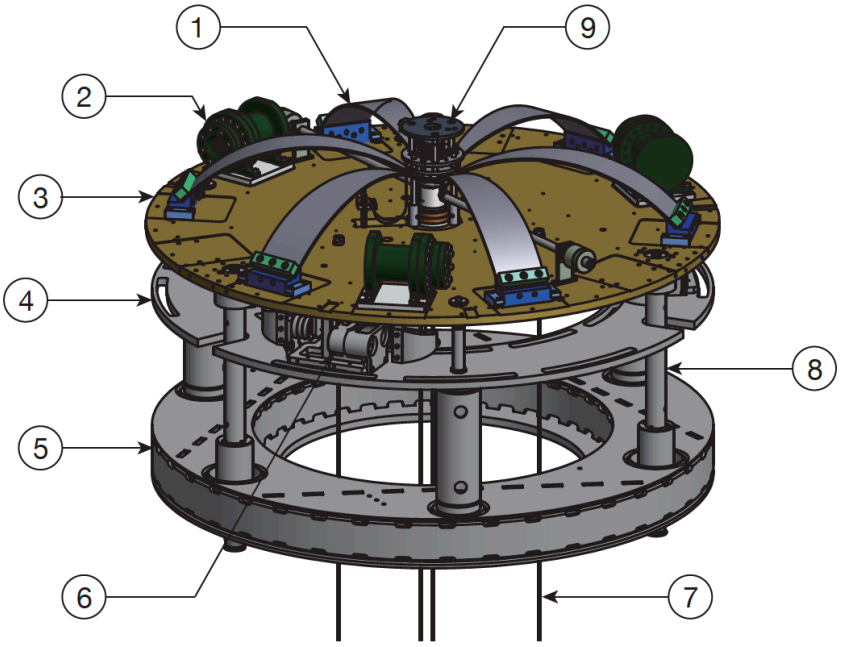

(a) Pre-isolator stage (PI). (1) Cantilever blade for GAS. (2) Geophone (3) Table of the top stage (4) Refernce frame rigidly connected to the base ring (5) The base ring mounted on the ground (6) LVDT and the coil magnet actuator (7) suspension wire to suspend the lower stages (8) leg of the inverted pendulum (IP). Figure is cited from figure 3.9 in [69]

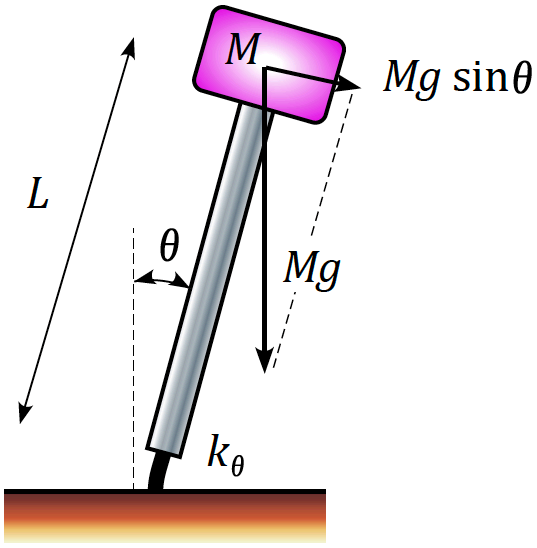

(b) Leg of the inverted pendulum (IP) [80].

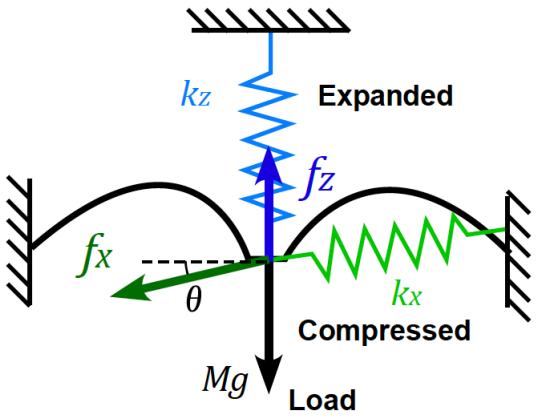

(c) Geometrical Anti-Spring [80].

Figure A.3: CAD drawing of the pre-isolator (top) and main mechanical components of PI; IP leg and GAS (bottom).

Inverted pendulum for horizontal vibration isolation

Inverted pendulum (IP) is the low eigenfrequency pendulum because this mechanical filter can adjust the effective spring constant to small value by tuning the load on the platform stage. The angular eigenfrequency of the single IP leg is given by [80]

$$\omega_{\mathrm{IP}} = \sqrt{\frac{g}{L}\left(\frac{k_\theta/gL - M}{M}\right)}, \tag{A.1}$$

$$\tag{A.2}$$

where k_θ is the bending spring constant of the flexure, M is the mass of the stage, and L is the length of the leg. Although the eigenfrequency can be adjusted to zero in principle, actual eigenfrequency is designed at least 100 mHz because it is unstable when the term in the square root is minus value.

Geometric Anti-Spring for vertical vibration isolation

Geometric anti-spring is also the low eigenfrequency pendulum in a vertical direction. The eigenfrequency is adjusted to small value by compressing the cantilever blades as shown in Figure A.3c. The angular eigenfrequency is given by

$$\omega_{\mathrm{GAS}} = \sqrt{\frac{1}{M}\left[k_z - \left(\frac{l_0}{x_0} - 1\right)k_x\right]}, \tag{A.3}$$

where M is the load mass, k_{x} and k_{z} are the elastic constant of the compressed catilevers, l_0 is a natural length of the blades, x_0 is the horizontal distance between the central keystone and the support poit of the blades. One can find that the angular eigenfrequency of the GAS is reduced when $x_0 < l_0$.

Liner Variable Differential Transducer (LVDT)

LVDT is a wide range relative position sensor composed of three coils [82]. shown in Fig.A.4. The emitter coil is mounted on the pre-isolator stage and driven with a sinusoidal signal to emit a modulated magnetic field. The two receiver coils are mounted on the reference structure, and these coils are counter-wound to each other. When the emitter coil is on the center of two receiver coils, the induced voltage is not emitted from the receiver coils. On the other hand, when the pre-isolator is moved, a sinusoidal signal appears on the receiver coils. Therefore, after demodulating this signal, the amplitude

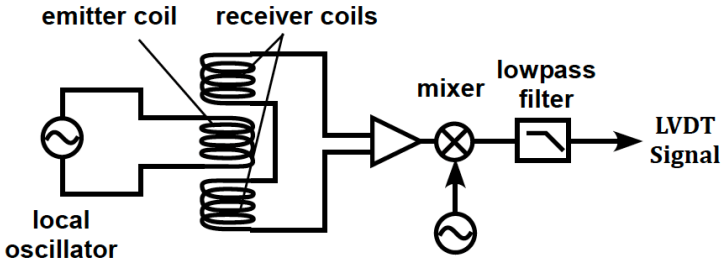

Figure A.4: [80]

of the output signal is proportional to the displacement from the LVDT geometrical center.

Coil-magnet actuator

We use a voice-coil type wide range actuator to move the pre-isolator stage [83].

Appendix B

Gaussian Beam

B.1 Gaussian beam

The ideal Gaussian beam has a fundamental spatial mode called TEM_{00}. The whose electric field of the beam propagating to z axis is given by [84, 85]

$$u(x,y,z) = \sqrt{\frac{2}{\pi w^2(z)}} \exp\left(i\zeta(z) - \mathrm{i}k\frac{x^2+y^2}{2R(z)} - i\frac{2\pi}{\lambda}z\right) \exp\left(-\frac{x^2+y^2}{w^2(z)}\right), \tag{B.1}$$

where λ, w_0 are the wavelength and the beam radius at $x = 0$ of the beam. In addition,

$$z_0 = \frac{\pi w_0^2}{\lambda} \tag{B.2}$$

$$w(z) = w_0\sqrt{1+\left(\frac{z}{z_0}\right)^2}, \tag{B.3}$$

$$R(z) = z\left[1+\left(\frac{z_0}{z}\right)^2\right], \tag{B.4}$$

$$\phi(z) = \arctan\left(\frac{z}{z_0}\right) \tag{B.5}$$

are Rayliegh range and radius, curvature, and Gouy phase of the beam as a function of z, respectively. One can find that power of the beam $|u^2|$ has a Gaussian distribution as shown in Figure B.1a according to Eq.(B.1).

As shown in Figure B.1b, the beam profiles given by Eq.(B.4,B.5,B.5) are plotted as a function of z. In near-field ($z = 0$), the beam can be regarded as the plane wave because the beam radius is smallest (beam waist), and the Gouy phase is 0. On the other hand, in far-field, the beam looks like a point source from far distant, and it is regarded as the spherical wave.

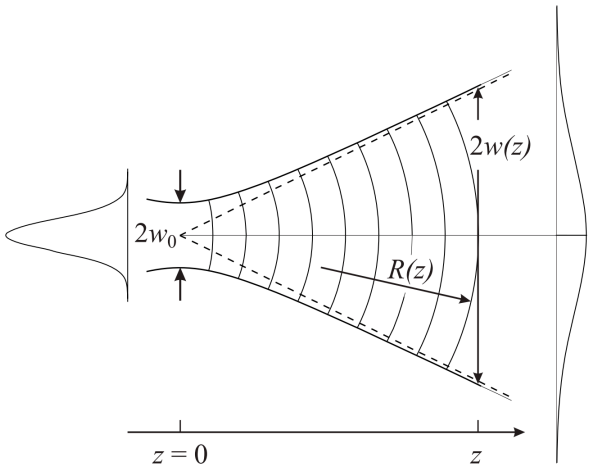

(a) Evolution of a Gaussian beam propagating along the z-axis[86]
w_0 denotes a beam radius at beam weist, where $z = 0$. $w(z)$ and $R(z)$ are the beam radius and curvature at z. Gouy phase is not shown in here.

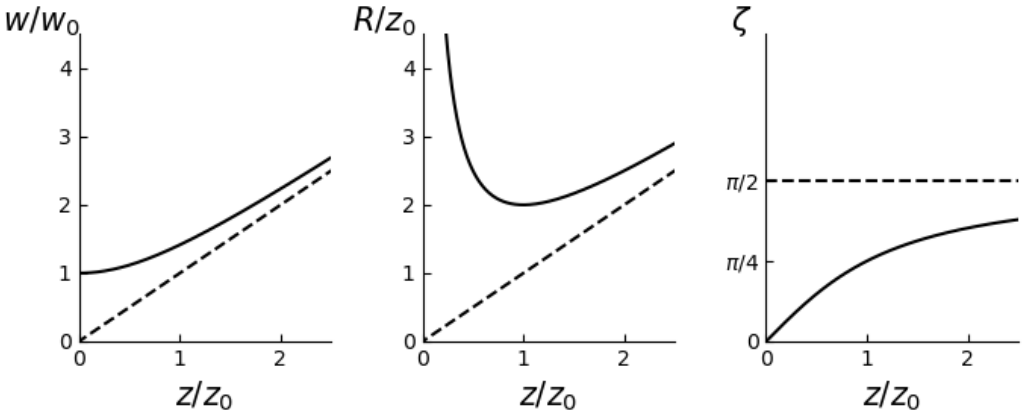

(b) Beam prifile
(left) Beam radius normalized by w_0 as a function of z/z_0, where z_0 is Rayleigh length. (Middle) Beam curvature normalized by z_0. (right) Gouy phase.

Figure B.1: Gaussian beam.

Bibliography

[1] Albert Einstein. The Foundation of the General Theory of Relativity. *Annalen Phys.*, 49(7):769–822, 1916. [Annalen Phys.354,no.7,769(1916)].

[2] Curt Cutler and Kip S Thorne. An overview of gravitational-wave sources. In *General Relativity and Gravitation*, pages 72–111. World Scientific, 2002.

[3] BP Abbott, R Abbott, TD Abbott, S Abraham, F Acernese, K Ackley, C Adams, RX Adhikari, VB Adya, C Affeldt, et al. Gwtc-1: a gravitational-wave transient catalog of compact binary mergers observed by ligo and virgo during the first and second observing runs. *Physical Review X*, 9(3):031040, 2019.

[4] Paola Leaci, LIGO Scientific Collaboration, Virgo Collaboration, et al. Searching for continuous gravitational wave signals using ligo and virgo detectors. In *Journal of Physics: Conference Series*, volume 354, page 012010. IOP Publishing, 2012.

[5] Mark Hereld. *A Search for Gravitational Radiation from PSR 1937+ 214*. PhD thesis, California Institute of Technology, 1984.

[6] Christian D Ott, Adam Burrows, Eli Livne, and Rolf Walder. Gravitational waves from axisymmetric, rotating stellar core collapse. *The Astrophysical Journal*, 600(2):834, 2004.

[7] AA Starobinskii. Spectrum of relict gravitational radiation and the early state of the universe. *JETP Letters*, 30:682–685, 1979.

[8] Nelson Christensen. Stochastic gravitational wave backgrounds. *Reports on Progress in Physics*, 82(1):016903, nov 2018.

[9] Alan H. Guth. Inflationary universe: A possible solution to the horizon and flatness problems. *Phys. Rev. D*, 23:347–356, Jan 1981.

[10] Rainer Weiss. Electronically coupled broadband gravitational antenna. 1972.

[11] Rana X. Adhikari. Gravitational radiation detection with laser interferometry. *Reviews of Modern Physics*, 86(1):121–151, feb 2014.

[12] Takaaki Yokozawa, Mitsuhiro Asano, Tsubasa Kayano, Yudai Suwa, Nobuyuki Kanda, Yusuke Koshio, and Mark R Vagins. Probing the rotation of core-collapse supernova with a concurrent analysis of gravitational waves and neutrinos. *The Astrophysical Journal*, 811(2):86, 2015.

[13] Hiroki Takeda, Atsushi Nishizawa, Yuta Michimura, Koji Nagano, Kentaro Komori, Masaki Ando, and Kazuhiro Hayama. Polarization test of gravitational waves from compact binary coalescences. *Physical Review D*, 98(2):022008, 2018.

[14] Masaki Ando. *Power recycling for an interferometric gravitational wave detector*. PhD thesis, University of Tokyo, 1998.

[15] Brian J Meers. Recycling in laser-interferometric gravitational-wave detectors. *Physical Review D*, 38(8):2317, 1988.

[16] Jan Harms. Terrestrial gravity fluctuations. *Living reviews in relativity*, 18(1):3, 2015.

[17] Jennifer Clair Driggers. *Noise Cancellation for Gravitational Wave Detectors*. PhD thesis, California Institute of Technology, 2015.

[18] Dan Chen. *Study of a cryogenic suspension system for the gravitational wave telescope KAGRA*. PhD thesis, University of Tokyo, 2016.

[19] Yu. Levin. Internal thermal noise in the ligo test masses: A direct approach. *Phys. Rev. D*, 57:659–663, Jan 1998.

[20] Kenji Numata, Masaki Ando, Kazuhiro Yamamoto, Shigemi Otsuka, and Kimio Tsubono. Wide-band direct measurement of thermal fluctuations in an interferometer. *Phys. Rev. Lett.*, 91:260602, Dec 2003.

[21] Gregory M Harry, Andri M Gretarsson, Peter R Saulson, Scott E Kittelberger, Steven D Penn, William J Startin, Sheila Rowan, Martin M Fejer, DRM Crooks,

Gianpietro Cagnoli, et al. Thermal noise in interferometric gravitational wave detectors due to dielectric optical coatings. *Classical and Quantum Gravity*, 19(5):897, 2002.

[22] Chiang-Mei Chen, James M Nester, and Wei-Tou Ni. A brief history of gravitational wave research. *Chinese Journal of Physics*, 55(1):142–169, 2017.

[23] Mark G. Beker. *Low-frequency sensitivity of next generation gravitational wave detectors*. PhD thesis, Vrije U., Amsterdam, 2013.

[24] 新藤 静夫. 武蔵野台地の地下地質. **地學雜誌**, 78(7):449–470, 1970.

[25] Shuichi Sato, Shinji Miyoki, Souichi Telada, Daisuke Tatsumi, Akito Araya, Masatake Ohashi, Yoji Totsuka, Mitsuhiro Fukushima, Masa-Katsu Fujimoto, LISM Collaboration, et al. Ultrastable performance of an underground-based laser interferometer observatory for gravitational waves. *Physical Review D*, 69(10):102005, 2004.

[26] M Ohashi, K Kuroda, S Miyoki, T Uchiyama, K Yamamoto, K Kasahara, T Shintomi, A Yamamoto, T Haruyama, Y Saito, et al. Design and construction status of clio. *Classical and Quantum Gravity*, 20(17):S599, 2003.

[27] Masaki Ando, Koji Arai, Ryutaro Takahashi, Gerhard Heinzel, Seiji Kawamura, Daisuke Tatsumi, Nobuyuki Kanda, Hideyuki Tagoshi, Akito Araya, Hideki Asada, et al. Stable operation of a 300-m laser interferometer with sufficient sensitivity to detect gravitational-wave events within our galaxy. *Physical Review Letters*, 86(18):3950, 2001.

[28] Hartmut Grote, LIGO Scientific Collaboration, et al. The geo 600 status. *Classical and Quantum Gravity*, 27(8):084003, 2010.

[29] Hirotaka Takahashi, Hideyuki Tagoshi, Masaki Ando, Koji Arai, Peter Beyersdorf, Nobuyuki Kanda, Seiji Kawamura, Norikatsu Mio, Shinji Miyoki, Shigenori Moriwaki, et al. Coincidence analysis to search for inspiraling compact binaries using tama300 and lism data. *Physical Review D*, 70(4):042003, 2004.

[30] Stephen Fairhurst, Gianluca M. Guidi, Patrice Hello, John T. Whelan, and Graham Woan. Current status of gravitational wave observations. *General Relativity and Gravitation*, 43(2):387–407, Feb 2011.

[31] T Akutsu and et. al. Construction of kagra: an underground gravitational-wave observatory. *Progress of Theoretical and Experimental Physics*, 2018(1), 01 2018. Link.

[32] F Acernese, M Agathos, K Agatsuma, D Aisa, N Allemandou, A Allocca, J Amarni, P Astone, G Balestri, G Ballardin, et al. Advanced virgo: a second-generation interferometric gravitational wave detector. *Classical and Quantum Gravity*, 32(2):024001, 2014.

[33] Junaid Aasi, BP Abbott, Richard Abbott, Thomas Abbott, MR Abernathy, Kendall Ackley, Carl Adams, Thomas Adams, Paolo Addesso, RX Adhikari, et al. Advanced ligo. *Classical and quantum gravity*, 32(7):074001, 2015.

[34] Benjamin P Abbott, R Abbott, TD Abbott, MR Abernathy, F Acernese, K Ackley, C Adams, T Adams, P Addesso, RX Adhikari, et al. Prospects for observing and localizing gravitational-wave transients with advanced ligo, advanced virgo and kagra. *Living Reviews in Relativity*, 21(1):3, 2018.

[35] B P Abbott, R Abbott, T D Abbott, M R Abernathy, K Ackley, C Adams, P Addesso, R X Adhikari, V B Adya, C Affeldt, et al. Exploring the sensitivity of next generation gravitational wave detectors. *Class. Quantum Grav*, 34(044001):044001, 2017.

[36] Takayuki Tomaru, Toshikazu Suzuki, Tomiyoshi Haruyama, Takakazu Shintomi, Nobuaki Sato, Akira Yamamoto, Yuki Ikushima, Tomohiro Koyama, and Rui Li. Development of a cryocooler vibration-reduction system for a cryogenic interferometric gravitational wave detector. *Classical and Quantum Gravity*, 21(5):S1005, 2004.

[37] Takashi Uchiyama, Shinji Miyoki, Souichi Telada, Kazuhiro Yamamoto, Masatake Ohashi, Kazuhiro Agatsuma, Koji Arai, Masa-Katsu Fujimoto, Tomiyoshi Haruyama, Seiji Kawamura, et al. Reduction of thermal fluctuations in a cryogenic laser interferometric gravitational wave detector. *Physical review letters*, 108(14):141101, 2012.

[38] T Akutsu, M Ando, K Arai, Y Arai, S Araki, A Araya, N Aritomi, H Asada, Y Aso, S Atsuta, et al. First cryogenic test operation of underground km-scale gravitational-wave observatory kagra. *arXiv preprint arXiv:1901.03569*, 2019.

[39] S Biscans, J Warner, R Mittleman, C Buchanan, M Coughlin, M Evans, H Gabbard, J Harms, B Lantz, N Mukund, A Pele, C Pezerat, P Picart, H Radkins, and T Shaffer. Control strategy to limit duty cycle impact of earthquakes on the LIGO gravitational-wave detectors. *Classical and Quantum Gravity*, 35(5):055004, jan 2018.

[40] Adam J Mullavey, Bram JJ Slagmolen, John Miller, Matthew Evans, Peter Fritschel, Daniel Sigg, Sam J Waldman, Daniel A Shaddock, and David E McClelland. Arm-length stabilisation for interferometric gravitational-wave detectors using frequency-doubled auxiliary lasers. *Optics express*, 20(1):81–89, 2012.

[41] Kiwamu Izumi. *Multi-Color Interferometry for Lock Acquisition of Laser Interferometric Gravitational-wave Detectors*. PhD thesis, University of Tokyo, 2012.

[42] M Punturo, M Abernathy, F Acernese, B Allen, Nils Andersson, K Arun, F Barone, B Barr, M Barsuglia, M Beker, et al. The einstein telescope: a third-generation gravitational wave observatory. *Classical and Quantum Gravity*, 27(19):194002, 2010.

[43] Peter M. Shearer. *Introduction to Seismology*. Cambridge University Press, 2 edition, 2009.

[44] 西村太志 長谷川昭, 佐藤春夫. *Seismology*, volume 6 of *Introduction to Modern Erath Science Series*. Kyoritsu, 2015.

[45] 竹本修三, 新谷昌人, 赤松純平, 森井亙, 東敏博, 福田洋一, 尾上謙介, 市川信夫, 川崎一朗, 大橋正健, et al. 神岡鉱山における 100 メートルレーザー伸縮計について. **京都大学防災研究所年報**, 2003.

[46] Sylvette Bonnefoy-Claudet, Fabrice Cotton, and Pierre-Yves Bard. The nature of noise wavefield and its applications for site effects studies: A literature review. *Earth-Science Reviews*, 79(3-4):205–227, 2006.

[47] E J Daw, J A Giaime, D Lormand, M Lubinski, and J Zweizig. Long-term study of the seismic environment at LIGO. *Classical and Quantum Gravity*, 21(9):2255–2273, apr 2004.

[48] M G Beker, J F J van den Brand, E Hennes, and D S Rabeling. Newtonian noise and ambient ground motion for gravitational wave detectors. *Journal of Physics: Conference Series*, 363:012004, jun 2012.

[49] R. Schofield et al. Source and propagation of the predominant 1-50 hz seismic signal from off-site at ligo-hanford. In LIGO Scientific Collaboration Meeting, Hanford, August 2000.

[50] Jon R Peterson. Observations and modeling of seismic background noise. Technical report, US Geological Survey, 1993.

[51] Kiwamu Nishida, Naoki Kobayashi, and Yoshio Fukao. Origin of earth's ground noise from 2 to 20 mhz. *Geophysical Research Letters*, 29(10):52–1, 2002.

[52] P Bormann. New manual of seismological observatory practice. *GFZ German Research Centre for Geosciences*, 2012. Link.

[53] RA Haubrich, WH Munk, and FE Snodgrass. Comparative spectra of microseisms and swell. *Bulletin of the Seismological Society of America*, 53(1):27–37, 1963. Link.

[54] Michael Selwyn Longuet-Higgins. A theory of the origin of microseisms. *Philosophical Transactions of the Royal Society of London. Series A, Mathematical and Physical Sciences*, 243(857):1–35, 1950. Link.

[55] GG Sorrells, John A McDonald, ZA Der, and Eugene Herrin. Earth motion caused by local atmospheric pressure changes. *Geophysical Journal International*, 26(1-4):83–98, 1971.

[56] W Zürn and R Widmer. On noise reduction in vertical seismic records below 2 mhz using local barometric pressure. *Geophysical Research Letters*, 22(24):3537–3540, 1995.

[57] Keiiti Aki and Paul G Richards. *Quantitative seismology*. 2002.

[58] Keiiti Aki. Scaling law of seismic spectrum. *Journal of geophysical research*, 72(4):1217–1231, 1967.

[59] Duncan Carr Agnew. Earth tides: an introduction. 2005.

[60] Nanometrics Inc., 250 Herzberg Road Kanata, Ontario, Canada K2K 2A1. *Trillium 120Q/QA User Guide*, 04 2017.

[61] Rolf Bork, R Abbott, D Barker, and J Heefner. An overview of the ligo control and data acquisition system. *arXiv preprint physics/0111077*, 2001.

[62] Akito Araya, Akiteru Takamori, Wataru Morii, Kouseki Miyo, Masatake Ohashi, Kazuhiro Hayama, Takashi Uchiyama, Shinji Miyoki, and Yoshio Saito. Design and operation of a 1500-m laser strainmeter installed at an underground site in kamioka, japan. *Earth, Planets and Space (Online)*, 69(1):1, 2017.

[63] Philip E Ciddor. Refractive index of air: new equations for the visible and near infrared. *Applied optics*, 35(9):1566–1573, 1996.

[64] Kouseki Miyo. 重力波望遠鏡 kagra のための地殻変動モニターの開発. Master's thesis, University of Tokyo, 2017.

[65] Akito Araya, Takashi Kunugi, Yoshio Fukao, Isao Yamada, Naoki Suda, Sumitaka Maruyama, Norikatsu Mio, and Shigenori Moriwaki. Iodine-stabilized nd: Yag laser applied to a long-baseline interferometer for wideband earth strain observations. *Review of scientific instruments*, 73(6):2434–2439, 2002.

[66] James J Snyder, Rama K Raj, Daniel Bloch, and Martial Ducloy. High-sensitivity nonlinear spectroscopy using a frequency-offset pump. *Optics letters*, 5(4):163–165, 1980.

[67] Norman Bobroff. Recent advances in displacement measuring interferometry. *Measurement Science and Technology*, 4(9):907, 1993.

[68] Mark A Zumberge, Jonathan Berger, Matthew A Dzieciuch, and Robert L Parker. Resolving quadrature fringes in real time. *Applied optics*, 43(4):771–775, 2004.

[69] S Wen, R Mittleman, K Mason, J Giaime, R Abbott, J Kern, B OReilly, R Bork, M Hammond, C Hardham, et al. Hydraulic external pre-isolator system for ligo. *Classical and Quantum Gravity*, 31(23):235001, 2014.

[70] S. Braccini. The VIRGO suspensions. In *Classical and Quantum Gravity*, volume 19, pages 1623–1629, apr 2002.

[71] Okutomi Koki. *Development of 13.5-meter-tall Vibration Isolation System for the Main Mirrors in KAGRA*. PhD thesis, SOKENDAI, The Graduate University for Advanced Studies, 2019. Link.

[72] F Matichard, B Lantz, R Mittleman, K Mason, J Kissel, B Abbott, S Biscans, J McIver, R Abbott, S Abbott, et al. Seismic isolation of advanced ligo: Review

of strategy, instrumentation and performance. *Classical and Quantum Gravity*, 32(18):185003, 2015.

[73] Wensheng Hua. *LOW FREQUENCY VIBRATION ISOLATION AND ALIGNMENT SYSTEM FOR ADVANCED LIGO*. PhD thesis, stanford university, 2005.

[74] Christophe Collette, Stefan Janssens, Pablo Fernandez-Carmona, Kurt Artoos, Michael Guinchard, Claude Hauviller, and André Preumont. Inertial sensors for low-frequency seismic vibration measurement. *Bulletin of the seismological society of America*, 102(4):1289–1300, 2012.

[75] Sebastein Biscans. *Optimization of the Advanced LIGO gravitational-wave detectors duty cycle by reduction of parametric instabilities and environmental impacts*. PhD thesis, University of Maine, 2018.

[76] R. W. P . Drever. Outline of a proposed design for a first receiver for installation in the long-baseline facilities, of fabry-perot type. Technical Report T870001-00-R, LIGO Document, 9 1987.

[77] Ronald WP Drever and Steven J Augst. Extension of gravity-wave interferometer operation to low frequencies. *Classical and Quantum Gravity*, 19(7):2005, 2002.

[78] Y Aso, M Ando, K Kawabe, S Otsuka, and K Tsubono. Stabilization of a fabry–perot interferometer using a suspension-point interferometer. *Physics Letters A*, 327(1):1–8, 2004.

[79] Kenji Numata and Jordan Camp. Interferometric testbed for nanometer level stabilization of environmental motion over long time scales. *Appl. Opt.*, 47(36):6832–6841, Dec 2008.

[80] Yuta Michimura, Tomofumi Shimoda, Takahiro Miyamoto, Ayaka Shoda, Koki Okutomi, Yoshinori Fujii, Hiroki Tanaka, Mark A Barton, Ryutaro Takahashi, Yoichi Aso, et al. Mirror actuation design for the interferometer control of the kagra gravitational wave telescope. *Classical and Quantum Gravity*, 34(22):225001, 2017.

[81] J Aasi, J Abadie, BP Abbott, Robert Abbott, T Abbott, MR Abernathy, T Accadia, F Acernese, C Adams, T Adams, et al. Characterization of the ligo detectors during their sixth science run. *Classical and Quantum Gravity*, 32(11):115012, 2015.

[82] Takanori Sekiguchi. *A Study of Low Frequency Vibration Isolation System for Large Scale Gravitational Wave Detectors*. PhD thesis, Department of Physics School of Science, University of Tokyo, 2016.

[83] RWP Drever, John L Hall, FV Kowalski, J_ Hough, GM Ford, AJ Munley, and H Ward. Laser phase and frequency stabilization using an optical resonator. *Applied Physics B*, 31(2):97–105, 1983.

[84] Hareem Tariq et al. The linear variable differential transformer (LVDT) position sensor for gravitational wave interferometer low-frequency controls. *Nucl. Instrum. Meth.*, A489:570–576, 2002.

[85] Chenyang Wang, Hareem Tariq, Riccardo DeSalvo, Yukiyoshi Iida, Szabolcs Marka, Yuhiko Nishi, Virginio Sannibale, and Akiteru Takamori. Constant force actuator for gravitational wave detector's seismic attenuation systems (sas). *Nuclear Instruments and Methods in Physics Research Section A: Accelerators, Spectrometers, Detectors and Associated Equipment*, 489(1-3):563–569, 2002.

[86] Charlotte Bond, Daniel Brown, Andreas Freise, and Kenneth A Strain. Interferometer techniques for gravitational-wave detection. *Living reviews in relativity*, 19(1):3, 2016.

[87] Orazio Svelto. *Principles of lasers*, volume 4. Springer.

[88] Fritz Riehle. *Frequency standards: basics and applications*. John Wiley & Sons, 2006.